Department of Precision and Microsystems Engineering

Towards a neutrino trap

Design, optimization, realization and characterization of a fiber laser hydrophone

Laura Peeperkorn

Report no : 2018.040
Coach : Ernst-Jan Buis, Jan de Vreugd
Professor : M. Langelaar
Specialisation : SOM
Type of report : Thesis
Date : 13 November 2018

Towards a neutrino trap

Design, optimization, realization and characterization of a fiber laser hydrophone

L.M. Peeperkorn

Master of Science Thesis

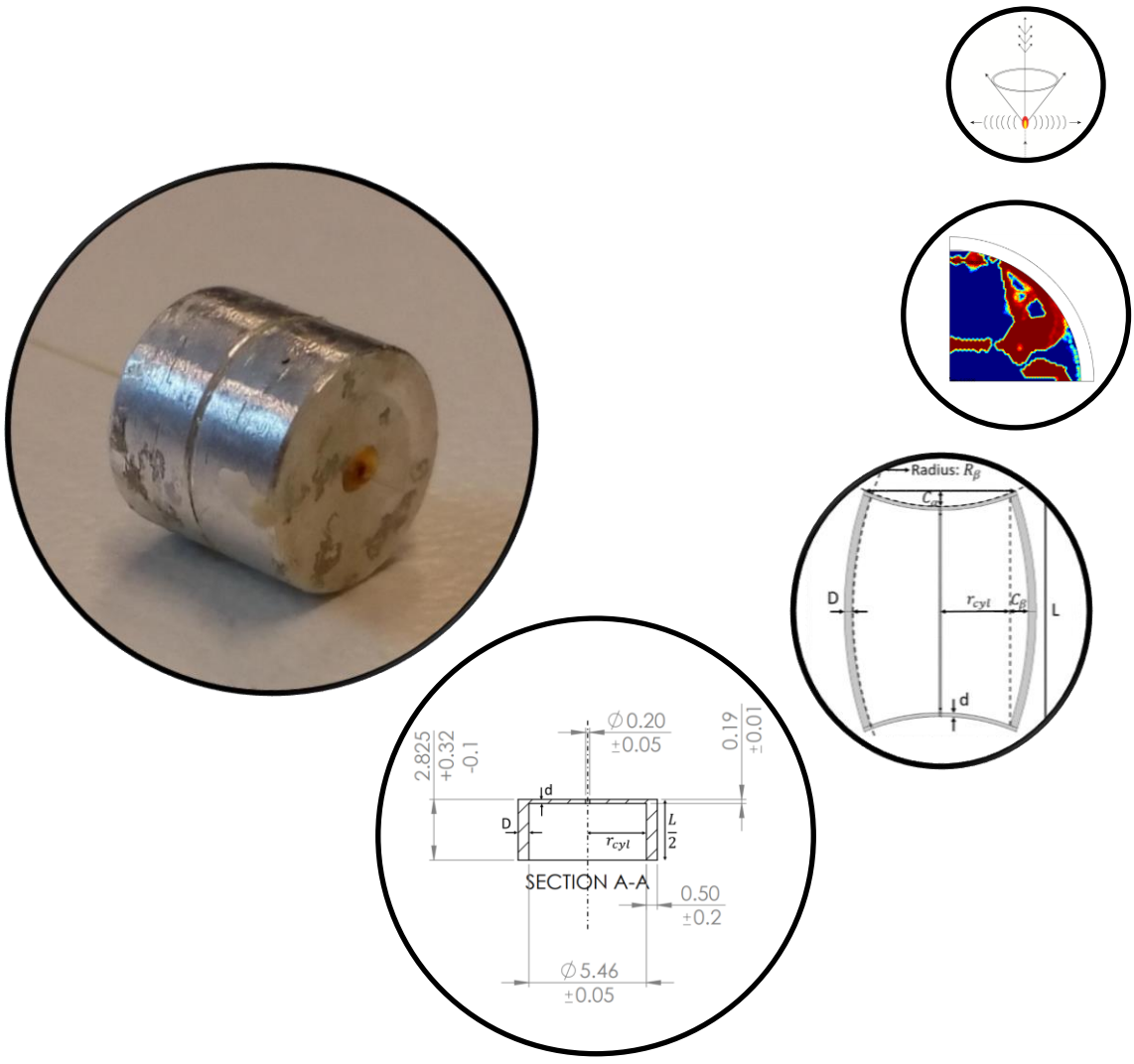

TU Delft Delft University of Technology

Precision and Microsystems Engineering

Towards a neutrino trap

Design, optimization, realization and characterization of a fiber laser hydrophone

Master of Science Thesis

For the degree of Master of Science in Precision and Microsystems Engineering at Delft University of Technology

L.M. Peeperkorn

November 13, 2018

Faculty of Mechanical, Maritime and Materials Engineering (3mE) · Delft University of Technology

The work in this thesis was supported by TNO.

Delft University of Technology
Department of
Precision and Microsystems Engineering

The undersigned hereby certify that they have read and recommend to the Faculty of Mechanical, Maritime and Materials Engineering (3mE) for acceptance a thesis entitled

Towards a neutrino trap

Design, optimization, realization and characterization of a fiber laser hydrophone

by

L.M. Peeperkorn

in partial fulfillment of the requirements for the degree of

Master of Science Precision and Microsystems Engineering

Dated: November 27, 2018

Supervisor(s):

Dr. ir. M. Langelaar. Supervisor

Dr. ir. E.J. Buis. Second Supervisor

Dr. ir. J. de Vreugd. Third Supervisor

Reader(s):

Dr. ir. M. Tichem. First Reader

Dr. ir. Q. Wang. Reader-two

Abstract

A neutrino is am intriguing subatomic particle with a high abundance in the universe. Due to its properties, it has a low interaction probability and can therefore travel from its source to its destination without deflecting from its course, and without losing much energy. The detection of neutrinos can help us understand various events happening in space and answer fundamental questions about the universe. Although neutrinos are abundant, it is very difficult to detect them as they do not often collide with matter. A solution is to create a detection volume as large as possible. One possibility to detect neutrinos is acoustic detection in the ocean.

The goal of the research described in this thesis is to design, optimize, manufacture and test a hydrophone that can be used to detect ultra-high energy neutrinos, when implemented in a large-scale telescope. The hydrophone used in this research is a transducer which converts acoustic pressure to strain in an optical fiber. Different design methods were investigated and the best design was manufactured and tested. The measurements were corroborated by numerical simulations using finite element method.

To be implemented in a telescope for the detection of ultra-high energy neutrinos the transducer has to meet a number of design requirements. Driving requirements concern the sensitivity and frequency range of the hydrophone. The transducer should have a frequency range from 1 to 50 kHz and the strain in the fiber as a function of applied pressure has to be optimized. Within the frequency range mentioned, it is preferable that the transducer behaves linearly. Consequently, the first eigenfrequency of the sensor should be above 50 kHz. Such a high eigenfrequency means that the sensor must be stiff and as this conflicts with the objective to maximize strain, a trade-off had to be made. The added mass effect, caused by the acceleration of a structure in a fluid, had an unexpectedly large effect on the dynamics of the transducer. This was investigated and accounted in the design process.

A surprisingly small variation of transducer concepts could be found in literature. This research investigated how (to what extend) topology optimization could contribute to the design of new concepts. A large amount of new concepts was conceived, however the translation from those concepts to real designs proved difficult. At the completion of this study, attempts to create an optimization that contained the right boundary conditions to simulate

pressure waves caused by a fluid, were partially successful. Preliminary results are reported in this thesis. The realization of a complete topology optimization for the design of acoustic transducers remains a challenge for future research.

In a following shape optimization approach, both a diaphragm and an inverse diaphragm type of transducers were parametrically optimized. To be able to make a good decision about the trade-off between frequency range and sensitivitiy, the optimization was done with the objective to maximize the strain in the fiber, while having different frequency ranges as a constraint. The diaphragm type turned out to be the concept with the best sensitivity in combination with the available manufacturing possibilities.

The design best suited for the neutrino detection was manufactured and tested in a basin. The experimental results corroborate the predicted behavior of the transducers as calculated using the finite element method. Although this was not confirmed by measuring the dimensions of the components of the sensors, it was estimated that the manufactured sensors are much stiffer due to manufacturing error.

The hydrophone has a frequency range until 40 kHz and a static sensitivity of 3.95 $\frac{\mathrm{n}\epsilon}{\mathrm{Pa}}$. It only shows a small difference in frequency response due to directionality below the eigenfrequency and behaves linearly. The designed hydrophones are suitable to be implemented in an telescope for ultra-high energy neutrino detection.

Keywords: Neutrino, transducer, fiber optic pressure sensor, acoustic detection of neutrinos

Table of Contents

List of Figures

List of Tables

Preface

Dear reader,

For me, a typical mechanical engineering student, fiber optical sensor technology was still a blank page in my mind at the time of starting this research. When I went through the literature on optical sensor technology and later when I went on designing, manufacturing and testing fiber optic pressure sensors, I experienced how varied the possibilities of this technology are. I also discovered how unexplored the possible variations for these kind of sensors were and still are, offering ample space for improvements and new opportunities.

Although topology optimization in my research proved to be difficult to apply in the design of the hydrophones, working with these topology optimizations is fascinating and for minutes, if not hours, I could stare at the changing topologies on my screen wondering where the design would would lead me this time. As satisfying as it was looking at those small pieces of changing topological art, it was equally frustrating that pitfalls, problems and imperfections of topology optimization are almost nowhere clearly described and sometimes even seem to be overlooked or ignored. This makes it difficult to to identify exactly what the possibilities and limits of topology optimization are.

TNO and especially my supervisors gave me the opportunity to do this highly interesting research in a stimulating environment. My thesis research provided me with everything I wanted, in particular a complete design cycle with the manufacturing and testing of my own sensors. I learned how to operate all the hundreds of buttons in Comsol, I experienced how fine yet strong thin glass fibers are and how (not) to break them while working with them. For the first time and with lots of pleasure I did real experiments. For all this I would like to thank my supervisors Ernst-Jan Buis, Jan de Vreugd and Matthijs Langelaar, who each in their own way provided support and motivation during this thesis! I would recommend anyone interested in neutrinos, to talk with Ernst-Jan, the driving force behind the ultra-high-energy-neutrino-detection-projects. Also I would like to thank Peter for the seemingly infinite amount of fibers and his kind help with testing the sensors. Arvind, Joris, Pjotr, Bart and Jernej also deserve some applause for making my time at TNO so comfortable and for the fun times we had inside and outside the TNO campus. Finally I would like to thank my parents, Sam, Jari and Wouter for their years of support and help during the many years I have studied.

Delft, University of Technology — L.M. Peeperkorn
November 13, 2018

Chapter 1

Introduction

This chapter includes the goal and motivation for this thesis and provides an introduction to the basics of acoustic neutrino detection. Section 1-3 deals with the workings of fiber optic hydrophones, and subsequently discusses several types of hydrophones found in literature and goes deeper into their design requirements.

1-1 Motivation and goal of this thesis

Many events happen in the universe. Some of them are well studied and can already be understood, but most events are still a mystery, that humankind is not (yet) able to explain. Neutrinos can help with understanding more about astrophysical processes and help answer fundamental questions about the universe. During multiple events in the universe, such as gamma ray bursts and supernovae, neutrinos are formed together with other particles like protons, photons and neutrons and are emitted into space. While protons are deflected by magnetic fields and photons are absorbed by interstellar matter, the neutrinos do not interact with microwave background and are not affected by magnetic fields. This special characteristic allows them to cross the universe in a straight line, retaining their energy, until they collide, possibly far away, from their source, as illustrated in Figure 1-1. This behavior is due to the fact that neutrinos are electrically neutral subatomic particles with a very small mass.

The detection of the collision of neutrinos with matter on Earth makes it possible to know their origin, as the neutrinos travel in a straight line from their source to the collision point. This allows us to study their source directly [2] and may make it possible to answer fundamental questions about the universe. A neutrino can be seen as a perfect messenger from its source, which could be the most violent highest-energy processes in our galaxy. In addition, it can give us insights about the mechanisms and processes of the non-thermal universe and can also complement cosmic ray studies and high-energy gamma ray astronomy [2].

Thus, to study space it would be logical to study neutrinos and luckily there is a vast amount of neutrinos traveling around the universe. Although the neutrino is the second most abundant known particle in the universe and billions of neutrinos pass through our own body each

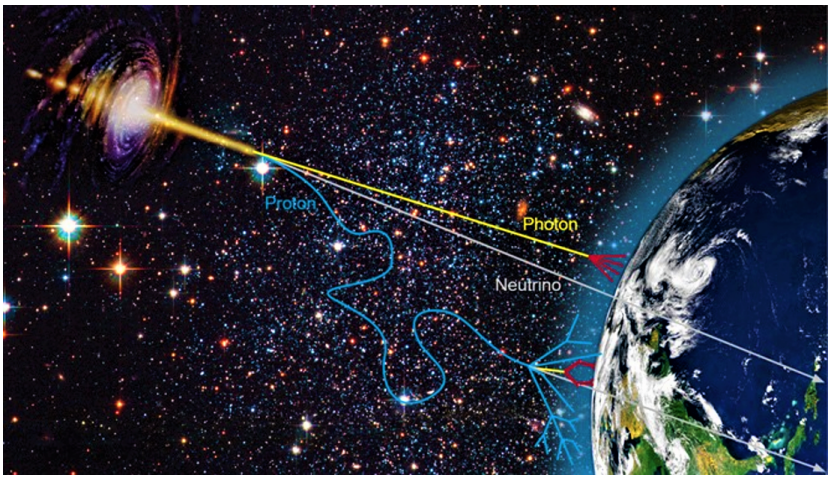

Figure 1-1: Neutrinos, protons and photons are formed during an event in space. The neutrino propagates in a straight line from its source to its destination [1].

second [3], it is not easy to detect them and they remain poorly understood.
Although it is difficult, humanity has found ways to detect different kinds of neutrinos and has built research facilities and telescopes solely for this purpose. Neutrinos are known to have a large range of energy, spanning from 1 μeV to 1 EeV and higher. The challenge for which we stand today is to solve the problem of detecting ultra-high energy neutrinos, which have an energy above 10 PeV.

Neutrinos are weakly interacting because they have a small size, mass and are electrically neutral. Hence, they travel in a straight path from their source to their destination and there is a low rate of interactions with matter. Figure 1-2 depicts the flux of neutrinos. It is inferred that with higher energy of the neutrino, the flux is lower. The expected flux of the ultra-high energy (UHE) neutrinos, those with an energy above 1 EeV, is smaller than $1/\text{km}^3/\text{year}$.

In other words: to detect a reasonable amount of high energy neutrino interactions, the detection volume of the telescope should be large. In the case of UHE neutrinos the detection volume should be above 100 km^3 [5], which is too expensive to realize with current technologies used in neutrino telescopes. The need for this large detection volume makes it logical to look for naturally available volumes. One of them is the water in the oceans and seas. It is isotropic and there are large areas that are relatively undisturbed.
One of the technologies with promising prospects to detect UHE neutrinos is acoustic neutrino detection in water, which is discussed in the next section. A large volumetric telescope is formed by deploying distributed arrays of pressure sensors, hydrophones, in the deep-sea. To realize such a large telescope, highly sensitive but economically viable hydrophones are required.

The goal of the research described in this thesis is to design, construct and test a hydrophone that can be used to detect ultra-high energy neutrinos, when implemented in a large-scale telescope.
In the following sections background information will be provided on neutrino detection. State of the art in the field of neutrino detection and the design requirements of the intended hydrophones for the UHE neutrino telescope will also be discussed.

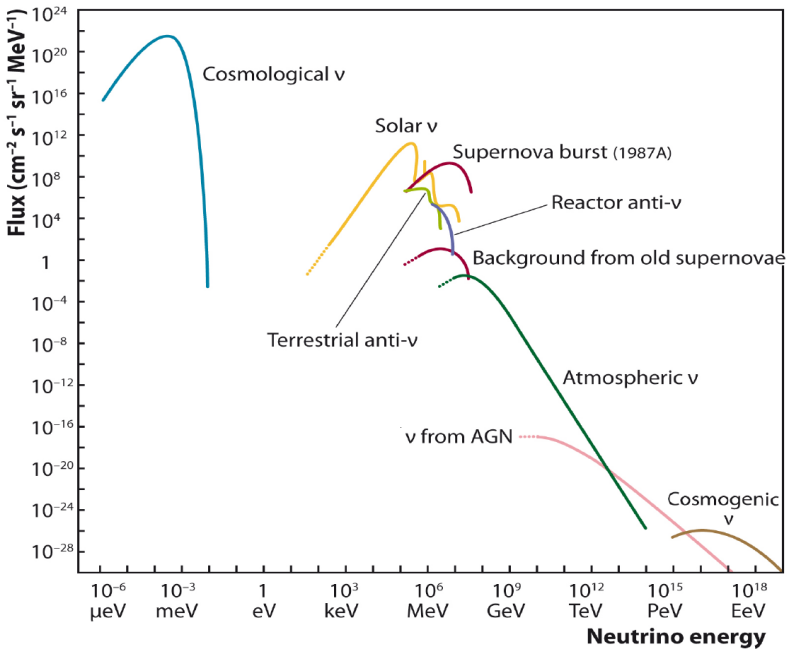

Figure 1-2: The flux of neutrinos as a function of its energy. Cosmological ν neutrinos have low energy, while the ones of interest in this research, the cosmogenic neutrinos, are typically in the order of PeV and EeV [4].

1-2 Neutrino detection

1-2-1 Neutrino interaction

A neutrino interaction with nuclei in matter may induce traceable signatures such as Cherenkov radiation (light), heat dissipation and radio waves as illustrated in Figure 1-3.

The Cherenkov radiation is a trace of light that propagates in the direction of the neutrino after collision. Photosensitive (optical) sensors can detect these traces of light [2].

Energy dissipation, starting at the point of the neutrino interaction, is found within a cylindrical volume of water of several meters long and a few centimeters wide. This energy dissipation causes a brief local instantaneous heating of the water, causing the water to expand and contract [6]. The temperature change resulting from the interaction from a 1EeV neutrino is 1 μK at a sea water temperature around 300 K. The relative change is only an effect in the order of 10^{-8} [1]. The expanding water causes a pressure pulse, an acoustic wave, that propagates away from the cylindrical source. The wave propagates in a flat disc like shape.
The precise shape and frequency spectrum of the wave are discussed later in this thesis.

Finally there is also electromagnetic radiation with frequencies of about 100 MHz to 1 GHz. Water is not transparent for these electromagnetic waves, thus detection of electromagnetic waves is only an option with ice or salt as a medium.

Table 1-1 shows the different attenuation lengths for the different neutrino interaction signals [3]. The attenuation length of the acoustic signal is very long compared to the other signals. When the attenuation length is larger, less sensors are needed to cover the same volume in a

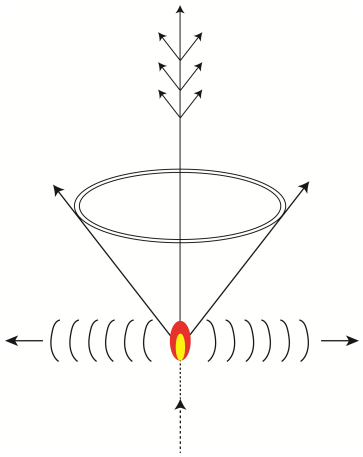

Figure 1-3: The interaction of a neutrinos with matter causes Cherenkov radiation, heat dissipation (and an accompanying acoustic wave) and a cone of radio waves.

telescope, accordingly with the same amount of sensors a larger telescopes can be constructed. Realizing a larger telescope results in measuring more high energy neutrinos. Hence, detecting acoustic signals provides an enormous advantages over other signals in a neutrino telescope.

Table 1-1: Attenuation length of signals from the neutrino interaction in different media.

	Sea water	Ice	Salt
Optical (Cherenkov)	50 m	100 m	0 m
Radio waves	0 m	few km	1 km
Acoustic waves (10kHz)	10 km	10 km	10 km

1-2-2 State of the art

The current set-ups for acoustic neutrino detection are mostly using acoustic arrays built for other purposes (for example military) or set-ups added to optical neutrino telescopes. This generally results in a telescope that is too small for the purpose of acoustic high energy neutrino detection. There are some acoustic telescopes built solely for neutrino detection, but the volume of those telescopes is not sufficient for UHE neutrinos. A large detection volume requires a higher number of sensors to be used in the telescope, thus making the telescope more expensive or even unfeasible to realize. The sensors that are used in most acoustic telescopes are piezo-electric hydrophones.

Figure 1-4 and Table 1-2 [3, 7] give an overview of different neutrino telescopes and the energy range of neutrino they are able to detect. As seen, some telescopes are able to detect neutrinos up to 10^{16} GeV. However, in practice many telescopes show to have difficulty to distinguish between a neutrino and another cosmic particle.

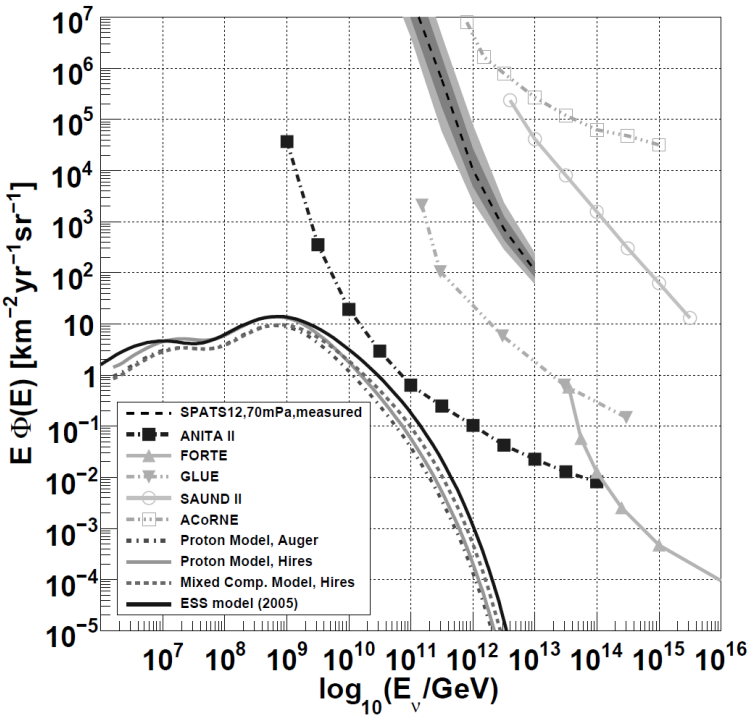

Figure 1-4: The detection limits of the current neutrino telescopes as a function of the energy of the neutrino [7].

Table 1-2: An overview of different neutrino telescopes [3, 7].

Experiment	Medium	Number of sensors	Range [GeV]	Type
SPATS	Ice	80	10^{11}	Acoustic
Lake Baikal	Fresh Water	4	10^{8}	Acoustic, Cherenkov
OvDE	Sea water	4		Acoustic
AMADEUS	Sea water	36		Acoustic
ACoRNE	Sea water	8	10^{15}	Acoustic
SAUND II	Sea water	49	10^{15}	Acoustic
KM3NeT	Sea water		10^{6}	Optical
Anita	Radio ice from balloon		10^{14}	Radio
Forte	Radio ice from satellite		10^{16}	Radio
Glue	Radio moon from Earth		10^{14}	Radio
Amanda	Ice		10^{8}	Cherenkov light
Antares	Sea water	300	10^{6}	Cherenkov light
Ice cube	Ice		10^{8}	Cherenkov light
Rice	Ice		10^{11}	Radio
Nestor	Sea			Cherenkov light
Auger	Air		10^{11}	Air shower

Extra attention is given to the KM3NeT collaboration. The research as presented in this thesis anticipates on plans from the KM3NeT collaboration concerning the development of

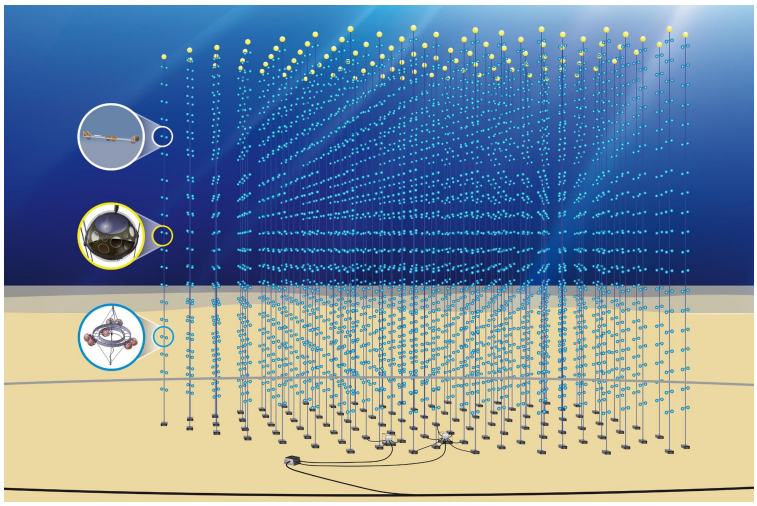

Figure 1-5: An artistic representation of the KM3NeT telescope [2].

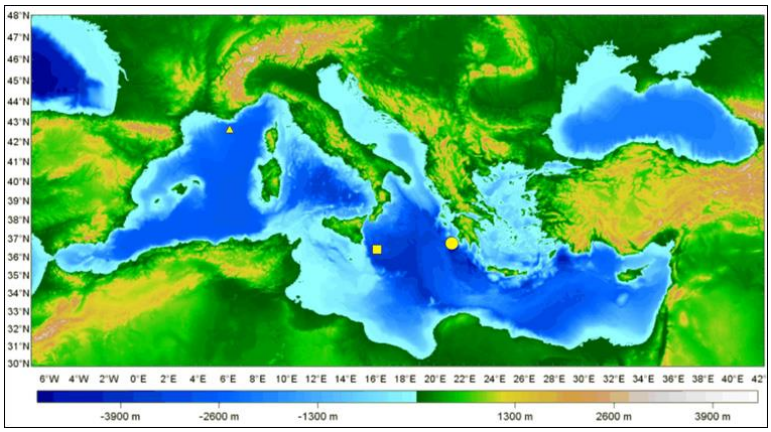

Figure 1-6: The possible locations for the neutrino telescopes of the KM3NeT. The triangle marks the Toulon site in the south of France, the square marks the Capo Passero site in the south of Italy and the circle marks the Pylos site in the south of Greece [2].

the future European deep sea research infrastructure in the Mediterranean. This new infrastructure will host the new generation of neutrino telescopes. About 240 researchers from more than 45 institutes and from 13 different countries will be active within the collaboration. The KM3NeT collaboration has designed and is currently deploying an optical neutrino telescope consisting of arrays of photosensitive detectors that are used to detect the Cherenkov radiation. A representation of this telescope is shown in Figure 1-5. Due to its volumetric limitations, it will only be able to detect neutrinos up to 1 PeV only. The KM3NeT collaboration has three preferred locations in the Mediterranean sea, they are presented in Figure 1-6. These locations have optimal conditions for an optical underwater neutrino telescope. In addition to the optical telescope there is also an option to build an acoustical telescope on one of these sites. The hydrophones discussed in this thesis were designed to be implemented in this acoustical telescope.

1-2-3 Functional requirements

It is crucial to know the functional requirements of the intended UHE neutrino telescope before jumping into the different types of hydrophones. The goal of this research is to design a sensor that can be used in the construction of a telescope that is able to detect UHE neutrinos with an energy above 1 EeV. In addition there is the wish to have an overlap with the optical KM3NeT telescope, which is designed to detect neutrinos with an energy below 1 PeV. Most of the requirements originate from the acoustic signal caused by the UHE neutrino and the medium in which the collision occurs. Some requirements are of a more practical nature and originate from financial constraints and the deep-sea working environment of the hydrophone. A deeper understanding of the working environment of the neutrino telescope as well as the acoustic signal of the neutrinos is needed, to determine the functional requirements of the hydrophone. These aspects are discussed in the next section, while the basic information about acoustic waves, how they propagate in the ocean and the units frequently used can be found in Appendix A.

Acoustic signal of the neutrino

The interaction of a neutrino with water produces a shower of secondary particles, in which the neutrino's energy is dissipated. This causes a local heating of the water, eventually creating an acoustic line source. This line source is a cylinder of several meters long and a few centimeters in diameter. The pressure pulses travel perpendicular away from this line source. The pressure pulses propagate in a pancake shape, with the height of the cylinder. For neutrino interactions with the energy between 1 EeV to 20 YeV, the disk has a height of approximately 10 to 100 meters and a diameter of several kilometers. Only a few degrees outside of the center plane of the disk, the amplitude of the acoustic pressure pulse is already almost non-existing. The amplitude versus the angle out of plane is depicted in Figure 1-7.

In equation (1-1) [8] and in Figure 1-7 an estimation of the mean pulse peak pressure [Pa], at 1 km perpendicular to the center of the 'line' source in sea water, is presented for neutrinos with different magnitudes of energy. In this equation E [GeV] is the magnitude of the energy of the neutrino, as seen the amplitude scales with E.

$$\log_{10}(p_{max}) = 1.0021(\pm 0.0018)\log_{10}(E) - 11.93(\pm 0.0012). \tag{1-1}$$

The pressure pulse is a typical bipolar pulse. At 1 km from the source of the UHE neutrino interactions, the energy is concentrated around 10 kHz [9][10]. For this signal, the best signal to noise ratio is in the frequency range between 10 and 50 kHz [11] (see Figure 1-8). Note that the absorption of acoustic waves is higher for a higher frequency, as shown in Appendix A, thus the waves at higher frequencies attenuate faster than at lower frequencies. Consequently, the frequency at which the peak concentration of the signal is located varies with distance from the source.

When multiple hydrophones detect the same bipolar pulse and when the shape can be reconstructed to the typical pancake shape, it is probable that the signal originates from a neutrino interaction. This shape reconstruction provides a handle to discriminate a neutrino event from other transients in the deep sea. Dolphins, other marine fauna and shipping traffic

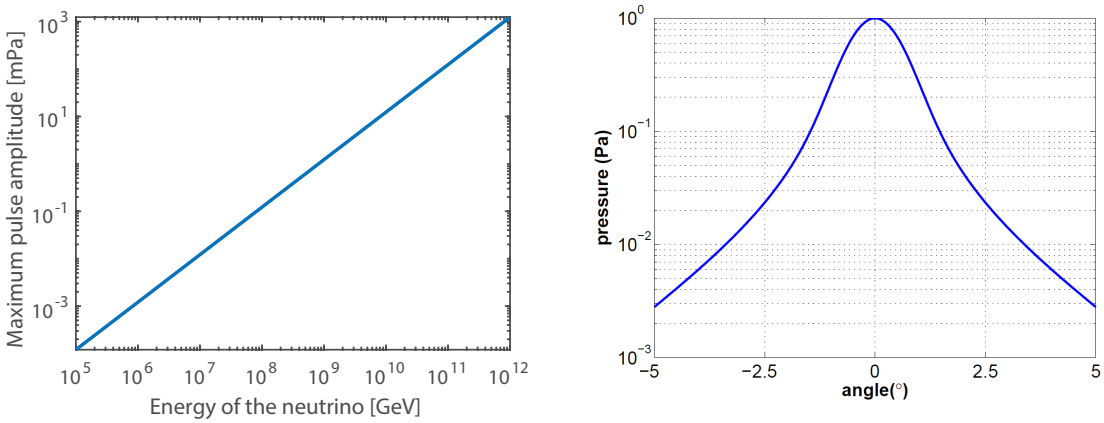

Figure 1-7: Left: the pressure amplitude of the signal at 1 km distance perpendicular to the center of the line source. It scales linearly with the energy of the neutrinos. Right: The pressure amplitude of a neutrino signal is quite sensitive to the out of plane angle [3].

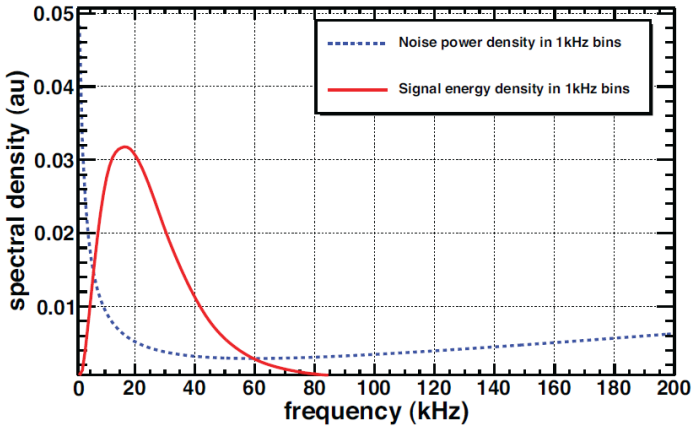

Figure 1-8: The signal to noise ratio is best between 10 and 50 kHz for a neutrino interaction at 1 km from the source [11].

can cause similar bipolar pulses, so it is of importance to reconstruct the acoustic event and to make sure the source of the sound is a neutrino interaction. Thus by extensive processing and filtering the data collected with multiple hydrophones, it is possible to distinguish the signal coming from a neutrino interaction from a signal coming from another transient noise source.

The propagation velocity of the acoustic wave depends on the density ρ and the bulk modulus, K, of the medium. This also means that the path of the acoustic wave deviates, depending on the velocity differences. This occurs, for instance when a wave travels between different depths. This is something that has to be taken in account when tracing back the pancake shaped signal of the neutrino.

Noise

It is not silent in the ocean, not even at a depth of 1 to 3 kilometers. These sounds interfere with the acoustic detection and are broadly classified as ambient and transient acoustic noise. The ambient noise in the ocean has different origins. Seismic and volcanic activity generate very low-frequency (<100 Hz) ambient noise. Shipping and industrial activity at the shore cause most of the ambient noise between 10 Hz and 1 kHz. Ambient noise between a few Hz and a few dozen kHz, is mostly caused by surface agitation, which is dependent on the sea state and the wind speed. At higher frequencies the ambient noise caused by thermal agitation is dominant.
The acoustic ambient noise in the ocean is so important because it limits the lowest pulse height of the neutrino signal that can be measured and thus it limits the sensitivity of the neutrino telescope.
Transient (narrow-band) noise mostly comes from marine animals like whales and shrimps. They can disturb the measurements of the telescope as it can be difficult to differentiate the signal coming from a neutrino interaction from the signal coming from another source.

The Sea State (SS) is a variable that describes the conditions of the ocean depending on the wind speed: when there is more wind (a higher sea state level) the sea is noisier. Sea state zero (SS0) is the state when the wind speed is very low and when there is a very calm sea, the water surface looks glassy, this is the state with the least noise. At sea state 1 the water surface is still calm, but there are small ripples, the wave height is up to maximum 0.1 m. At sea state 4 the conditions at sea are moderate. The ambient noise in the frequency range of interest (above 1kH) as a function of the sea state is described in literature by multiple models. In equation (1-2) the model by Urick [10] is presented. n_s is changed with the number of the sea state. In Figure 1-9 the different levels of sea states according to the Urick model, as well as the thermal noise, are depicted.

$$PSS0_{\,Urick} = 94.5 + 10\log_{10}(f^{\frac{-5}{3}}) + 30log_{10}(n_s + 1)\ [\text{dB re}\frac{(1\mu\text{Pa})^2}{\text{Hz}}]. \tag{1-2}$$

$$N_{thermal} = -75 + 20\log_{10}(f)\ [\text{dB re}\frac{(1\mu\text{Pa})^2}{\text{Hz}}]. \tag{1-3}$$

One flaw of the models is that the ambient noise is of course different for every location and that also the depth is not taken into account. In the paper by Kurahashi and Gratta [10] a depth dependent factor is experimentally determined at a depth of 1631 m. In this thesis the depth dependence of the ambient noise is not accounted for, as the noise at the location of the telescope is unknown and the dependency at the frequency range of interest is negligibly small.

Functional requirements

The ideal sensor can detect pressures as low as the ambient noise during sea state zero. In the case the sensor is able to measure those pressures, the noise in the ocean is the limiting factor, otherwise the sensor is the limiting factor. Furthermore, if the amplitude of the pressure that can be measured is smaller, less sensors are needed to cover the same volume of the telescope. The sensor should have a frequency range between 1 and 50 kHz, as is in this frequency range

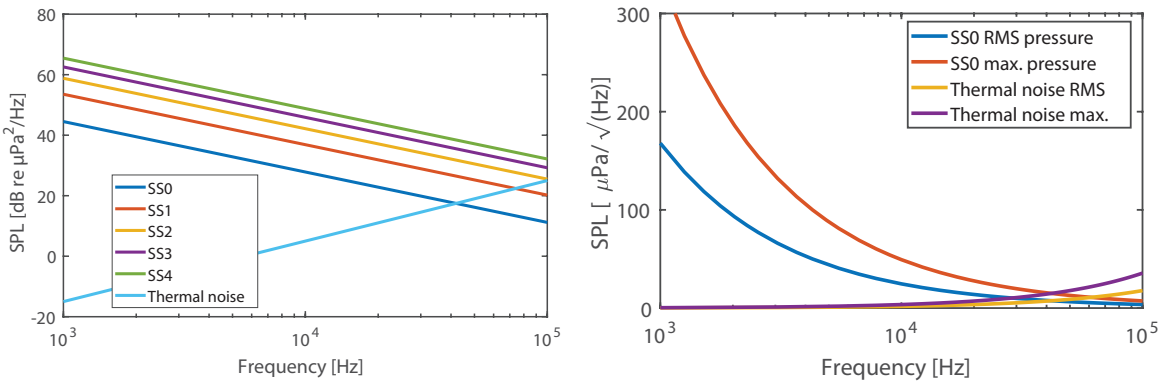

Figure 1-9: Left: Sound pressure level (SPL) of the ambient noise for different sea states (SS) based on the Urick model. The SPL of the thermal noise is also depicted. Right: The SPL for sea state zero (SS0) and the thermal noise.

the best signal to noise ratio is found. The sensor should exhibit minimal directionality, this makes it easier to reconstruct the original acoustic signal from the measurements of different sensors.

The sensor should operate in a deep-sea environment between 1 and 3 km depth, which is needed to achieve the large volume of the total neutrino telescope. Hence, the sensor should be able to withstand and work in high static pressure. The highest static pressure is at 3 km depth, at this depth the static pressure is approximately 300 bar (30 MPa). This means that while the static pressure is extremely high, small dynamic pressures have to be measured. To install the sensor it must absolutely be possible to transport the sensor from 0 to 3 km depth. The sensors will work in arrays installed in the sea and it will not be possible to completely fix their location, so the slow, almost static movements of the sensor in the water should not cause deviations in the measured signal.

The last requirement originates from the budget and the size of the complete neutrino telescope. For the telescope around 10,000 sensors will be produced and later installed, maintained and measured. The lower the costs of the (mass) production, the installation and the operational costs, the larger the telescope that can be built and the more neutrino interactions that can be measured.

1-3 Fiber optic hydrophones

A hydrophone can be driven by different mechanisms. Currently the most used mechanism is the piezo-electric hydrophone. The piezo-electric hydrophone has good sensitivity, high reliability and is already well established. The costs however for the piezo-electric sensor, in combination with the electrical wires and batteries that are needed to power all the sensors in the telescope, are relatively high, making this type not the ideal candidate.

An optical fiber hydrophone uses an optical fiber to measure acoustic pressures.
Some advantages of working with an optical fiber hydrophone are listed below:

- An optical fiber has a very low weight and small size.

- An optical fiber is immune to electromagnetic interference and disturbance .
- An optical fiber can withstand a high static pressure.
- Multiple sensors can be multiplexed on a single fiber (multiple sensors can work on the same fiber).
- Optical power losses are extremely small when using optical fibers, in the order of 0.03 dB per kilometer. Due to this low attenuation of the signal, remote measurements are possible.
- Optical fibers are cheap, although the interrogator needed to read out the fibers can be expensive.
- The sensors do not have to be electrically powered individually, this saves on operational costs during the measurements and on installation costs, as there is no need to have electrical wires going to every sensor.
- An optical fiber can withstand a wide range of high temperatures

It was decided to use the optical fiber hydrophone in the continuation of this research, because of these advantages. In the following section the working mechanism of the fiber optic hydrophone is explained. Subsequently the design requirements are set and also an effect, the added mass effect, that is caused by the interaction of a structure with fluid, will be examined. To conclude this section the concepts found in literature are shown.

1-3-1 Optical hydrophone

Optical fibers are usually made of thin threads of silica, that are used as cylindrical dielectric waveguides for the propagation of light. The optical fiber has a core and a cladding around this core. The reflection of the light rays remains completely internal and the light is trapped inside the core of the optical fiber, because the refractive index of the core of the fiber is higher than that of the cladding. Only when the fiber has a sharp bend the rays of light can escape. Silica fibers have very low optical losses, so an optical signal can travel for long distances in the fiber without losing significant energy.

Optical fibers are usually between 30 μm and 125 μm thick. The Young's modulus of silica is around 72.5 GPa and the Poisson ratio is 0.27. In literature the Young's modulus for fibers without coating is found to be 69.22 GPa [12]. Even though the optical fibers are thin, they usually have a high tensile strength, for uncoated fiber it is around 350 Mpa [12] and for coated fibers even around 5 Gpa. They are manufactured very precisely and have almost no (micro) cracks [13]. While the use of an optical fiber in harsh marine environments may cause the physical strength of the fiber to degrade, this effect was ignored in this thesis [12]. When the arrays with hydrophones are deployed in the sea water, it is highly probable that protection around the fiber will be present and that the effect of sea water on the strength of the fiber does not need to be accounted for.

There are multiple possibilities to design pressure sensors based on optical fibers: intensity based sensors, wavelength based sensors and phase modulated optical fiber sensors. Their

ability to multiplex (have multiple sensors on one fiber), their capacity to work in a stable manner outside of a laboratory environment and the fact that the sensor can be local and not distributed, are the reason why there was chosen to use a design with a wavelength based sensor.

With the wavelength based sensors a pattern, called a grating, is engraved in the optical fiber. The grating that is engraved is called a fiber bragg grating (FBG). It is a periodic perturbation of the refractive index of the core of the fiber. When a FBG is engraved in a fiber, this FBG acts as a wavelength selective mirror for the light traveling in the fiber. It reflects a narrow band of the wavelength spectrum that is proportional to the spacing of the FBG. This is shown on the left in Figure 1-10.
When the fiber with the FBG is strained, the spacings between the braggs become longer, resulting in a change in the reflected wavelength. This is illustrated on the right in Figure 1-10. The change in reflected wavelength is measured. The spacing between the braggs can be chosen such that there can be multiple sensors on one fiber, reflecting different wavelengths.

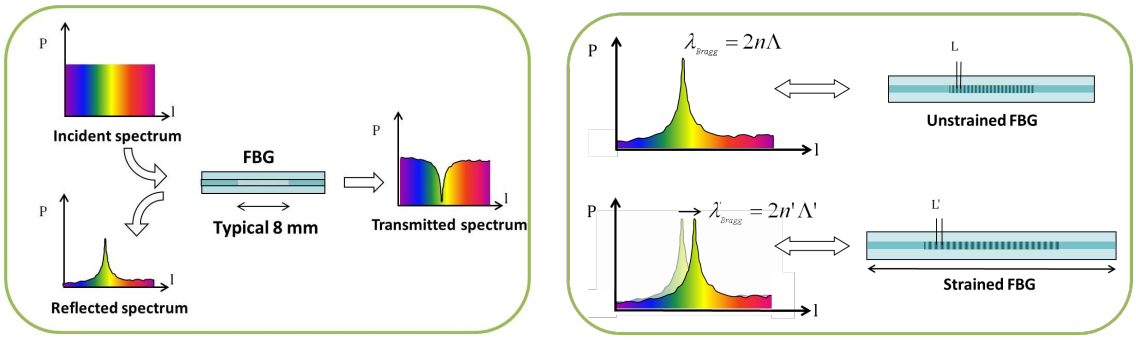

Figure 1-10: [14] Left: a small band of wavelengths is reflected by the fiber bragg grating. Right: there is a wavelength shift in the reflected wavelength when the FBG is strained.

A more recently developed method called a fiber laser has the advantage that the reflected bandwidth is smaller. This makes the measurements more precise. A fiber laser consists of two FBGs with in between a gain medium. This gain medium is a part of the fiber that is doped with erbium. When the erbium is brought into excited state, it will emit light between 1530 and 1570 nm. The light that is emitted depends on the wavelength that the FBGs reflect.
In Figure 1-11 two different types of fiber lasers are show: the π-shifted distributed feedback laser (DFB), where the cavity length is short and is half the period of the grating and the distributed bragg reflector (DBR) fiber laser, where the cavity length is in the order of the length of the FBG. The π-shifted DFB has the lowest laser gain threshold and it is less vulnerable to mode hopping, so this fiber laser method is preferred.

In earlier research by TNO in 2015 [15], the shortest DBR laser found was 7 mm long and the shortest π-shifted DFB laser was 17 mm long. Part of the 2015 TNO research was a design made for a π-shifted DFB with a length of 5 mm. This fiber laser design has not been produced yet. The π-shifted DFB has a lower noise than the regular FBG due to a smaller bandwidth of the reflected wavelength, it is 1 pm for fiber lasers and 0.1 nm for FBGs.

A note should be made on the effect of multiplexing multiple fiber lasers on one fiber. Up to 20 FLs can be engraved in one fiber [9]. When there are multiple sensors on a single fiber,

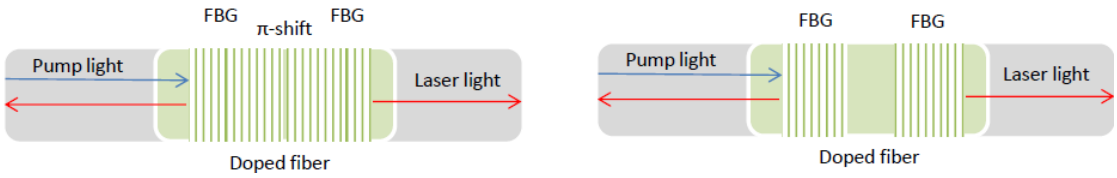

Figure 1-11: [15] Left: A π-shifted DFB fiber laser. Right: A DBR configuration.

the interrogator has to read out multiple wavelengths, which has an impact on the error.

1-3-2 Design requirements

The requirements for the detection of UHE neutrinos were laid out in the earlier sections. In this section some of those fundamental requirements are translated to practical requirements for the design of a fiber laser hydrophone.

Sensitivity

The sea state zero determines the sensitivity requirement for the minimum pressure that has to be measured. This requirement in Pascals is converted to a requirement on the minimum strain in the fiber per Pascal pressure. This requirement is valid when using a certain available optical fiber with fiber laser in combination with the measurement setup that is available at TNO.

The sensitivity calculation is illustrated in the following example:
At 10 kHz the noise at SS0 is 16.16 dB re $\frac{\mu \text{Pa}^2}{\text{Hz}}$, this is the minimum pressure amplitude that has to be measured. To measure this, the noise of the system has to be lower than the signal caused by the pressure.

The pressure wave causes a strain in the fiber at the location of the FL, this causes a wavelength shift of the reflected wavelength. This shift is calculated with equation (1-4) in which p_e is the effective photo-elastic coefficient, $\Delta\lambda$ is the wavelength shift and ϵ is the strain. p_e is approximately 0.22 and λ_B is 1550 nm. So the fiber laser sensitivity is approximately 1.2090 $\frac{\text{pm}}{\mu\epsilon}$.

$$\Delta\lambda_B = (1 - p_e)\lambda_B\epsilon = 1.2090\epsilon. \tag{1-4}$$

The measured noise of the fiber laser, in combination with the interrogator used at TNO and with an optical path difference (OPD) of 10 m, is depicted in Figure 1-12. It is -194.35 dB re $\frac{\text{nm}}{\sqrt{\text{Hz}}}$ in the whole frequency range of interest. Table 1-3 lists the expected noise of the interrogator for other OPD lengths.

Table 1-3: Noise interrogator for different OPD lengths.

OPD[m]	1	2	10	20
dB re $\frac{\text{rad}}{\sqrt{\text{Hz}}}$	-118	-115	-106	-103
dB re $\frac{\text{nm}}{\sqrt{\text{Hz}}}$	-186.35	-189.37	-194.35	-197.37

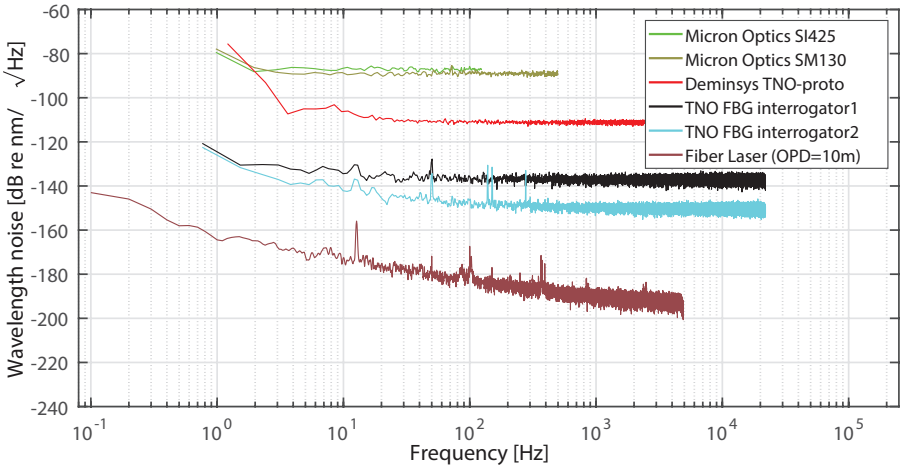

Figure 1-12: The measured noise of the fiber laser, in combination with the interrogator used at TNO. The noise is much larger when using an FBG or when measuring with the micron optics system.

The required sensitivity of the transducer in strain per Pascal pressure, to have a signal caused by the SS0 larger than the noise of interrogator with the fiber laser, was calculated by the formula in equation (1-5). N_{sys} is the noise of the system with the fiber laser, $PSS0$ is the noise in the ocean at sea state zero. This means that for example at 10 kHz and with 1 m OPD length, the transducer should strain the fiber by 16.29 $\frac{\mathrm{n}\epsilon}{\mathrm{Pa}}$ to be able to measure pressures as low as SS0.
The sensitivity requirements to measure different sea state levels with different OPD lengths is shown in Figure 1-13. The longer the OPD, the lower the requirement becomes for the strain sensitivity.

$$\text{Sensitivity} = \left(\frac{\Delta\lambda_B}{\Delta\epsilon}\right)^{-1} 10^{\frac{N_{sys}}{20}} 10^{\frac{-PSS0}{20}} 10^{12} \quad [\frac{\mathrm{n}\epsilon}{\mathrm{Pa}}]. \tag{1-5}$$

Frequency range

The signal to noise ratio between the acoustic signal from the neutrino interaction and the ambient noise is optimal between 10 and 50 kHz. Hence, the sensor should be operated in the frequency range between 1 and 50 kHz. It is preferred to design a sensor that has its first eigenfrequency above this range as it is easier to predict (a linear) behavior below the first eigenfrequency.

Dimensions

The sensor should be able to measure signals coming from every direction. This was achieved by setting a maximum size on the parts of the sensor that are influenced by the pressure: this size should be a lot smaller than the wavelength of the highest frequency that will

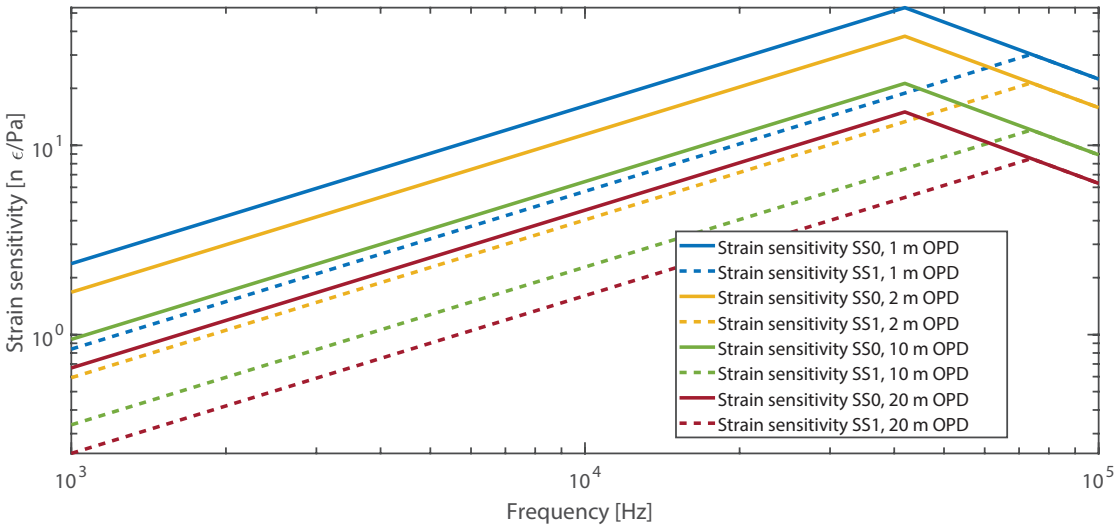

Figure 1-13: The strain sensitivity requirement to measure different sea state levels (including the thermal noise) with various OPD lengths of the interrogator.

be measured with the sensor in water. A quarter of the shortest wavelength will be the maximum dimension for the active components of the sensor used in the design. In Table 1-4 the maximum dimensions are listed for different frequency ranges. For a frequency range up to 50 kHz the maximum dimension is 7.25 mm.

Table 1-4: Maximum size components per desired frequency range.

Frequency [kHz]	Max. length [mm]	Wavelength [mm]
5	72.5	290
10	36.25	145
20	18.13	72.5
30	12.08	48.3
40	9.06	36.25
50	7.25	29

Currently optical fibers with fiber laser are not widely available. TNO has measured the noise of an optical fiber with fiber laser that was available in 2014 [15]. The properties of this fiber with fiber laser are used in this research. This optical fiber had a fiber laser of 20 mm in length and was 125 μm thick. It has been reported that fiber lasers with a length of only 5 mm and a thickness of 125 μm are possible to produce in the future [15]. In this thesis a fiber with a diameter of 125 μm, and a minimum length of the fiber laser of 5 mm, is used.

Static pressure

To be able to distinguish the small dynamic pressure changes from the static pressure at 3 km depth, the sensor needs to have some form of static pressure compensation. This pressure compensation mechanism also has to be able to compensate the pressure in the sensor when moving the sensor between different depths.

Costs

The costs to mass produce the sensors have to be low, this means that in the design the production should be taken into consideration.

1-3-3 The added mass effect

The added mass effect has a large impact on the dynamics and the eigenfrequency of a structure in fluid. A changing eigenfrequency impacts the frequency range of the sensor. When an object is moving in fluid, the fluid exerts forces on the object. When an object is moving at a constant speed the fluid only exerts a drag force, caused by the viscous properties of the fluid, on the object. However when the object has an acceleration, the fluid also exerts an extra inertial force.
The general equation of the forces on the body are [16]:

$$F = M_{solid}a + F_{drag} + F_{inertial} \tag{1-6}$$

$$F_{drag} = C_D \frac{1}{2}\rho v^2 S \tag{1-7}$$

$$F_{inertial} = M_{add}a. \tag{1-8}$$

C_D being the drag coefficient, ρ the density of the fluid, v the speed of the object, S the frontal area of the object and a the acceleration. The inertial force, $F_{inertial}$ consists of a constant, M_{add}, multiplied by the acceleration. This constant is called the "added mass" or "hydrostatic mass". The physical interpretation of this added mass effect is that when the body accelerates, it must also accelerate the surrounding medium.

The added mass is a function of:

- The size and shape of the body.
- The direction of the movement through the fluid with respect to an axis in the body.
- The viscosity and density of the fluid.

When looking at the general formula of the eigenfrequency, $\omega = \sqrt{\frac{k}{M_{solid}+M_{add}}}$, one can derive that the added mass decreases the eigenfrequencies of the transducer. This decrease can be very large and can decrease the eigenfrequency even by more than half. When the ratio between the mass of the solid and the added mass is smaller, this decrease in eigenfrequency is proportionally larger. This decrease is so large that this effect can not be neglected and thus it was taken into account during the design of the hydrophone.

The added mass is very complex to calculate analytically. Already for simple 2D shapes the calculation is quite complex, this is why the added mass of a variety of shapes is determined experimentally. When making a finite element method (FEM) model this effect can be included by combining two physics, a structural physics and an acoustic physics. The structural physics solves the mechanical equations for the elastic deformations of the sensor, while the acoustic physics solves the Navier-Stokes equations to find the velocity and pressure fields of

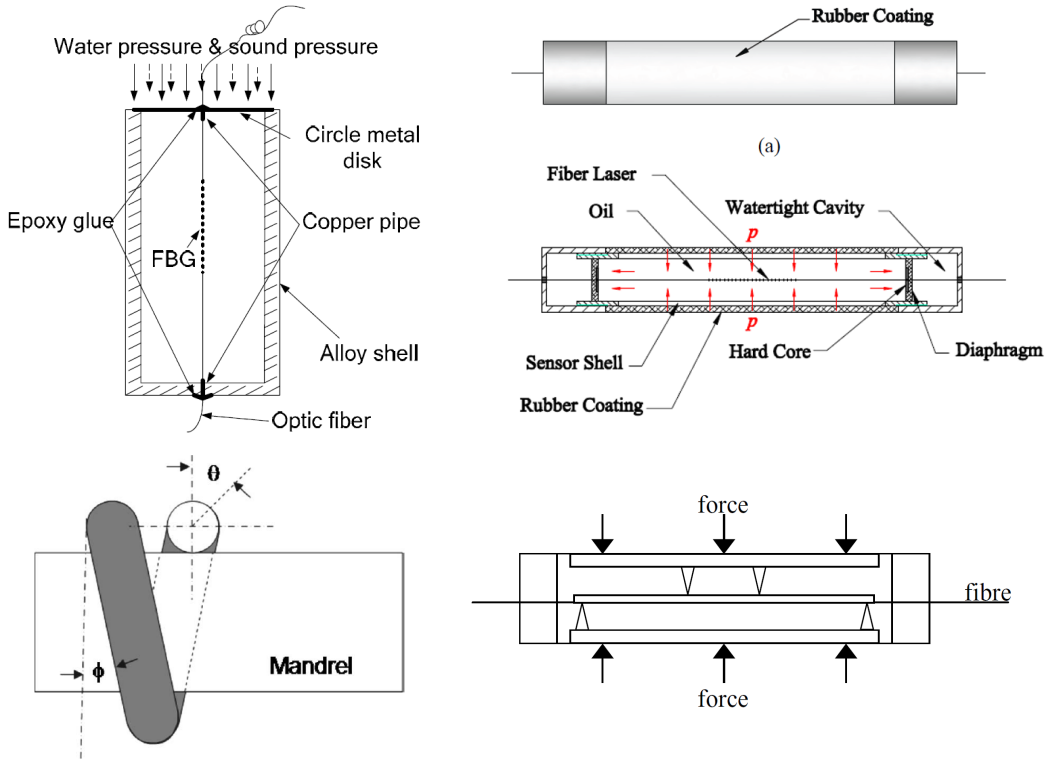

Figure 1-14: Different types of transducer concepts. Top; left: diaphragm [18], right: inverse diaphragm [19]. Bottom; left: mandrel [20], right: beam [21].

the fluid. On the fluid-structure boundary the equations are coupled to each other, for example: the velocity of the structure is coupled to the velocity of the fluid and on that boundary they must be the same. The acoustic physics was implemented by using an acoustic domain, filled with water, around the sensor.

1-3-4 Fiber laser hydrophone concepts

In a literature study [17] done before writing this thesis, different types of fiber laser hydrophone concepts were found. First of all, a bare fiber engraved with a FBG is also able to measure pressure changes. Due to pressure the fiber deforms slightly and has a strain of approximately 0.003 $\frac{n\epsilon}{Pa}$. This sensitivity does not however reach the requirements that were set in Section 1-3-2. In addition, a coating also does not enhance the sensitivity as much as needed. This means that it is necessary to implement a transducer that converts pressure to strain in the fiber.
Several types of mechanical transducer concepts were found: a diaphragm, an inverse diaphragm, a mandrel and a beam transducer. Drawings of the different transducers are shown in Figure 1-14. The diaphragm, inverse diaphragm and the beam work with the basic mechanism that the pressure out- and inside of the sensor is different and that this pressure difference deflects the active part of the sensor that is attached to the fiber.

Table 1-5 summarizes the sensitivities and the operational frequency range of the various concepts found in literature. Note that many papers are incomplete on relevant details, which

makes a direct comparison of the transducer concepts difficult. For instance, the diameter of the fiber is mostly not mentioned, but as the stiffness of the fiber scales with its diameter, it has quite an impact on the performance. Note further that no sensor that is found in literature was designed for the frequency range of our interest.

Table 1-5: An overview of different fiber optic hydrophone sensitivities.

Type	Freq. range (kHz)	Sensitivity $[\frac{n\epsilon}{Pa}]$	Validation method	Ref.
Bare fiber	15-100	0.003	Experimental/literature	[22]
Bare fiber		0.00301	Experimental	[23]
Bare fiber		0.0082	Experimental	[24]
Coated fiber		0.057	Experimental	[25]
Air backed teflon	2-10	0.1875	Experimental	[26]
Diaphragm	10	2.5	simulation	[27]
Diaphragm	1-3	11.7	Simulation/analytical	[28]
Diaphragm	0.4-10	3.78		[29]
Diaphragm	2.5-9	3.01	Experimental/analytical	[18]
Diaphragm	1-6.5	3 /0.95	Simulation / Experimental	[30]
Inverse diaphragm		6.07	Experimental	[31]
Inverse Diaphragm		5.79	Analytical	[19]
Mandrel	1-7			[20]
Mandrel				[32]
Mandrel		0.645	analytical	[33]
Mandrel	7	2	Sim./analytical/Exp.	[34]
Beam	1-3			[21]
Beam	9	2.5	Experimental	[35]
Beam TNO		6.3	Theoretical design	[9]
Unknown	1	2.9783	Experimental	[24]
Diaphragm TNO RVS	7.8	16.4 /12.65	FEA / experimental	[36]
Diaphragm TNO RVS	7.8	22.3 / 22.37	FEA / experimental	[36]
Diaphragm TNO ALU	4.7	46.1 /41.44	FEA / experimental	[36]

In addition to meeting the sensitivity requirements, the hydrophone must withstand high static pressures and filter out the low frequency acoustic waves that are not in the frequency range of interest. If this is not the case it is very difficult to measure the small dynamic pressure changes relative to the very large static pressure. Furthermore the hydrophone can collapse due to a large difference in pressure in- and outside of the hydrophone. In literature different types of static pressure compensation approaches were found.

One method for pressure compensation consists of incorporating a compartment filled with air into the design. The compartment can change in volume and is connected with the compartment in which the active sensor part of the sensor is accommodated. The connection is via a small hole that acts as a low pass filter. With slow pressure changes the air has enough time to move between the two compartments, for pressure changes at high frequencies the air is not moved between compartments yet and the active sensing part deforms due to the pressure difference.

Other methods are to connect the sensor to an external flexible bladder or to connect the

inside of the sensor with the water. Pressure compensation by filling the sensor completely with water is not suitable as water is almost incompressible and thus the active part of the sensor will not move with changing pressure. There is an option to have an internal bladder in the sensor that can fill with water, so that the air in between the bladder and the moving part of the sensor is pressure compensated.

When using a thin tube as low pass filter between an external air bladder and the inside of the hydrophone, the lowpass cutoff frequency is calculated as in equation (1-9) [35]. Above the cutoff frequency the sensor is sensitive to external pressures. f_c is the cutoff frequency, c_a the speed of sound in air, A the cross-sectional area of the tube, V_i the internal volume of the hydrophone and L the length of the tube.

$$f_c \approx (2\pi)^{-1} c_a \sqrt{\frac{A}{V_i L}}. \tag{1-9}$$

The bladder should have an appropriate volume. The minimum volume of the bladder at depth is calculated with equation (1-10). V_i is the internal volume of the sensor, V_e is the volume of the bladder, p_a is the atmospheric pressure, D the depth under water, ρ the density of sea water and g the gravitational constant. At 3 km depth, the maximum depth of the telescope, the volume of the bladder should be almost 300 times larger than the internal volume of the sensor.

$$p_a V_e = V_i \rho g D + V_i p_a \tag{1-10}$$

$$V_e = V_i \rho g D / p_a + V_i \tag{1-11}$$

$$V_e \approx 0.1 V_i D. \tag{1-12}$$

The volume of air needed for a sensor that should be pressure-compensated up to 3 km depth is 300 times bigger than the internal volume of the sensor. It will probably be most convenient to use an external bladder as otherwise the sensor itself becomes very large.

1-4 Focus and organization of this thesis

The goal of the research described in this thesis was to design, construct and test a hydrophone that can be used to detect ultra-high energy neutrinos, when implemented in a large-scale telescope. The basics about neutrino detection and fiber optic sensors were explained in this chapter. With this knowledge it is possible to continue to the next chapters in which the continuation of the design is discussed.
The focus during the design phase is on the different possibilities to design and optimize transducers that convert pressure to strain in a fiber. Although critical for the implementation of the hydrophone in the telescope, less attention will be given to the design of the pressure compensation mechanism.

In the last section it became clear that only a few concepts exist for the fiber optic hydrophone. Topology optimization is used to find inspiration for new transducer concepts, which is described in Chapter 2. In Chapter 3 different transducer concepts are parametrically optimized. After the optimizations, the final design and manufacturing of the hydrophone is reported in Chapter 4. In Chapter 5, the experiments with the manufactured hydrophones are described and the results are compared with the FEM models.

Experiments with the manufactured hydrophone can verify the behavior that is predicted by the FEM models. Thus another main focus of this thesis will be to manufacture and test a hydrophone, such that the dynamic behavior as predicted by FEM models can be verified by the measurements. In the last chapter the conclusions and recommendations are given.

1-4-1 Selection of the finite element package

During this thesis there will be extensive use of the finite element method. A FEM package, Comsol, was selected to be used. Comsol includes the physics (structural and acoustic) that are needed tot simulate the dynamic behavior of transducers in water. This package also has an extensive toolbox that can be used for topology optimization and parametric optimization.

To verify if the added mass effect can correctly be implemented in the simulations, two beams with known eigenfrequencies in water are modeled, the results are presented in appendix B.

Chapter 2

Topology optimization

A surprisingly small variation of transducer concepts can be found in literature. In this thesis topology optimization was used as a design tool in the creation of new concepts. Concepts that on their turn may form the foundation for new transducer designs that will ultimately come in use. In this chapter a general background about topology optimization is given followed by it's application to this research. Finally, the caveats and optimization issues that were encountered are discussed while showing a glimpse of the obtained results.

2-1 Background

The goal of topology optimization (TO) is to find an optimal design by an iterative process optimization of an objective function. During this process an algorithm can distribute material in a design domain to maximize/minimize the objective function. The TO is constricted by the design domain, constraints and the objective function. Although TO can be used to deliver a design that can almost immediately be used, often TO is used in the initial phase of the design process as a creative aid. In this research it was used for the latter purpose. The goal is to find compliant mechanisms that can work as a transducer and that have a better performance than existing systems.

The most basic TO problem works as follows: At the start of the optimization cycle, the domain is meshed and divided in a number of elements. Each element is given an initial virtual density between 0 and 1, such that 1 corresponds to an element completely filled with material and 0 corresponds to a void. There are multiple models to relate the virtual density, ρ, of the element to the Young's modulus of that element. In this research the Solid Isotropic Material with Penalization (SIMP) model was used: [37]

$$E = E_{min} + \rho^p(E_{solid} - E_{min}). \tag{2-1}$$

The Young's modulus, E, of an element can vary between E_{min} and E_{solid}. E_{solid} is the Young's modulus of the solid material, the lower bound of E_{min} is needed for numerical

stability. By implementing a constraint on the maximum amount of virtual density available for all elements together, the penalization factor, p, makes it uneconomical for an element to have an intermediate density. This helps to steer the virtual density of the element to 0 or 1. A typical value for p from literature is 3 [37].

For the TO used in this research the MMA (Method of Moving Asymptotes) algorithm was employed as optimization algorithm. This is an algorithm well suited for TO: it has been used frequently, seems to be efficient and has excellent convergence properties [37]. MMA, which is a gradient based algorithm, needs the gradient of the objective function with respect to the design variables to predict the next step in the iteration. The design variables are the virtual densities in each element of the mesh. The FEM package is used to calculate displacements or other properties that are needed to calculate the objective function during each iteration of the optimization cycle. The gradients, calculated by Comsol, are used in the next iteration to arrive at a new design. The complete TO process flowchart is shown in Figure 2-1.

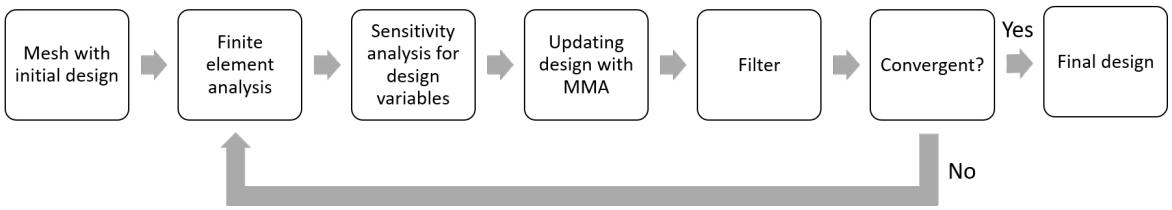

Figure 2-1: A flow chart of the topology optimization process.

The use of hydrostatic pressure loads in TO is complex. Pressure loads are design dependent as the pressure should only act on the boundaries of the design. Those boundaries are not constant and change with each iteration. Hence, the location, direction and magnitude of the pressure load changes at every iteration. In addition, boundaries of the design are usually not well defined during TO as the elements can have intermediate densities. Therefore, it is not clear on what boundary the pressure load should act. One way to include the hydrostatic pressure in TO is to find the loading surface at each iteration step [38]. Boundary detection is not easy to do when using a FEM program and thus a different approach was tried. This approach is presented in the following section.

2-2 The optimization model

To start the TO process, the requirements for the design of a fiber laser hydrophone as discussed in Chapter 1 must be recalled. In brief, there are requirements for the sensitivity (in various sea states), dimensions (signals from all directions), frequency range (between 1 and 50 kHz), static pressure and costs.
The basic TO set-up that was used for this research is presented in Figure 2-2.

The design space in which the optimization can distribute material is a quarter circle. In this design domain the Young's modulus can interpolate between E_{min}, with a value of 1 mPa, and E_{solid}, with a value of 1 kPa. Around this design space a layer of "soft" material was applied. The soft elements have a very low Young's Modulus (1 mPa) and a high Poisson ratio (0.49) and thus can deform, while keeping constant volume. With this method it was tried to approximate the behavior of water. On the outer boundary of the domain with soft

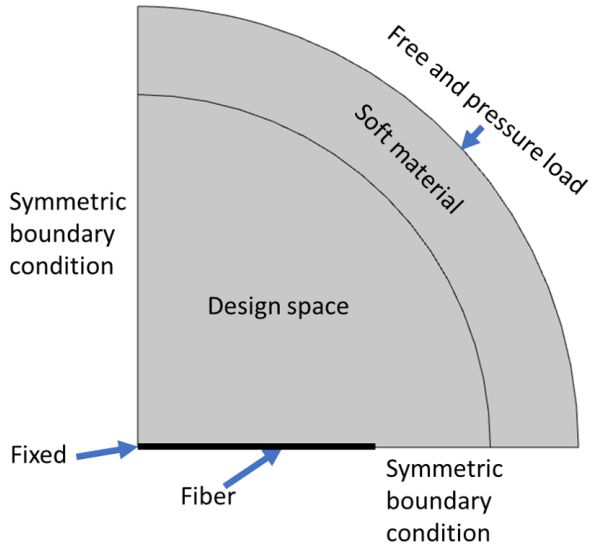

Figure 2-2: The model with most "basic" settings as used during the TO in this thesis.

material a pressure load was applied. The pressure load was 1 mPa, this value can not be much higher as otherwise the soft elements deform too much. The pressure load is passed on via the soft material to the elements in the design space.

The black line at the bottom of the figure is the fiber. The fiber has the Young's modulus of a regular fiber scaled to the Young's modulus of the solid material. The scaling was such that the ratio between the Young's modulus of the solid material to the Young's modulus of the fiber in the simulation, was the same ratio as the ratio between the Young's modulus of steel, the transducer material of choice, and that of silica glass. When the design can have material attached to the fiber at every point, the optimized design can load and bend the fiber in such ways that are not possible in reality. Solutions for this were to model the fiber as a spring or to have a gap, which is not part of the design domain, around the fiber.

The objective function was to maximize the displacement at the endpoint of the fiber, thus imposing maximum strain. It is important to normalize the objective function, the MMA solver performs best if the objective function in each iteration is between 1 and 100 for reasonable values of the variables. The element order of the elements used for the FEM calculations was linear. The maximum amount of inner iterations per outer iteration inside the MMA algorithm was set to 1. A typical constraint was to limit the maximum amount of virtual density available for all elements together to 40% of the design domain.

As TO requires some experience and feeling for correct settings, many simulations with varying settings were investigated. A lot of different models with many different boundary conditions, constraints and other settings were studied, some models are discussed here and in the following section. A more elaborate list of all the variations that were investigated is presented in Appendix C.
To limit computational time while finding the best settings for the optimization, the first optimizations were done in 2D. Simulations, with the same settings that worked well in 2D, were conducted later in a 2D-axisymmetric environment. The 2D optimization needed between 100 and 500 iterations to converge. The 2D axisymmetric models rule out a vast amount of good

designs because all the designs that are not axisymmetric can not be formed. Unfortunately 3D simulations required too much computational time and hence they were not completed. Selected results of the optimizations are shown in Section 2-4.

2-3 Caveats and optimization issues

Some important caveats and optimization issues that occurred during the TO are discussed below.

2-3-1 Eigenfrequency constraint

The frequency range is a crucial requirement for the design of the hydrophone. However, it is impossible to calculate the eigenfrequency of a design and its gradient during each iteration of the optimization with MMA in Comsol. Even if it were possible it would be difficult to calculate only the eigenfrequency of the solid elements and not those of the void or soft elements (which have a very low eigenfrequency).

Two ways to incorporate incentive to form structures with higher eigenfrequencies were studied. The first was to introduce a constraint on the elastic energy in the design. When the elastic energy has a maximum, the design domain should have a minimum stiffness. A stiffer structure can have a higher eigenfrequency, but this is not a certainty.
The second method was by incorporating a pseudo gravity. With the pseudo gravity the design domain was first optimized in the same way as with the basic TO simulations, with the same load, objective function and constraints. In a second step there was an additional calculation with a load case where there is a gravity load towards the middle of the circle, where the fiber was fixed. The gravity load scaled with the density of the elements. The movement of the structure at the first dynamic mode was simulated using this approach. By constraining the maximum elastic strain energy, the stiffness for that mode was forced to become higher, creating a higher eigenfrequency. Other examples of methods that were not tried are to have an input load at multiple frequencies with the objective function that the strain is maximized at each of these frequencies. The added mass, which influences the eigenfrequency in water, was not included in the optimizations. It is impossible to include this effect, when the acoustic physics is not used in the optimization.

2-3-2 Checkerboard patterns

Checkerboard patterns are numerical artifacts related to the discretization of displacements and densities. Two elements with high density that are only connected at one point form a very stiff link numerically. The checkerboarding is a known problem when using TO [37]. One solution to avoid checkerboarding is the implementation of a filter so that a solid element has to be connected to multiple other elements. A Helmholtz filter [39] was investigated and implemented in the optimization. With this filter a radius around an element with high density was chosen and within this radius the elements should also posses some density. The filter provided a good solution for the checkerboarding problem. The formulas used in the

Helmholtz filter are:

$$\nabla(-c\nabla\rho_0). + a\rho_0 = f \tag{2-2}$$

$$\nabla = \left[\frac{\partial}{\partial x}, \frac{\partial}{\partial y}\right]. \tag{2-3}$$

$$\tag{2-4}$$

c was -1, f was $-\frac{\rho}{fil^2}$ and a was $-\frac{1}{fil^2}$. The initial value and time derivative of ρ_0 was 0. With the constant, fil, the filter was coupled to the size of the elements, fil had a value of half the element size. A second manner to avoid the checkerboarding is by using higher order elements, however this increases the computational time.

2-3-3 Mesh dependency

The computational time rises with the amount of elements, hence the element size of the mesh can not be too small. This limits the resolution of the design. The implication of this is that no thin walled structures, such as a diaphragm, can be formed. Also, when a finer mesh is chosen, the optimal design can be different from that of a coarser mesh. Smaller structures can be formed, and thus there are more solutions. One approach is a restriction on the minimum size of structures, this was also done with the Helmholtz filter.

2-3-4 Discretization

There is a vast choice in options on how to discretize the elements in the TO simulation. The elements for the FEM calculations, the Helmholtz filter and also the optimization solver each have their own discretization. The element order and the shape function (Lagrange, Discontinuous-Lagrange, Serendipity,...) can vary for each of them. During simulations it was noticed that these settings had considerable impact on the convergence time and the resulting design. To study this effect and in order to find the best settings for the TO, a small study on discretization was done on a typical example in TO, the force inverter. This study is reported in Appendix C-2. The study was stopped after 14 combinations of different settings as it was found out that the settings that worked well for this problem, did not work specifically well for the hydrophone optimization. The numerical and discretization settings in TO problems turn out to be problem dependent. This makes it difficult to find good settings for new problems such as the sensor design problem studied here.

2-3-5 Stability

The optimizations showed very unstable behavior. The results were not reproducible, even when the simulations were rerun with identical settings. An example of this is illustrated in Figure 2-3. The instabilities occurred because the difference in the gradients in the elements was small at the first iteration. In such a situation a small numerical difference between simulations can already make the optimization move to another local optimum. Such a small numerical difference can for example be caused by processors, which do the calculations, that do not end simultaneously. To make the simulation more stable multiple solutions were conceived:

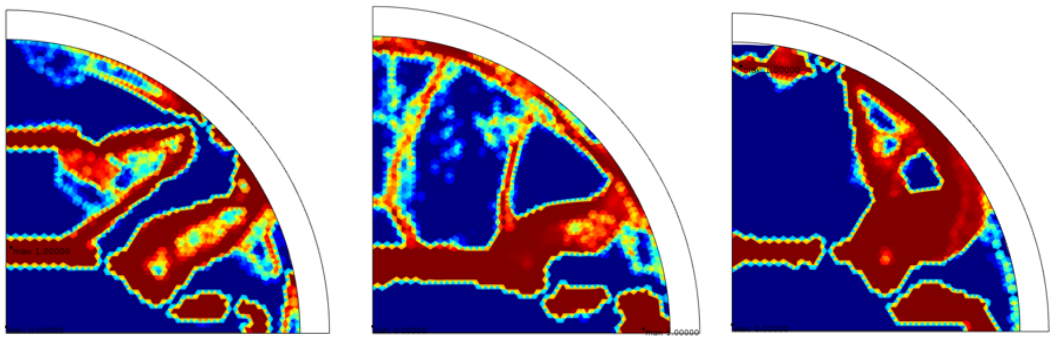

Figure 2-3: Three results of identical simulations are presented, they are very different from each other. Colors indicate the virtual density, red and blue depict the maximum and minimum density respectively.

- Smaller steps in the MMA (make the move limits in the MMA smaller) (not possible in Comsol).
- Start with a small penalization and make it bigger after a certain amount of iterations.
- Start without filter and then after some iterations use it.
- Other starting configuration, such as a gradient in the starting densities. In this way the objective function has a clear gradient in each element at the start.
- Different solver.

Some solutions were implemented, some improved the stability of the optimization, but none made the optimization completely reproducible, as there were still small differences between the resulting designs of the same optimizations. For typical TO test problems, where compliant mechanisms are formed such as the force inverter and the design of a bridge these problems did not occur. The difference between the hydrophone problem and the those typical TO test problems is that they do not have pressure loads, but rather prescribed displacements or a point load in one direction.

2-3-6 Closed boundaries

Additional to the problem with finding the boundaries on which the hydrostatic pressure load should act, the design should also have closed boundaries. A hydrophone only deforms under a hydrostatic pressure load when it's inside and outside are not connected. There was no procedure implemented on how to force the design to be closed, hence the loadcase implemented in the optimization was not representing the actual sensor use case. This resulted in designs that did not always had closed boundaries and therefore would not function with real hydrostatic loads.

2-4 Results and conclusions

The large amount of different settings made it possible to create the same amount of different simulation. Each simulation offered a unique solution to the hydrophone optimization problem. Four selected results of the optimizations in 2D are shown in Figure 2-4. On the left their underformed configuration is shown and in the middle and on the right the deformed configurations are shown. The deformed configuration shows how the design deforms under the pressure load, the movement is magnified such that it is visible. In the right column of the figure, the movement is more amplified than in the middle column. The most important settings of the TO, that diverged from the basic TO model, are listed in Table 2-1. Some of the 2D results, such as the one in the 2^{nd} and 4^{th} row have closed boundaries and will function with real hydrostatic pressure loads. The two other results do not have completely closed boundaries. Those design have to be redesigned to get them functioning under real pressure loads.

Table 2-1: The settings of the selected optimizations as seen in Figure 2-4.

1^{ste} row	2^{nd} row	3^{rd} row	4^{th} row
Helmholtz filter	Helmholtz filter Long fiber No soft boundary Gradient in begin design	Helmholtz filter Square design domain All elements with same volume	Helmholtz filter Pseudo gravity

Two selected results of the 2D axi-symmetric TO are shown in Figure 2-5. The TO resulting in the first design, at the top of the figure, differed from the basic TO as the design domain was a semicircle. The TO resulting in the second design, in the middle of the figure, had a higher order discretization of the elements. The designs include some carefully placed hinges and levers that create the working mechanism. In the bottom of the figure, close-up details of the second selected design are shown. Both designs in the figure include structures that were loaded as if there is a normal load and not a hydrostatic one. This was because the hydrostatic load was not represented well in the optimization. In a plot of the pressure in the elements of the designs, as provided in Figure 2-6, this can clearly be seen. The "branches" that deform the most and that cause the mechanism to strain the fiber, do not form a closed boundary, but yet are loaded by the pressure. Under a realistic hydrostatic pressure they would not deform.

Inspiration can be found for new transducer concepts from the results of the TO. The resulting designs of the TO in 2D, which had closed boundaries, can be translated to 3D concepts. There was no constraint on the eigenfrequency, hence the designs were not stiff and have a low eigenfrequency, thus the design should be adapted to reach a higher eigenfrequency. The translation of the 2D designs to good 3D concepts will take too much time and thus there was chosen to not do this in this research.

The 2D axi-symmetric results are easily translated to 3D concepts. Much the same as with the 2D designs they have to be adapted to have a higher eigenfrequecy. Unfortunately none of the results of the 2D-axisymmetric optimization showed closed boundaries on which the load acts and thus they can not be translated to new concepts. Although no hydrophones will be manufactured based on the results of the TO in this research, the TO simulations in this research form a good foundation for future research on the use of TO in the design of hydrophones.

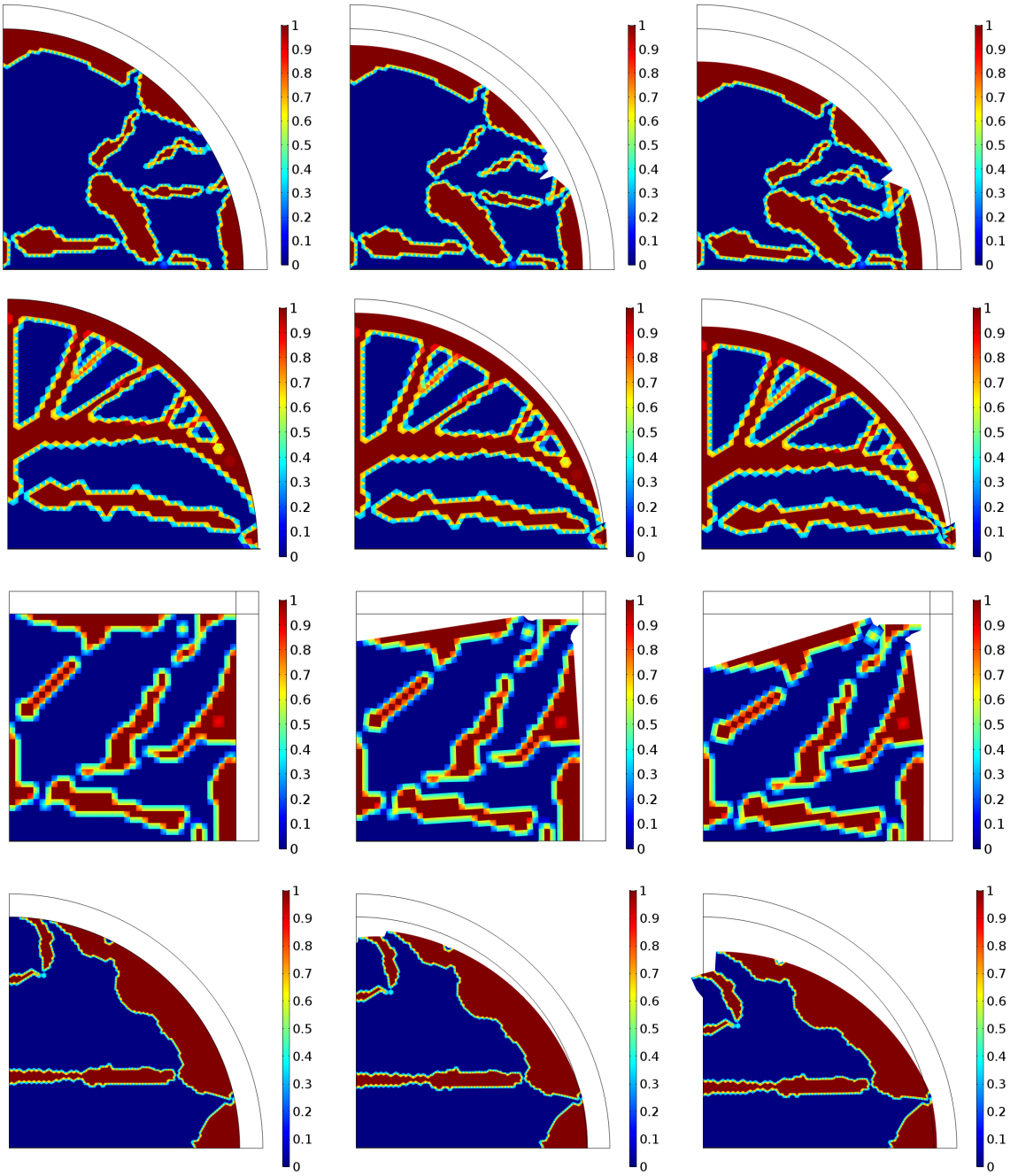

Figure 2-4: Results of the TO in 2D, colors indicate the material density. Red and blue depict the maximum and minimum material density respectively. The fiber is located at the bottom of the design domain. Left column: undeformed configuration. Middle and right columns: deformed configurations.

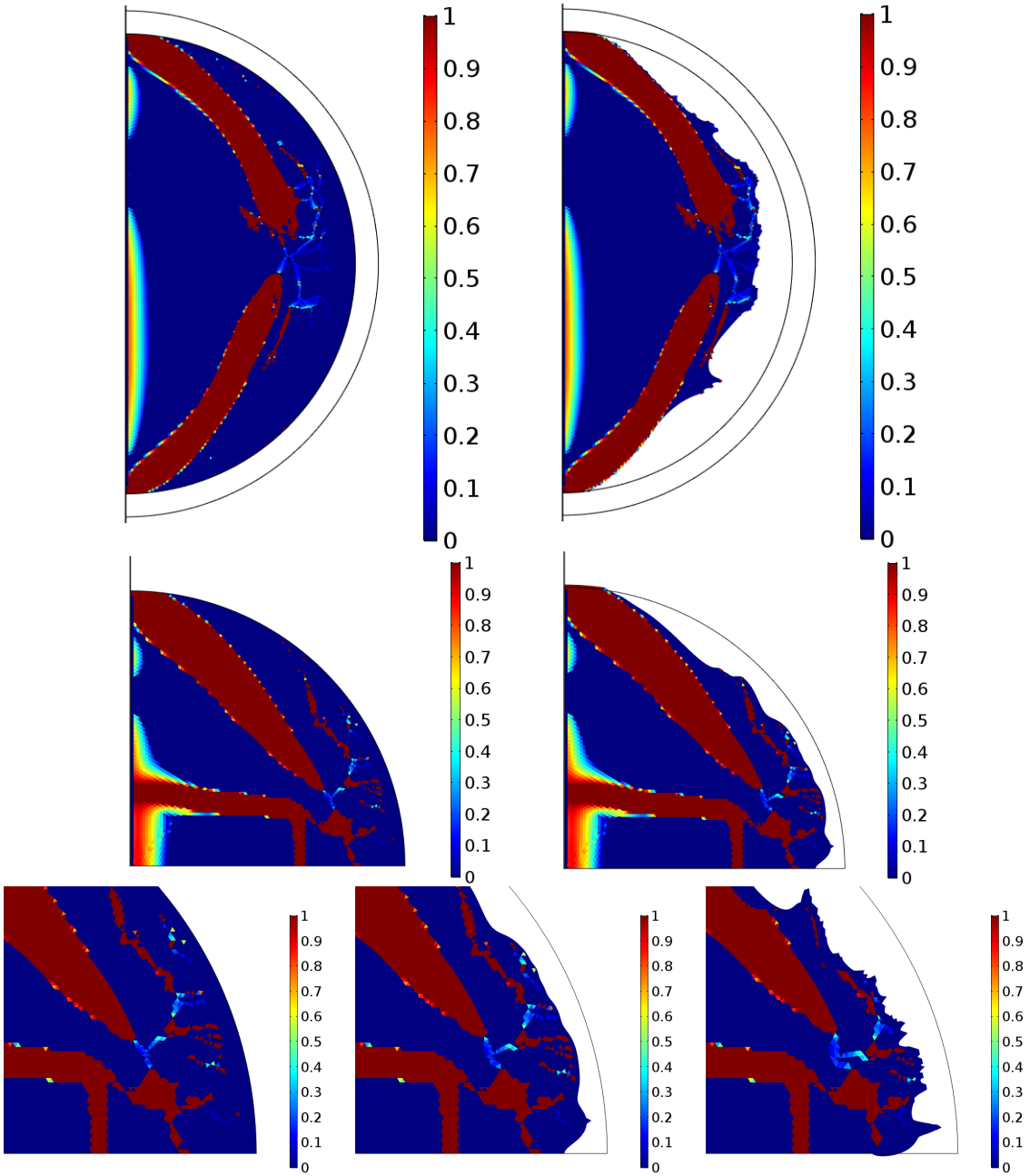

Figure 2-5: Results of the 2D axi-symmetric TO, colors indicate the material densities. The fiber is located on the left side, at the axis around which the design is rotated. Left column: underformed configuration. Right column: deformed configuration. Top: design 1. Middle: design 2. Bottom: close-up on the working mechanism design 2.

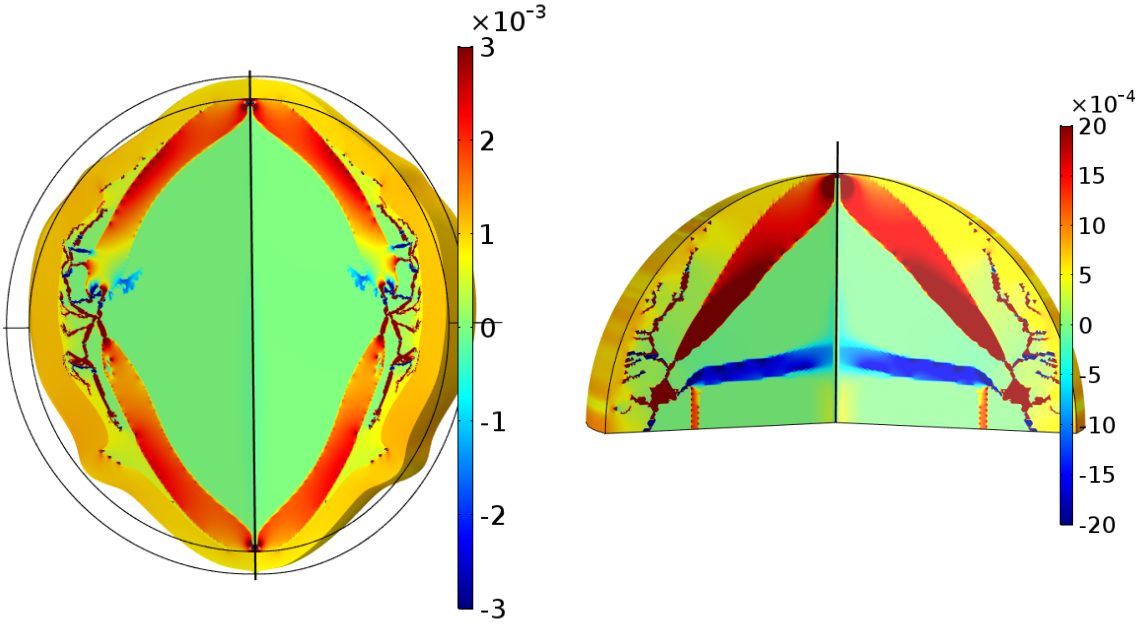

Figure 2-6: Pressure plot of the results from the 2D axi-symmetric TO, colors indicate the pressure. Red and blue depict the maximum and minimum pressure respectively. Left: pressure plot of design 1. Right: pressure plot of design 2.

Chapter 3

Parametric optimization

The concepts conceived by the TO were not suitable for parametric optimization and thus existing concepts needed to be optimized. As discussed in Section 1-3-4 several existing concepts were subdivided into four types of transducers: the diaphragm, the reversed diaphragm, the beam and the mandrel.
The diaphragm and the inverse-diaphragm type show promising sensitivities. However, Table 1-5 in Section 1-3-4 shows that there is a trade-off between the sensitivity and frequency range. This makes sense because when the diaphragm is stiffer, the first eigenfrequency is higher and inversely proportional the sensitivity becomes lower. The reversed diaphragm is less often described in literature, but the concept is based on the same basic mechanism as the normal diaphragm. The reversed diaphragm has one advantage over the normal diaphragm, namely that less to no prestress is required in the fiber. The beam type also shows approximately the same sensitivity to the same frequency range as the diaphragm type. There is more variation between the precise mechanical mechanisms of the beam transducers, several different hinges and reinforcement mechanisms were found in literature. It was anticipated that the manufacturing of the mandrel type of sensor is very difficult, as winding and glueing the fiber around the mandrel is difficult.

Due to time limitations it was not possible to optimize all different concepts. The diaphragm sensor was chosen to be optimized, it is a simple concept that is well known in literature and relatively easy to manufacture. There are not as many variations on this concept as with the beam concept, for which optimizing and investigating the different types of reinforcement mechanisms would take much time. The reversed diaphragm concept was also optimized as the optimization of this concept is much the same as the optimization of the diaphragm and it shows the promising advantage that no or less prestrain in the fiber is needed.
Figure 3-1 shows two examples of the two concepts.

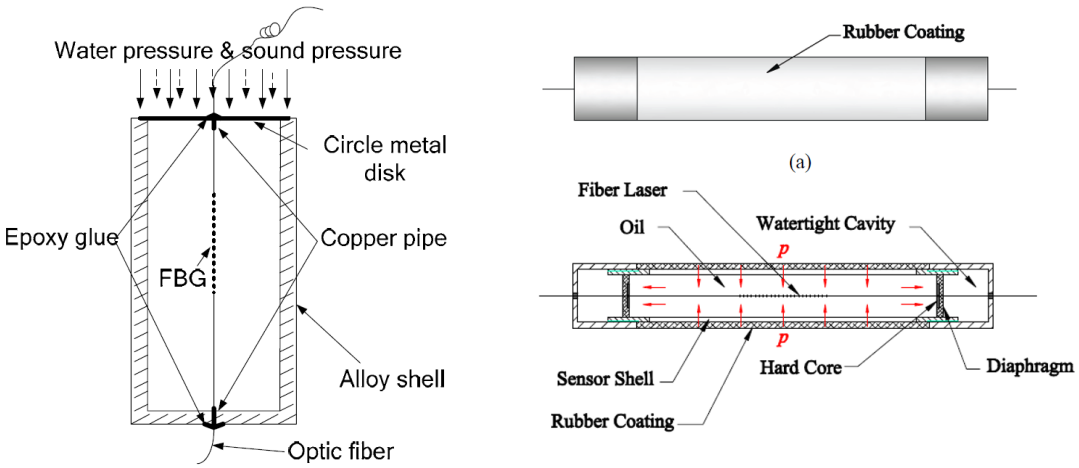

Figure 3-1: Examples of the two chosen types of transducer concepts that were parametrically optimized. Left: the diaphragm [18]. Right: the inverse diaphragm [19].

3-1 Optimization

With parametric optimization several dimensions of the transducer concept were optimized to achieve the highest sensitivity while respecting several constraints. In the next sections the constraints, objective function and the optimization algorithms are introduced. The FEM model used is checked and the implementation of the added mass effect, which has a big impact on the dynamic behavior of the transducer, is examined.

3-1-1 Constraints and objective function

The objective and constraints for the parametric optimization originate from the design requirements. The goal of the optimization was to maximize the sensitivity, this was translated to an objective function that maximizes the strain in the fiber for a static pressure on the transducer. The driving constraint was the frequency range of the transducer. Preferably this range is from 1 to 50 kHz because in this range the signal to noise ratio of the neutrino signal to the ambient noise is the highest.
To be able to make a decision on the trade-off between sensitivity and frequency range, various optimizations with different frequency ranges as constraint were conducted. This translated to a constraint on the minimum value of the first eigenfrequency of the transducer in water. Parametric optimizations with 10, 20, 30, 40 and 50 kHz as constraints for the eigenfrequency were done.

A quarter of the shortest wavelength was the maximum dimension for the width and length of the transducer. For different eigenfrequency constraints, different dimensional constraints were set as listed in Table 3-1. As the speed of sound in a medium is constant, the wavelength is shorter when the frequency is higher.

Table 3-1: Maximum size of the components as a function of the desired frequency range.

Eigenfrequency [kHz]	Max. length [mm]
10	36.25
20	18.12
30	12.08
40	9.06
50	7.25

The fiber laser, which has a length of 5 mm, has to fit inside the sensor and thus the height of the inside of the sensor was constrained to a minimum of 5 mm. The prototype of the sensor was manufactured in-house, which limits the minimum thickness of components. The minimum thickness of the diaphragms was 0.1 mm.

3-1-2 Algorithms

The parametric optimization of the design of the transducer was done using Comsol. The parametrization of the design will be introduced later, and is defined by several design variables. Because the design involves multiple parameters, an optimization algorithm was used to scan the parameter space.
Gradient based algorithms in Comsol are not compatible with the eigenfrequency study, so only gradient free algorithms could be used. The gradient free algorithms perform well with few design variables (<10), which limits the complexity of the design. The available algorithms were Monte Carlo, Coordinate search, COBYLA, BOBYQA and Nelder-Mead.

The algorithms and a short description of their working mechanism, with some (dis)advantages are briefly listed below [40].

- Coordinate search: Searches along one variable at a time, it estimates the gradient and then searches along the next variable.
- Monte Carlo: This algorithm selects the values of the variables randomly within boundaries. Only with a very dense statistic sampling it is possible to find a global optimum.
- Nelder-Mead: Using a first gradient approximation, it constructs a simplex and then improves the worst point. It is robust against noisy objective functions and can handle constraints.
- COBYLA: It stands for "Constrained Optimization BY Linear Approximation" and improves the objective function values by using an iteratively constructed quadratic approximation of the objective function. It requires a reasonably smooth objective function and it is fast.
- BOBYQA: It stands for "Bound Optimization BY Quadratic Approximation" and it uses a first order approximation gradient. It solves a sequence of linear approximations constructed from the objective function and constraint values sampled at the corners of a simplex. It can also consider constraints.

When the geometry is changed the mesh changes, leading to changing discretization errors for the objective function. Hence, the objective function was quite noisy as the control variables were all geometric dimensions. Initial assessment of all mentioned algorithms showed that in principle all could be applied. A detailed comparison is outside the scope of this thesis. Two algorithms were selected: Nelder-Mead, because this is the most commonly used, and COBYLA, because it turned out to be fast and obtained higher objective function values than others.

3-1-3 The added mass effect

The added mass effect was discussed in Section 1-3-3. This effect must be included in the optimization as it has a large effect on the eigenfrequency of the transducer.
The added mass of a flat circular disk that moves perpendicular to its surface is $\frac{8}{3}\rho r^3$, with r the radius of the disc [41]. Although the diaphragms of the concept are similar to a flat disc, it is not possible to blindly use this added mass estimation. There are some differences: the diaphragms in the optimizations are not flat and they deform during excitation. The middle part moves more than the outer part of the diaphragm and thus the movement is different from a translation. On top of this, the diaphragms of the transducers are only surrounded by water from one side, on the other side by air.

Although it is possible to include the added mass effect in simulations, which include an acoustic domain around the solid structures, there are two reasons to not conduct the optimization using such models:

- The simulation time increases and thus the whole optimization requires more computational time.
- When calculating the eigenfrequencies, the FEM package calculates the eigenfrequencies of the structure and those of the acoustic domain. It is not possible to automatically distinguish the structural eigenfrequencies from the eigenfrequencies of the acoustic domain.

Hence, the optimization used only the structural module with an estimated added mass added to the diaphragms. An estimation of the added mass was found by first calculating the eigenfrequency of the transducer in water, using a model which includes the acoustic module. Then an added mass was determined that, when added to the diaphragm, lowers the structural eigenfrequency such that it was equal to the eigenfrequency in water. To find a formula to estimate the added mass, a curve fit was done for multiple calculated added masses with different values for the geometrical variables. In the next sections the results of this process are presented.

A small remark about the effect of fluid depth: for a circular disk vibrating in a fluid, the effect of fluid depth can be neglected for depths larger than the diameter of the circular disk [42]. Looking at the dimensions of the sensors versus the depth in which the sensors will be deployed, it was concluded that an effect on the added mass caused by different fluid depths does not have to be taken into account.

3-1-4 FEM

The simulations were done in a 2D axisymmetric setting, which saved computational time compared to a 3D model. The objective function of the parametric optimization was evaluated with a static study by applying a pressure load on the outer sides of the transducer. The eigenfrequency constraint was evaluated by calculating the eigenfrequency in the structural physics of the FEM package while applying an added mass.
To simulate the behavior of the sensor in water an extra physics was added, the acoustic physics. An acoustic domain, in the form of a sphere of water around the transducer, was added to the simulation. On the boundary of the transducer with the water there was a fluid-structure interaction interface that coupled the structural physics with the acoustic physics, such that the transducer and water could influence each others dynamics. The structural-acoustic model is shown in Figure 3-2.

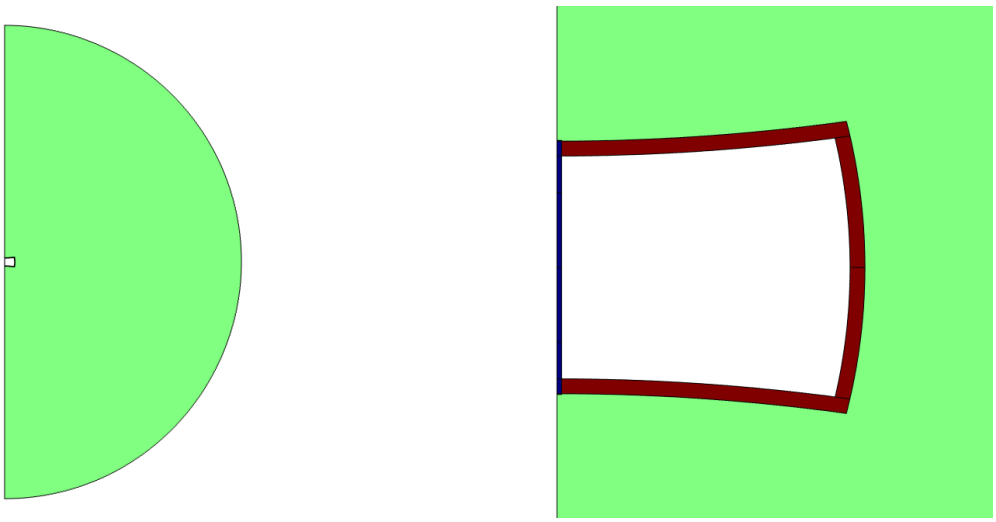

Figure 3-2: A FEM model including the structural and acoustic physics. The green area is the acoustic domain, with water as material. The red area is the transducer and the blue area, on the left edge of the figures, is the fiber, made of silica glass. The color white means that there is no material and that the white domain is not included in the simulations.

In appendix D the different FEM models that were used for the optimizations and the frequency response functions are shown. Special boundary conditions are highlighted. As conclusions and decisions are partially based on the results of the simulations, it is important to verify the accuracy and the reliability of the models. Convergence and error checks were implemented to check the reliability of the models.

3-2 The diaphragm

3-2-1 Design variables, objective function and constraints

In this section the diaphragm concept is parametrically optimized. The objective function of the optimization was to maximize the strain in the fiber at a static pressure of 1 Pa. The geometrical variables in this optimization were L, r_{cyl}, d, D, R_α and R_β, they are explained in Figure 3-3. The fiber is the line in the middle of the sensor, the transducer is axi-symmetric around this line.
Furthermore the material properties i.e. the Young's modulus E and the density ρ were variables. The last variable was the prestress that was applied on the fiber before glueing the fiber to the transducer. A prestress is needed to prevent the fiber from buckling when the diaphragms moves. This results in a total of 9 variables.

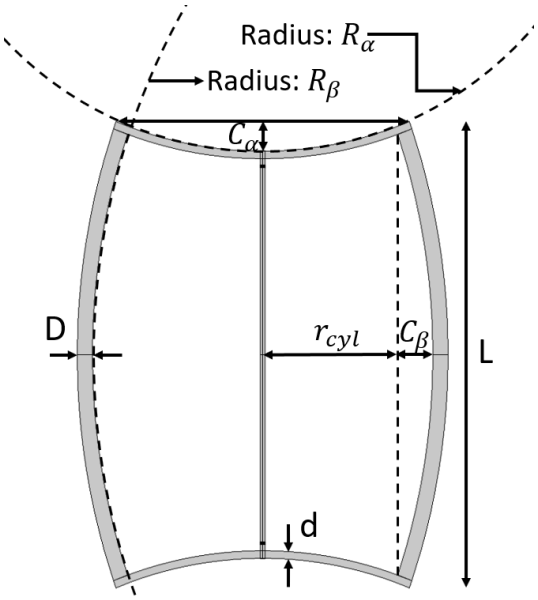

Figure 3-3: The geometric design variables as used in the optimization of the diaphragm concept.

To see which variables have negligible or substantial effect on the constraints or the objective function, sweeps of the variables were done. In a reasonable range the variables were swept over 10 values while the other variables remained constant, the structural eigenfrequency and static sensitivity were calculated. In Figure 3-4 the difference to the average, for the 10 different values of the variable, is plotted. When the effect of a variable is negligible it should not be included in the optimization, this can reduce the computational time and also make the optimization less noisy.

All geometrical variables have an effect on the eigenfrequency and the sensitivity of the transducer. The effect of the prestress in the fiber is negligible. Hence, in the optimization a prestress caused by 100 gram weight was used. As seen, the Young's modulus of the selected transducer material has a large effect on both the sensitivity and the eigenfrequency, while the density only has an effect on the eigenfrequency.
Since density also changes the ratio between the weight of the diaphragm and the added

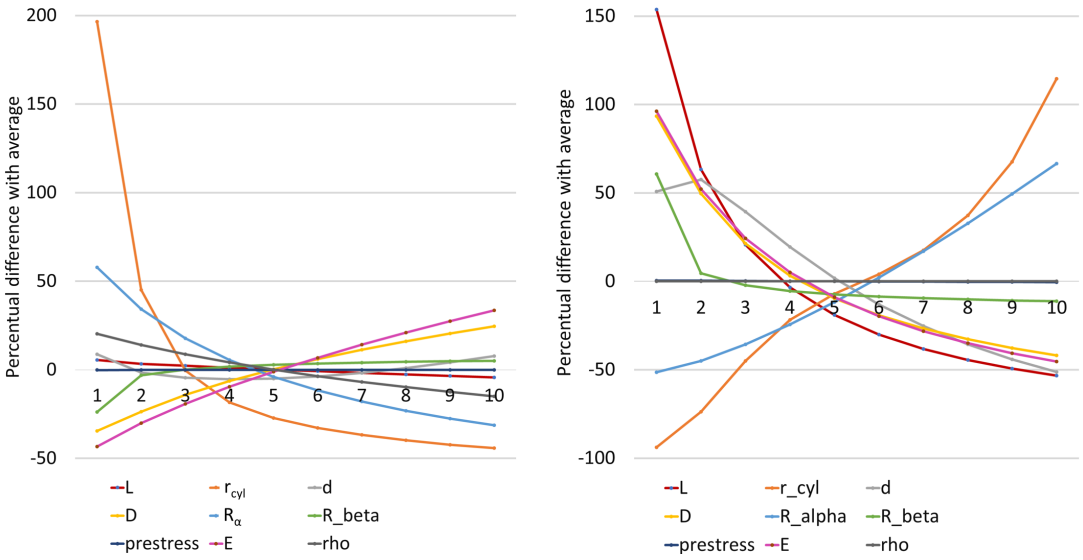

Figure 3-4: A sweep of the variables, in reasonable ranges, was conducted. In each range the eigenfrequency and sensitivity at 10 equally spaced points was calculated. Left: the effect on the eigenfrequency constraint. Right: the effect on the strain sensitivity.

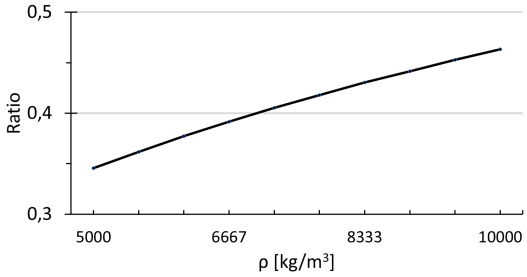

Figure 3-5: The ratio between the eigenfrequency in water and the structural eigenfrequency as a function of density .

mass, a higher density decreases the ratio between the structural eigenfrequency and the eigenfrequency in water. This is shown in Figure 3-5. Since a higher eigenfrequency in water increases the dynamic range of the transducer, a higher density is beneficial.

The geometrical optimizations were done with four different materials: aluminum, steel, iron and alumina. These materials were selected on their characteristics, which are listed in Table 3-2. As seen the ratio of the Young's modulus to the density of the material is very different for the materials, this was chosen such to see if very different ratios have a positive influence on the added mass in combination with the objective function.

Table 3-2: Material properties of different materials.

Material	Young's modulus [GPa]	Density $[\frac{\text{kg}}{\text{m}^3}]$	Ratio $[\frac{\text{GPa}}{\text{kg}}\text{m}^3 \cdot 10^3]$
Aluminum	71	2795	25.4
Steel	200	7850	25.48
Iron	140	7000	20
Alumina	300	3900	76.92

The optimization was constrained by a minimum value of the first eigenfrequency of the transducer. Furthermore the dimensions of the transducer were constrained to a maximum length, which was listed before in Table 3-1. Some geometrical variables were also constrained by geometrical feasibility. Table 3-3 presents an overview of all the constraints.

Table 3-3: The constraints for the parametric optimization of the diaphragm concept.

	Lower bound	Upper bound	Reason for constraint
First eigenfrequency	10/20/30/40/50 kHz		Required frequency range
L		$\frac{\lambda}{4}$	Quarter wavelength eigenfrequency
L		$2R_\beta$	Geometrical feasibility
r_{cyl}	Radius hole for fiber	$\frac{\lambda}{8}$	Quarter wavelength eigenfrequency
D	0.1 mm		Manufacturing constraint
d	0.1 mm		Manufacturing constraint
R_α	$r_{cyl} + D$		Geometrical feasibility
R_β	$\frac{L}{2}$		Geometrical feasibility
C_α		$\frac{L}{2} - d$	Geometrical feasibility
$\frac{L}{2} - C_\alpha - d$	$\frac{5mm}{2}$		Length fiber laser

3-2-2 Added mass estimation

The only two factors changing the added mass in this type of sensor are r_{cyl} and R_α, because they influence the part that moves the most in the first eigenmode . On the right of Figure 3-6 the added mass for different configurations of r_{cyl} and R_α is plotted, on the left the added mass is plotted in function of only r_{cyl}. r_{cyl} clearly has a large influence on the added mass while R_α has a negligible effect. It was chosen to perform a curve fit with a polynomial of the third degree, because the added mass of a flat circular disk is $\frac{8}{3}\rho r^3$. The curve fitted function for the added mass as well as the theoretical added mass function for a flat disc are also plotted in the left of Figure 3-6.

The fitted equation for the estimated added mass is:

$$M_{add} = 3312 r_{cyl}^3 - 14.02 r_{cyl}^2 + 0.06835 r_{cyl} - 0.000114. \tag{3-1}$$

This equation was used to add the added mass to the diaphragms during the optimization.

3-2-3 Results

The resulting values of the objective functions of the optimizations are presented in Table 3-4. Five different constraints on the first eigenfrequency were used, varied with 4 materials and 2 algorithms. The two algorithms sometimes showed very different results, although all the optimizations converged. An example of the convergence of the optimization is shown in Figure 3-7, this was an optimization with alumina as a material and an eigenfrequency constrained to 10 kHz. An explanation is that COBYLA is allowed to go slightly over the boundaries of the constraints during the optimization process and thus it has more possibilities to find a better local optimum. As the eigenfrequency becomes higher the diaphragms have

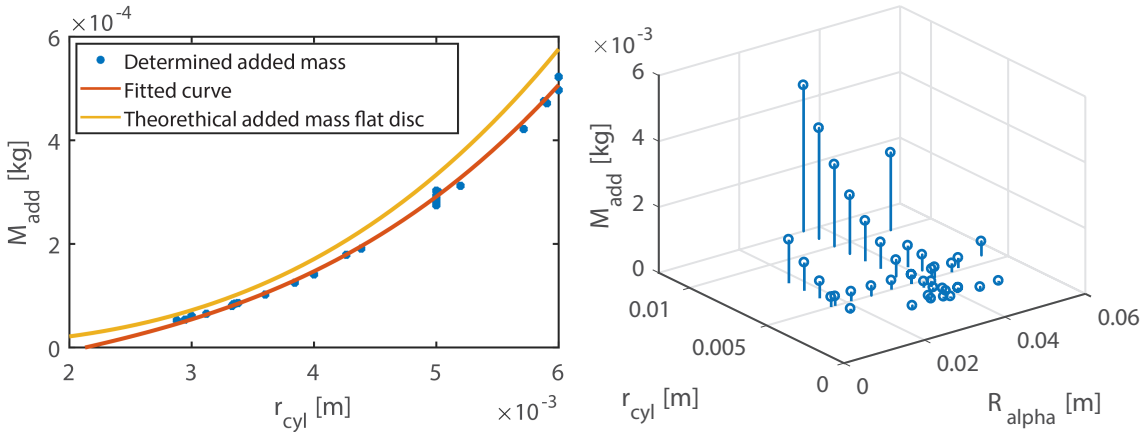

Figure 3-6: The determined added mass of the diaphragm in function of r_{cyl} and R_α. Left: the added mass in function of r_{cyl}. The fitted curve through these values and the theoretical added mass of a flat disk are also shown. Right: the added mass in function of R_α and r_{cyl}. R_α has negligible effect on the added mass.

a smaller diameter, are thicker and show less curvature.
A further discussion of these results follows in Section 3-4. Before that the optimization of the second concept, the reversed diaphragm, is presented.

Table 3-4: The obtained sensitivity values of the optimization of the diaphragm concept.

Eigenfrequency [kHz]	Aluminum $[\frac{n\epsilon}{Pa}]$	Steel $[\frac{n\epsilon}{Pa}]$	Iron $[\frac{n\epsilon}{Pa}]$	Alumina $[\frac{n\epsilon}{Pa}]$	Algorithm
10	22.63		19.80	23.76	COBYLA
20	9.09		7.99	8.92	COBYLA
30	6.23		5.45	5.61	COBYLA
40	4.50		4.46	3.85	COBYLA
50	3.87		4.01	3.59	COBYLA
10	21.28	14.19	17.97	14.50	Nelder-Mead
20	8.62	7.52	7.50	7.90	Nelder-Mead
30	5.42	4.73	4.99	5.10	Nelder-Mead
40	4.01	2.68	3.42	3.13	Nelder-Mead
50	1.91	1.14	1.21	1.28	Nelder-Mead

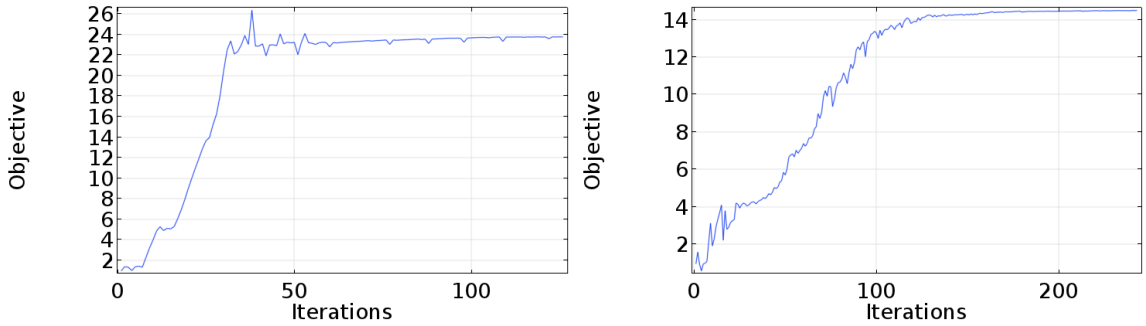

Figure 3-7: The value of the objective function versus the iterations of the optimization. With both algorithms the objective function converges. Left: COBYLA. Right: Nelder Mead.

3-3 The reversed diaphragm

3-3-1 Design variables, objective function and constraints

In this section the reversed diaphragm concept is optimized. In Figure 3-8 the reversed diaphragm concept is illustrated, with its variables r_{cyl}, d and L. It consists of two separate hollow cylinders, each having a membrane that deflects with a pressure difference between the in- and outside of the cylinders. When the pressure outside is higher, the membranes move inwards and the fiber is more stretched than before. The two cylinders are set at a fixed distance from each other using a rigid construction, such as bars. The horizontal line depicts the fiber.
The two materials that were used for the optimization were aluminum and steel. The objective function was again to maximize the strain in the fiber for a 1 Pascal static pressure load on the outside of the sensor.

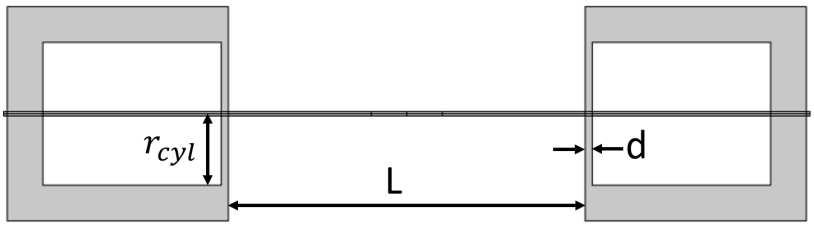

Figure 3-8: The variables for the optimization of the reversed diaphragm concept.

Table 3-5 presents a list of constraints. The lower bound of r_{cyl} was the size of the hole for the fiber. It was chosen to not include a possible curvature in the diaphragm as it was found that for the "normal" diaphragm optimization, the optimizations showed a trend towards a flat diaphragm when the eigenfrequency constraints were high.

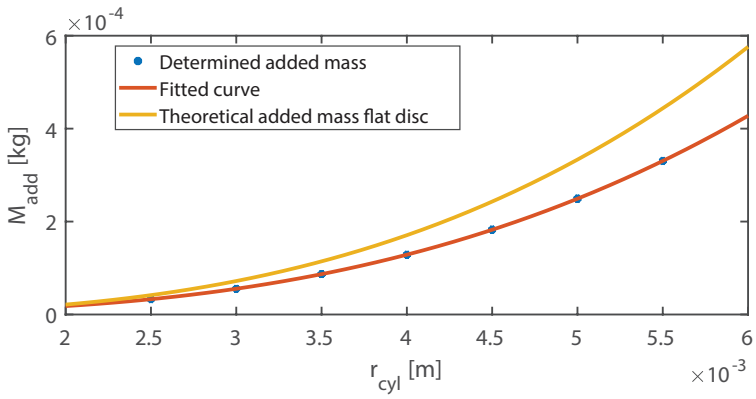

Figure 3-9: Estimated added mass for the reversed diaphragm in function of r_{cyl}. The theoretical function of the added mass for a flat disk and the determined added mass are also shown.

Table 3-5: Constraints for the parametric optimization of the reversed diaphragm.

	Lower bound	Upper bound	Reason for constraint
First eigenfrequency	10/20/30/40/50 kHz		Required frequency range
r_{cyl}	0.1	$\lambda/8$	Quarter wavelength eigenfrequency
d	0.1 mm		Manufacturing constraint
L	5 mm		Length fiber laser
L		$\lambda/4$	Quarter wavelength of eigenfrequency

In a similar way as for the regular diaphragm a function to estimate the added mass was determined. The function of the estimated added mass is:

$$M_{add} = 1828r_{cyl}^3 + 1.598r_{cyl}^2 - 0.005456r_{cyl} + 8.01 \cdot 10^{-6}. \tag{3-2}$$

It is plotted in Figure 3-9.

3-3-2 Results

The resulting values of the objective function for the optimizations are listed in Table 3-6. Five different eigenfrequency levels were used as constraint, varied with 2 materials and 2 algorithms. All the optimizations converged and much the same as with the optimization of the diaphragm, the obtained sensitivities between the two algorithms were different.
A further discussion of these results follows in 3-4.

Table 3-6: The obtained sensitivity values of the optimizations for the reversed diaphragm concept. NM stands for the Nelder-Mead algorithm and CB for COBYLA.

Eigenfrequency [kHz]	Aluminum CB $[\frac{n\epsilon}{Pa}]$	Aluminum NM $[\frac{n\epsilon}{Pa}]$	Steel CB $[\frac{n\epsilon}{Pa}]$	Steel NM $[\frac{n\epsilon}{Pa}]$
10	20.68	20.62	19.02	10.88
20	8.09	8.08	7.27	6.88
30	4.65	4.60	4.12	4.12
40	3.11	3.09	2.74	2.71
50	2.27	2.21	1.97	1.96

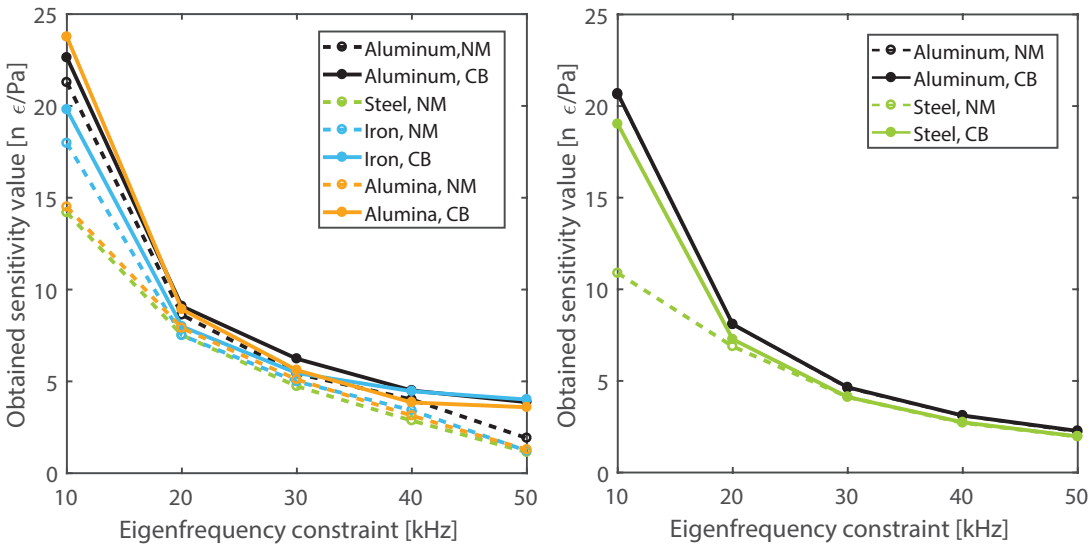

Figure 3-10: The obtained sensitivities of the optimization for both concepts, with 2 algorithms and 4 materials. NM stands for the Nelder-Mead algorithm and CB for COBYLA. Left: the results for the normal diaphragm. Right: the results for the inverse diaphragm.

3-4 Comparison and choice

In Figure 3-10 the obtained sensitivities for both concepts are shown. On the left the results of the normal diaphragm are shown and on the right those of the inverse diaphragm. For both concepts and all the materials the trade-off between the eigenfrequency constraint and the sensitivity is seen clearly. As the eigenfrequency constraint becomes higher, the obtained sensitivity decreases. So obtaining a sensitive sensor with a higher bandwidth is a challenge. Both concepts show comparable sensitivities for the higher eigenfrequency levels which are of the biggest interest. It was anticipated that manufacturing the diaphragm concept is slightly easier than the reversed diaphragm. Less parts have to be bonded together and the fiber only has to be glued twice and not four times to the transducer. This is why the diaphragm type was chosen to be the preferable concept.

The optimization of the normal diaphragm with aluminum as material performed well for both algorithms. As aluminum is also a material that is cheap and easy to manufacture in-house, this material was chosen to be the material of the transducer.
To make a better comparison between the different results of the optimizations of the diaphragm concept, the frequency response functions (FRF) of the optimized aluminum designs, loaded by an acoustic wave, were calculated. These are shown in Figure 3-11. As seen, the eigenfrequency in the FRFs differ from the estimated eigenfrequency of the optimizations. To illustrate: 40NM has an eigenfrequency at 36.7 kHz, while the optimization was constrained to a minimum eigenfrequency of 40 kHz. For the optimization using COBYLA, the differences in eigenfrequency were larger. For example 50CB, which was constrained to a minimum of 50 kHz, shows an eigenfrequency of 35.4 kHz in it's FRF. This is because the estimation of the added mass, especially with smaller radius of the diaphragm, was not perfect. This flaw can be due to the boundary conditions of the acoustical model that was used during the estimation of the added mass.

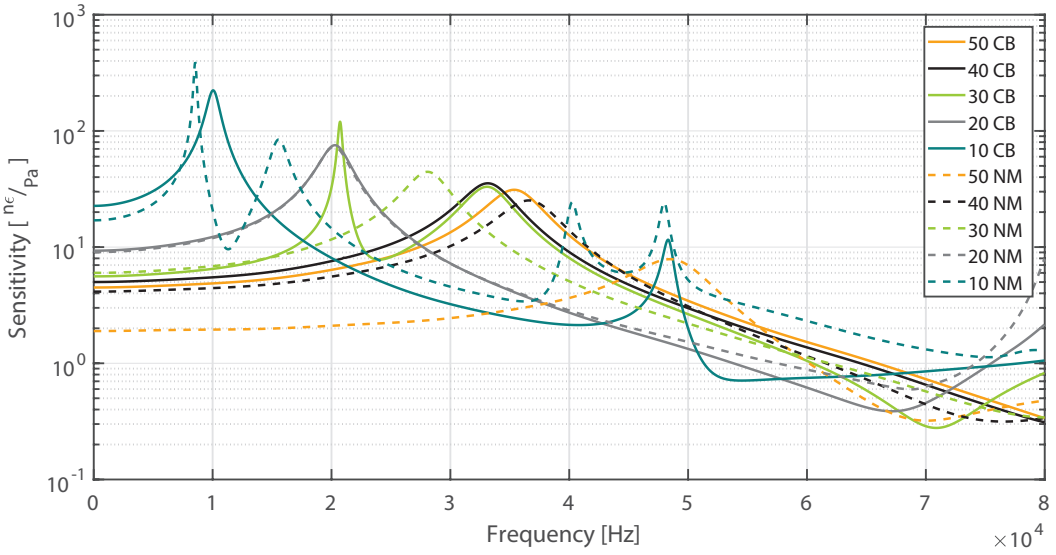

Figure 3-11: The frequency responses of various optimized designs. The numbers in the legend represent the value of the eigenfrequency constraint in kHz and NM/CB indicates if the Nelder-Mead/COBYLA algorithm was used.

In Table 3-7 the dimensions of the geometrical variables of selected optimized designs are presented. These four optimized designs come into consideration because of their relatively high eigenfrequency and not extremely low sensitivity. The 50NM optimization shows a very low sensitivity, thus it is not included in the table. As seen, 30NM, 50CB and 40CB are very close to the minimum limit of the thickness of the diaphragm, d, which is 0.1 mm. A thinner diaphragm provides a challenge during manufacturing. 40NM has the longest length. When the length of the sensor is close to the length of the fiber laser, which is 5 mm, the alignment between the FBG and the transducer has to be very precise.
Due to these two favorable aspects the 40NM concept was chosen as the design that was going to be manufactured. The details of the final design and the manufacturing process of the hydrophone are discussed in the next chapter.

Table 3-7: Dimensions of selected optimized designs [mm]. The number represents the value of the eigenfrequency constraint in kHz and NM/CB indicates if the Nelder-Mead/COBYLA algorithm was used.

	r_{cyl}	D	d	R_β	R_α	L
40 NM	2.73	0.44	0.19	21.67	29.59	5.66
30 NM	2.73	0.36	0.13	21.39	29.82	5.53
50 CB	2.30	0.41	0.10	33.07	25.48	5.42
40 CB	2.46	0.37	0.12	20.91	34.76	5.42

Chapter 4

Final design and manufacturing

In the previous section the design procedure was discussed and the optimized design that can be manufactured was chosen. In this chapter the details of the resulting design are given. The manufacturing process and realized hydrophones are shown. Also more detailed FEM simulations were conducted to predict the behavior of the hydrophone, the results of which are presented in this chapter.

4-1 First design sensor

The dimensions of the chosen design from the optimizations are shown on the left in Figure 4-1 and as one can observe the diaphragm and the outer wall of the transducer are curved. The possibility to simplify the design in favor of a manufacturing which restricts itself to what is necessary was investigated. One option for such simplification is shown on the right in Figure 4-1. The difference in the FRF between the two designs is small, as shown in Figure 4-2. For this reason it was decided to choose the non-curved design.

The static sensivity of the sensor, i.e. the sensivity at a frequency of "0 Hz", is expected to be 3.95 $\frac{\mathrm{n}\epsilon}{\mathrm{Pa}}$. The required fiber prestrain is provided by hanging a mass of 100 grams off its lower end. After attaching the prestrained fiber to the diaphragm, the diaphragm deflects 1.508 μm in the middle and the fiber has a strain of 573.9 $\mu\epsilon$. The prestrain should be such that when the hydrophone (without pressure compensation) is 10 m under water the fiber is still strained and does not buckle. The maximum depth at which the sensor was tested was about 10 m. The strain induced by a static pressure at 10 m depth is 386.9 $\mu\epsilon$, the prestrain realized by 100 gram weight is sufficient.

As the effect of the wavelength of the acoustic wave to the length of transducer was not known, it was also decided to produce the same kind of transducer with a length that was three times as large. Thus, the requirement of the maximum length can be derived and adjusted in later studies. With the longer sensor it is also possible to study the effect of directionality, when the acoustics waves travel in other directions towards the hydrophone. The design of these longer sensors is shown in Figure 4-3.

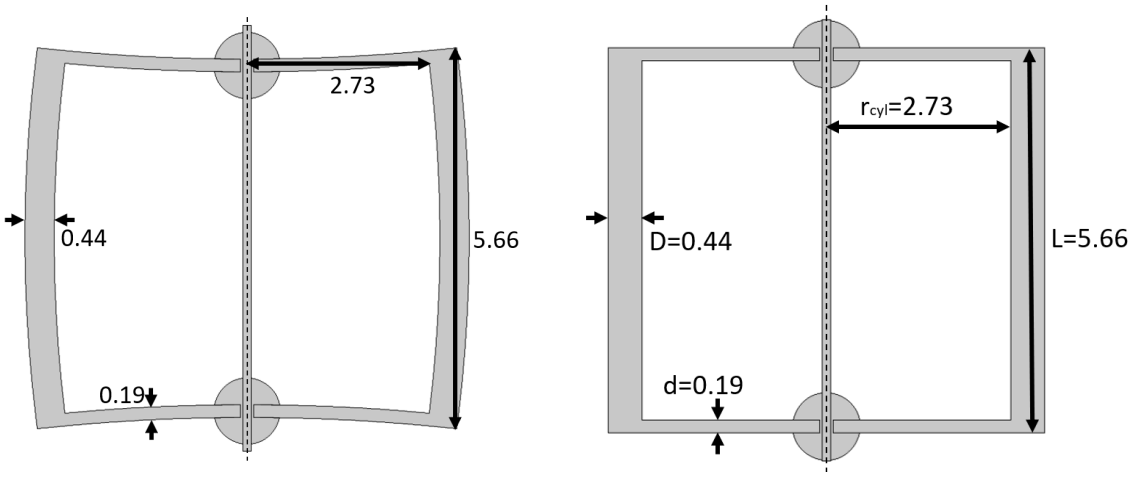

Figure 4-1: Left: the optimized design, 40NM, with dimensions [mm]. The radius of the circle which is used to draw the curvature of the diaphragm is 29.59 mm. The radius of the circle used to draw the curvatures of the cylinder is 21.67 mm. Right: the same design but without curvatures [mm]. The circles on the diaphragms depict the glue that attaches the fiber to the diaphragms.

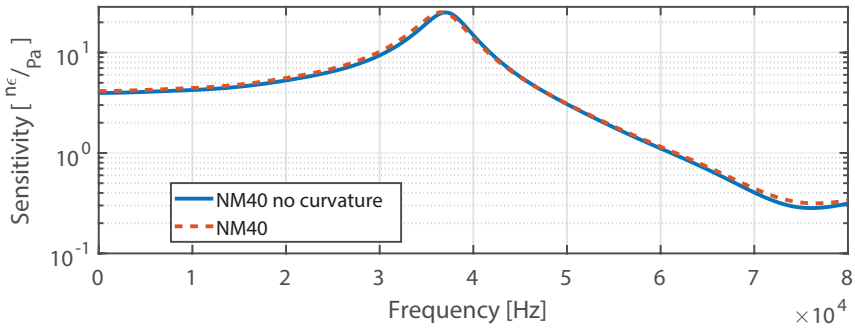

Figure 4-2: The FRF of the optimized design '40NM' with and without curvatures. As seen the difference is small.

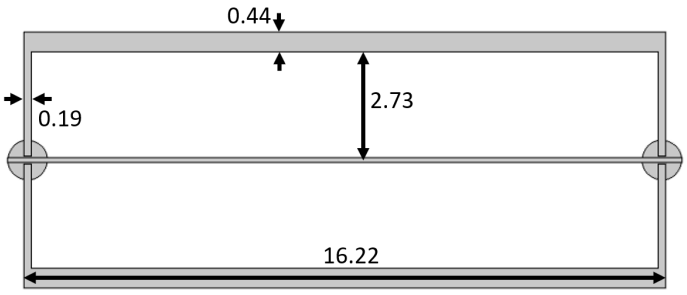

Figure 4-3: The design of a longer sensor with dimensions [mm].

4-2 Manufacturing

4-2-1 Manufacturing method

There are various methods to manufacture the sensor. Four different configurations of components to construct the transducer are shown in Figure 4-4. In advance it could already be expected that assembling and gluing the fiber would be the most problematic operation and therefore configuration 3 appeared the easiest to manufacture. The disadvantage of this configuration, however, is that there is a risk that the bonding is too close to the diaphragm and thus influences the behavior of the hydrophone. Configuration 2 and 4 also have this risk, especially concept 4 as the bonding is throughout the whole diaphragm. The advantage of concept 4 is that attaching the fiber is easier. Configuration 1, in which the two halves are first glued together and the fiber is inserted afterwards, is the only configuration without the risk of a large change in behavior of the hydrophone, but has the disadvantage that fixing the wire is most difficult to achieve. There are several ways to connect the components together and thus form the transducer. Two obvious options are gluing and welding. Welding is preferred as this causes a stiffer bond, gluing however can be done in-house.

The FRFs of configurations 1 and 3 were calculated in a model that includes the glue, these are depicted in Figure 4-5. The FRF of configuration 1 is very similar to that of the design without glue. Finally the transducer was manufactured as in configuration 1 and the components were assembled using glue.

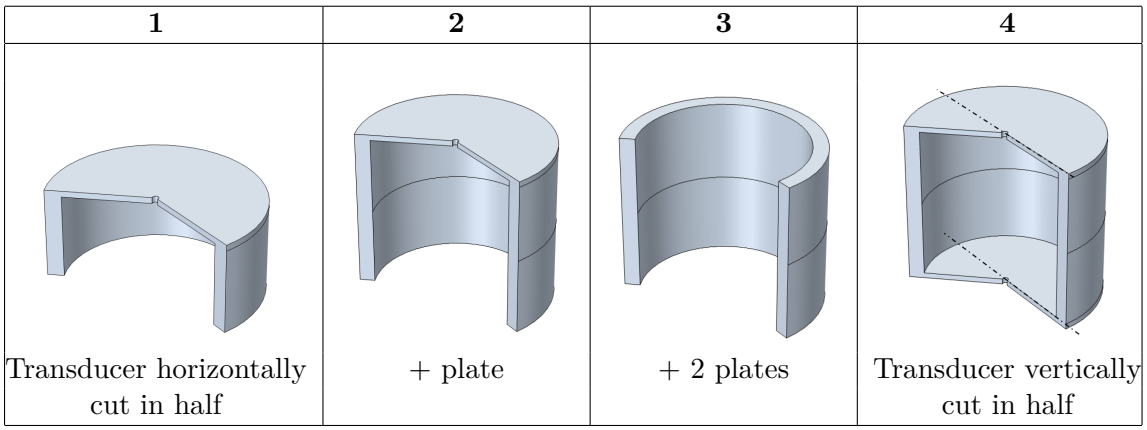

Figure 4-4: Four configurations of which components to manufacture to assemble the transducer.

4-2-2 Tolerances and final design

The tolerances were based on calculations of the static performance and the structural eigenfrequency. The maximum allowed error (within tolerances) caused by manufacturing was 5% for the static performance, and 3% for the structural natural frequency. By changing the dimensions in the 2D axisymmetric structural model, which did not include an acoustic (water) domain, and doing an eigenfrequency and static study, the tolerances were found. Table 4-1 lists the maximum allowed differences of the dimensions, to reach these maximum errors. To reduce the risk of loss of stiffness between the fiber and the diaphragm, the tolerance and

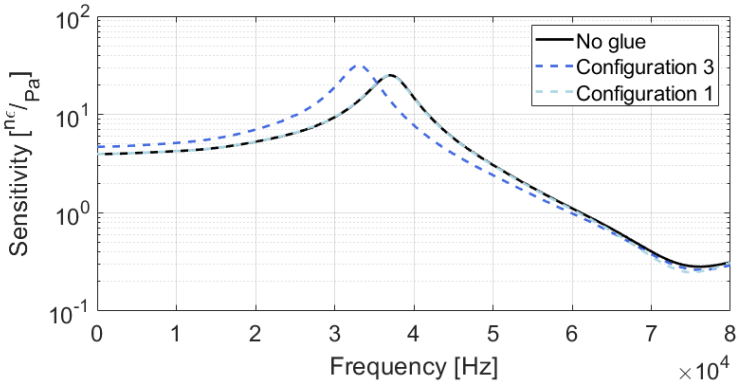

Figure 4-5: The FRF of the sensor without any glue and the FRF of configuration 1 and 3. The FRF of configuration 1 is almost the same as that of the sensor without glue.

dimensions for the hole in the center of the diaphragm were kept as small as possible. Based on the calculations of the tolerances it was decided to make the outer cylinder a bit thicker, this makes the manufacturing somewhat easier and gives the glue more area to bond the two halves to each other. The final design and the tolerances for the manufacturing are illustrated in Figure 4-6.

A sensor, which is three times as long, was also manufactured. The only difference between the longer sensor and the normal optimized sensor, which has the dimensions as in Figure 4-6, is that the height of the components is 7.715 mm and not 2.825 mm.

Table 4-1: The maximum allowed differences of the dimensions. The maximum error caused by the difference was max. 3 % for the structural eigenfrequency and max. 5 % for the static strain sensitivity.

	Normal value [mm]	Max. diff. for performance [mm]	Max. diff. for eigenfrequency [mm]
r_{cyl}	2.73	-0.055	+0.06
D	0.44	+6.56	-0.16
d	0.19	+0.01	-0.015
L	5.66	+0.65	+0.85

4-2-3 Manufacturing the sensor

One practical constraint during manufacturing was that not all types of fiber with a fiber laser were in stock. For this design a 125 μm thick fiber was needed with a fiber laser of 5 mm length engraved. While currently only fiber lasers of 2 cm length are commercially available, shorter lengths are expected to be possible in the future.
Thus the prototypes were manufactured with 125 μm thick fibers with FBGs of 5 mm length engraved in stead of fiber lasers. This does not complicate the experiments as the acoustic waves that were emitted during the experiments have a much larger amplitude than the minimum amplitude that can be sensed by the sensor with the FBG. Hence, a sensor with a FBG is still suited to characterize the dynamic behavior of the transducer.

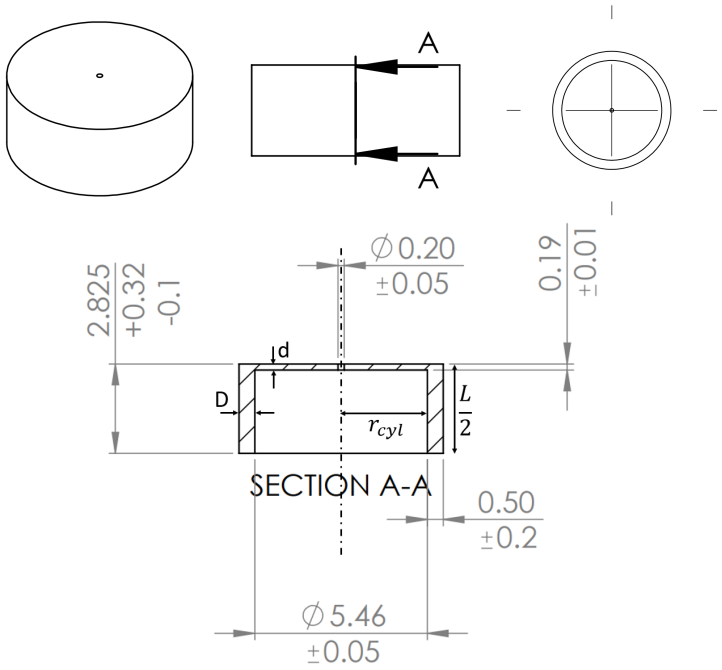

Figure 4-6: The final design of the sensor with tolerances [mm].

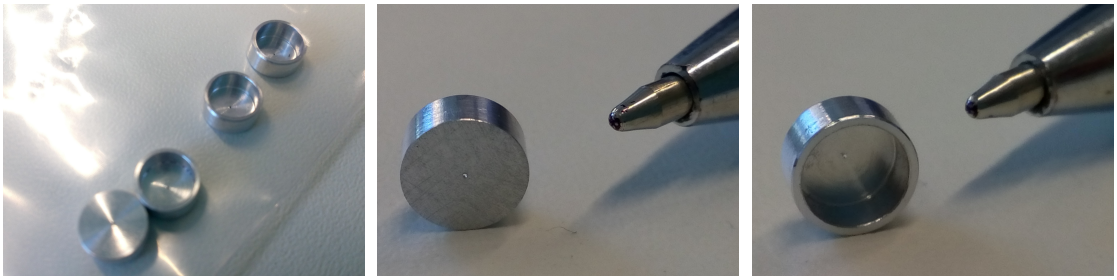

Figure 4-7: The components of the transducer.

During the manufacturing process the aluminum parts of the transducer were first machined. The components as shown in Figure 4-7. No measurements were done on the components to check the tolerances before assembly.
The next step was to find the location of the FBG, which is invisible, on the fiber. By slightly pulling the fiber with tweezers and looking whether there is a signal, it could be determined where the FBG was located on the fiber. The FBG is 5 mm long and while it is not possible to determine perfectly where the FBG is located on the fiber, the error is estimated to be less than 1 mm. As the FBG is 5 mm and the inside of the sensor is 5.270 mm it is of importance to correctly align the FBG and the transducer during the assembly process.
When the FBG and the sensor are not well aligned, part of the FBG will be outside of the sensor or it will be fixed in the glue, so that strain is only partially induced on the FBG when the diaphragms deform. However, also in this case the rest of the FBG will still function and give a correct signal. Only when a large part of the FBG does not experience strain the sensor is less sensitive.

Subsequently the two halves of the transducer were glued together. After the gluing of the two

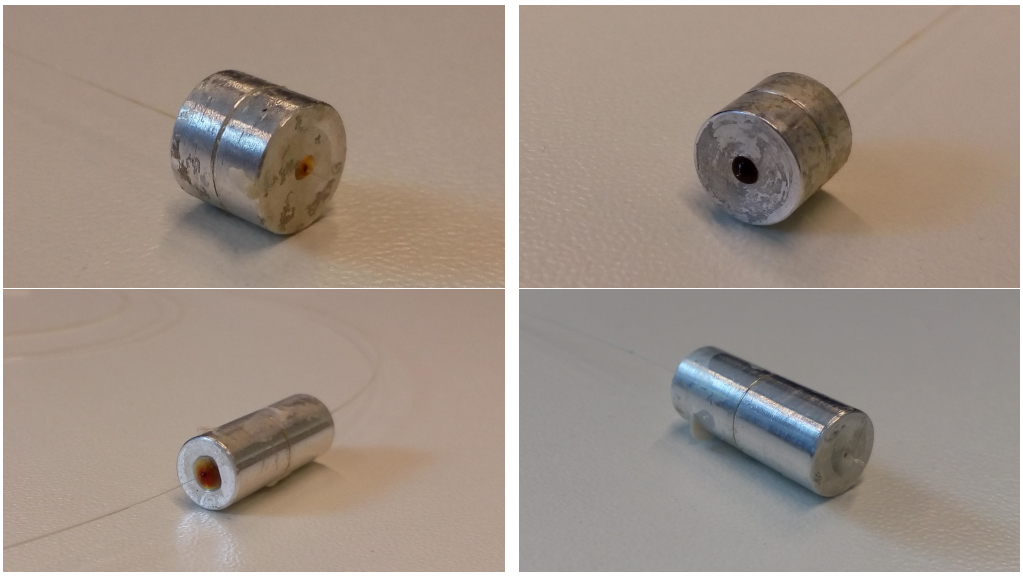

Figure 4-8: The manufactured fiber optic hydrophones. Top; left: S1, right: S2. Bottom; left: L3, right: L4.

halves, the fiber was laced through the tiny holes that are in the middle of the diaphragms. The fiber was glued to the diaphragm with a prestrain provided by hanging a mass of 100 grams off its lower end. This turned out to be quite unpractical as guiding the fiber through the second hole can be time consuming and two fibers also broke while hanging the mass for the prestrain on the fiber and during the hardening of the glue.

Figure 4-8 shows the two short and two long hydrophones, which were manufactured. The hydrophones were named: Short 1 (S1), Short 2 (S2), Long 3 (L3) and Long 4 (L4). The pictures were taken after the testing, this explains the stains and residues of the glue on the aluminum and the fact that some sensors miss parts of the fiber because the fibers broke during the manufacturing process or during experiments.

4-3 Frequency response of the final design

With the knowledge of all dimensions and the knowledge gained about the manufacturing of the hydrophone, detailed FEM models were made to calculate the FRFs of the hydrophones. In the models there were two possible locations of the acoustic source towards the hydrophone. When the source is below the FOH, the waves travel in a vertical direction. When the source is to the right of the FOH, the waves travel in the horizontal direction, this is depicted in Figure 4-9.

Figure 4-10 shows that when the frequency of the pressure waves becomes higher and thus the wavelengths become shorter, the ratio between the wavelength and the length of the sensor changes. When the wave is traveling in the vertical direction, as in the figure, this has an effect on the way the hydrophone is loaded. Especially in the model with the longer sensor - in which the sensor is 3 times longer - this effect plays a significant role. As seen in the right

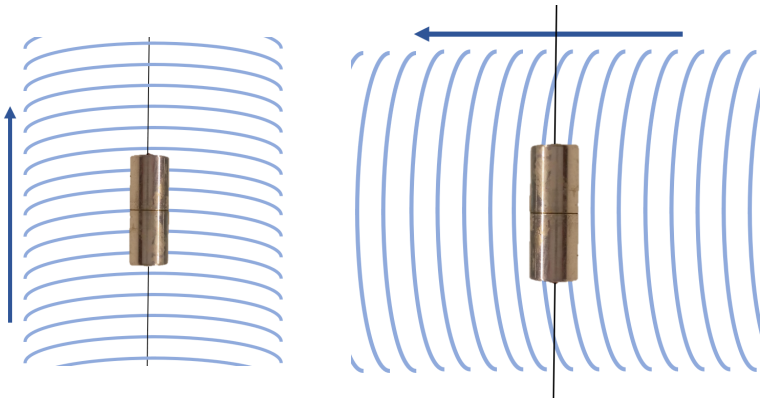

Figure 4-9: Left: when the source is to the right of the FOH, the waves travel in the horizontal direction. Right: when the source is below the FOH, the waves travel in a vertical direction.

figure, the length of the longer sensor is larger than one wavelength at higher frequencies.

The effect described above and the effect of directionality, i.e. to see if a wave traveling in a different direction influences the FRF, had to be further investigated. Figure 4-11 presents the FRFs with the acoustic waves traveling in different directions. In a 2D axisymmetric model it is not possible to simulate acoustic waves which travel in the horizontal direction. Hence, the load in this case was applied in another manner, which was to apply a pressure boundary load of 1 Pascal directly on the transducer. Also a FRF was calculated with a sine shaped pressure boundary load (with wavelength the same as that of an acoustic wave in water at that frequency) to compensate for the wavelength of the acoustic waves. Details on the FEM models are presented in Appendix D.

For frequencies higher than the first eigenfrequency, the shorter sensor, S1, shows a large difference between the FRFs for waves traveling in different directions. For lower frequencies, the difference is small. The effect of directionality is therefore not so big in the frequency range of interest, which is below the first eigenfrequency. The longer sensor shows a large difference in the whole frequency range, thus the longer hydrophones have a large difference in the FRF due to directionality.

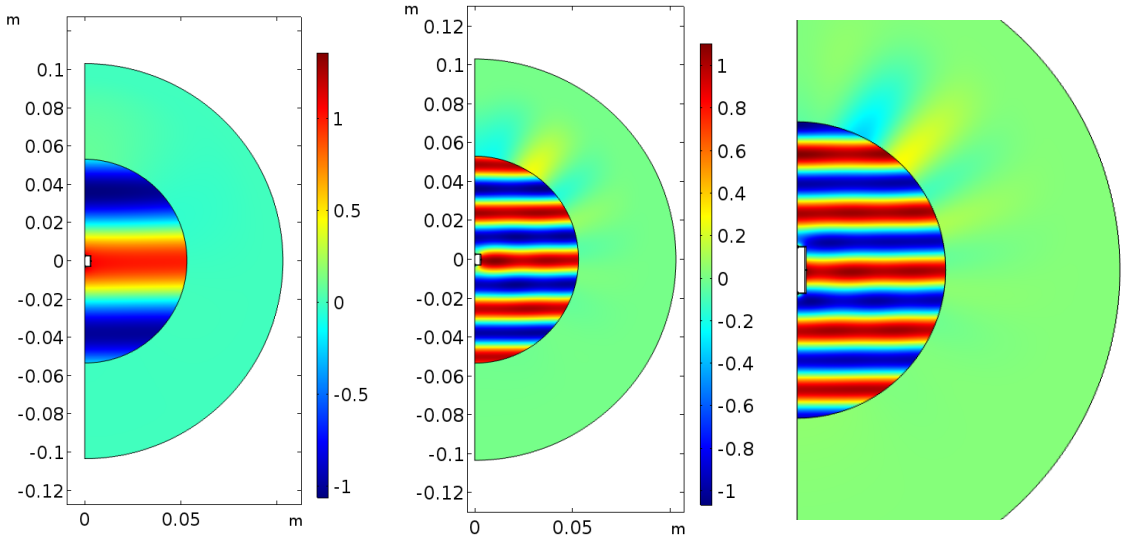

Figure 4-10: The acoustic wave is depicted versus the length of the FOHs. The colorbar depicts the acoustic pressure [Pa]. Left: S1 with an acoustic wave at 20 kHz. Middle: S1 with an acoustic wave at 60 kHz. Right: L3 with an acoustic wave at 70 kHz. L3 is so long that the top and bottom diaphragm are loaded by two different valleys.

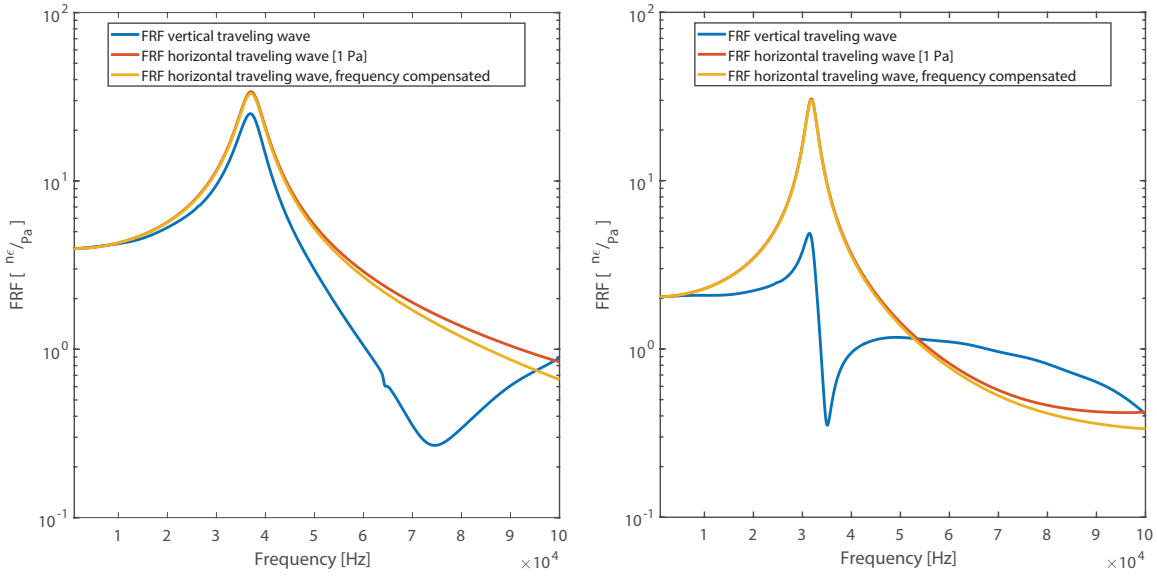

Figure 4-11: The FRF of the two designs with varying direction of the acoustic wave. Left: the FRF of S1. Right: the FRF of L3. For the longer sensor there is a clear difference between the FRF for a acoustic wave traveling in the vertical or horizontal direction.

4-4 Requirements check

In Section 1-3 the design requirement for the fiber optic hydrophone for UHE neutrino detection were set. In this section it is verified if the design meets those requirements.

Sensitivity

The sensitivity requirement demands that the hydrophone has to be able to measure the ambient noise in the sea at Sea State 0 (SS0). The sea state is a variable that describes the conditions of the ocean depending on the wind speed. When there is more wind (a higher sea state level) the sea is noisier and the ambient noise is thus higher. SS0 is when the water surface is very calm and the water looks glassy. SS1 is when the water surface is still calm, but there are small ripples, and SS4 is when there are average conditions. When the hydrophone can measure as low as the ambient noise in the sea, the noise in the sea is the limiting factor on the minimum amplitude of the signal caused by a neutrino interaction that can be detected. Otherwise the sensitivity of the hydrophone is the limiting factor.

In Figure 4-12 the FRF of S1 and the sensitivity requirements for different OPD lengths at SS0 and SS1 are plotted. The figure also depicts the sensitivities required to detect an acoustic wave, originating from the interaction of a 1 EeV neutrino with water molecules, at 1 km from the interaction. 1 EeV is the lowest energy of the ultra-high energy neutrinos that will be detected by the acoustic telescope in which the hydrophones will be implemented.

The sensitivity of the hydrophone is certainly significantly higher than the required sensitivity to measure the acoustic waves from UHE neutrino interactions. With an OPD of 10 or 20 m in the interferometer the hydrophone is capable of measuring the ambient noise of the ocean at SS1 for frequencies ranging from zero to just above the eigenfrequency. The ambient noise at SS0 can only be measured below 10 kHz and around the eigenfrequency. A larger number of hydrophones are needed to cover the whole detection volume of the telescope, when the noise at the location is lower than what the hydrophone can measure.
Important to keep in mind is that the noise at the location of the telescope is not known, this could be higher than the theoretical ambient noise at SS0.
Hence, although the sensitivity requirement to measure SS0 is only partially met, the hydrophone can still be used for UHE neutrino detection. A longer OPD length is possible, but investigation of that option did not fit within the framework of the research reported in this thesis.

Frequency range

The best signal to noise ratio of the signal from the neutrino interaction and the ambient noise is between 10 and 50 kHz. It was decided earlier that the frequency range of the hydrophone should be between 1 and 50 kHz. There was a trade-off between sensitivity and frequency range, hence a small concession was made on the frequency range.
The designed hydrophone has its first eigenfrequency at 37 kHz and after the peak at the eigenfrequency, its sensitivity is very low. The highest frequencies between 40 and 50 kHz fall outside of the measurable frequency range of the designed hydrophone.

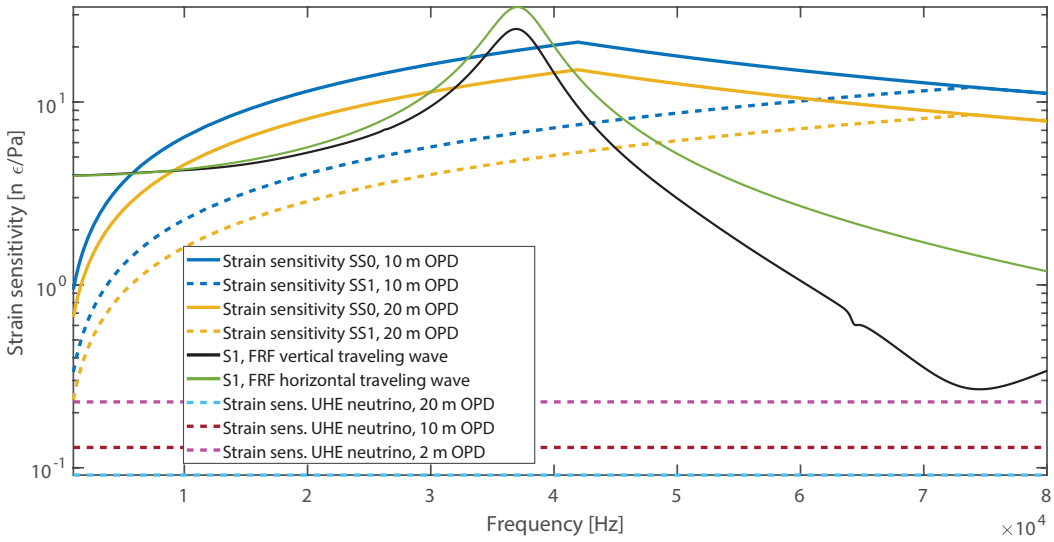

Figure 4-12: The FRF of S1, the sensitivity requirements and the sensitivity required to detect an acoustic wave from an UHE neutrino.

Dimensions

The hydrophone fits within the maximum dimensions of a quarter wavelength of the highest frequency in its frequency range. This requirement was created to ensure that the behavior of the hydrophone is the same for incoming acoustic waves from all directions. Within its functioning frequency range, below the eigenfrequency, the hydrophone shows little difference in FRF caused by directionality. The shortest fiber laser has a length of 5 mm, the designed hydrophone can house this fiber.

Static pressure

Although the design of a pressure compensation mechanism as such was not included in the research described in this thesis, some ideas were collected about how a pressure compensation mechanism could be involved in the design. However, the realization of such a mechanism remains a challenge for future research.
Expectations are that the hydrophone should be able to work when it would be pressure-compensated. The air inside a pressure-compensated hydrophone has the same absolute pressure as the water outside the sensor. The air has an absolute pressure of 1 atm when the hydrophone is above the water surface, thus at 3 km depth the air has an absolute pressure of 300 bar added to the 1 atm. The effect of the higher absolute air pressure on the dynamic behavior of the hydrophone was investigated. A FEM model, including various absolute pressures, was made and the results are shown in Figure 4-13. The volume inside the transducer is filled with air, which had an absolute pressure of 1 atm, 1 atm added with the pressure at 2 m water depth (20 kPa) or 1 atm added with the pressure at 3 km water depth (300 bar).
As seen the FRF shows no difference, except a small peak at 65 kHz, for the lower absolute pressures. With the absolute pressure simulating an operating depth of 3 km, there is a slight difference. The eigenfrequency is lower and the sensitivity is also slightly lower. The cause

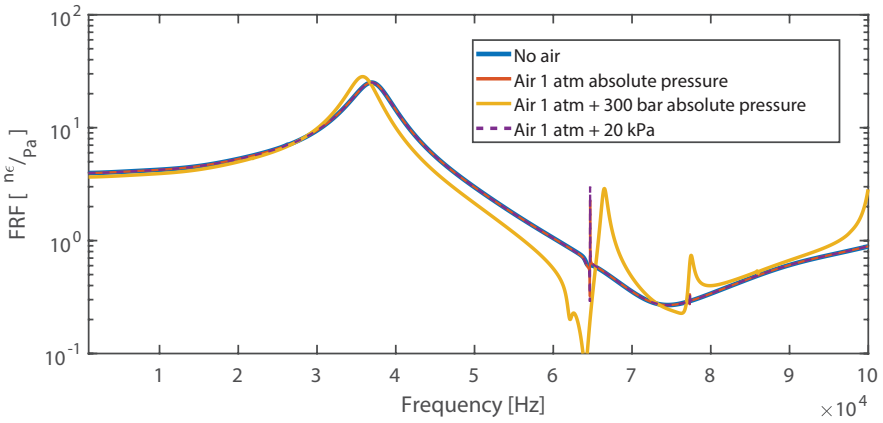

Figure 4-13: The FRF of S1 without any air in the FEM model and the FRF of S1 including air. The models including air have an absolute pressure of 1 atm, 1 atm added with the pressure at 2 m water depth (20 kPa) and 1 atm added with the pressure at 3 km water depth (300 bar).

of this probably lies in a noticeable added mass effect caused by the air. At higher pressures the density of air is higher and so its effect.

Costs and mass manufacturing

The components for the hydrophone were easy to manufacture. The assembly was, however, rather difficult because the fiber had to be laced through the small holes in the diaphragm and is vulnerable to breakage during the application of the prestress or during hardening of the glue.
An estimation of the costs for mass manufacturing could not be made, more research and engineering is needed to make a good estimate.

Chapter 5

Experiments

5-1 Test set-up

The four manufactured fiber optic hydrophones (FOHs), S1, S2, L3 and L4 were characterized and the results are presented in this chapter. The used experimental setup is depicted in Figure 5-1: left shows the measurement set-up needed to measure the wavelength shift of the reflected peak caused by the strain change in the FBG. An asymmetric light source (ASE) sends out a broad spectrum of light into the fiber. The interferometer is used to convert the wavelength shift to phase shift. This phase shift is converted to a change in output power by the optical-electronical unit (OE). The OE is read out by the data-acquisition system consisting of a NI PXI-1033 and a pc to both record and processes the data. The measured voltage can then be translated again to the original wavelength shift and thus the strain.
The set-up to measure the FL is shown on the right in Figure 5-1. The set-up is almost the same, the only difference is the light source, a pump laser that emits a smaller bandwidth of light than the ASE.

For the experiments the FOH was placed in an anechoic water basin of 10 x 8 x 8 m^3 with an acoustical source of type ITC-1042. The source operates within a frequency range of 0.01 - 100 kHz. Another crucial part of the experiments is the reference hydrophone, a piezoelectric hydrophone of type BK8103. The total test set-up is illustrated on the left in Figure 5-2, the signal from the reference hydrophone was amplified before acquiring the data. As seen on the right side of the figure the hydrophones were attached to a metal wire, which in turn was attached to a marked rope (with weight at the end), making it possible to lower the sensor to specific depths. The FOH was attached to the outer-side of the sensor by glue. The glue should not affect the dynamics of the sensor as the outer-side of the FOH is relatively thick. The reference hydrophone was attached using tape.

5-1-1 Calibration reference hydrophone system

The output of the reference hydrophone measurement system is used in the data analysis as input signal. It is therefore very important that the reference hydrophone system (which

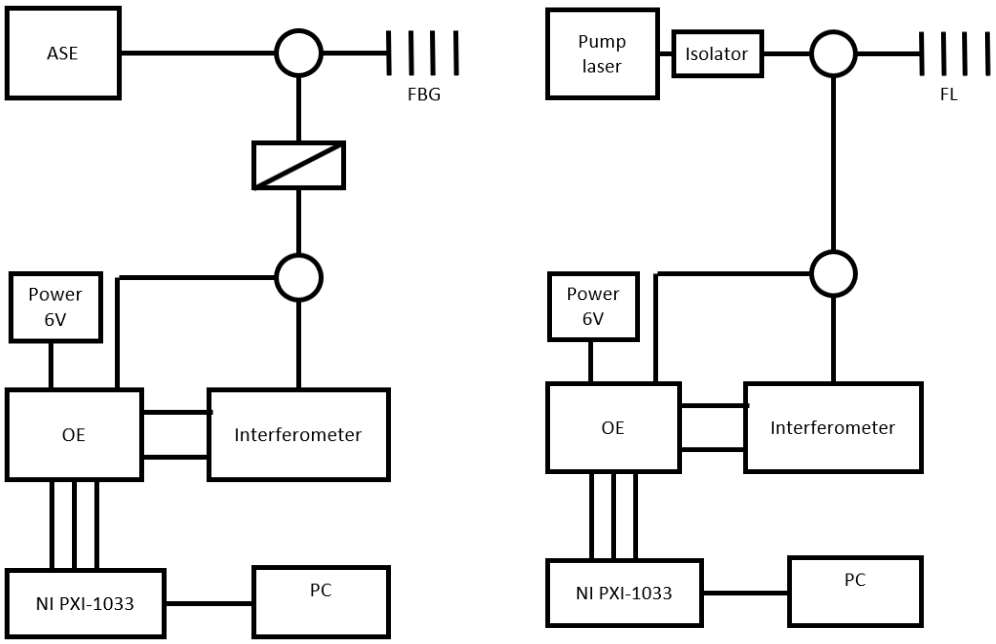

Figure 5-1: Left: measurement set-up for a FBG. Right: measurement set-up for a FL.

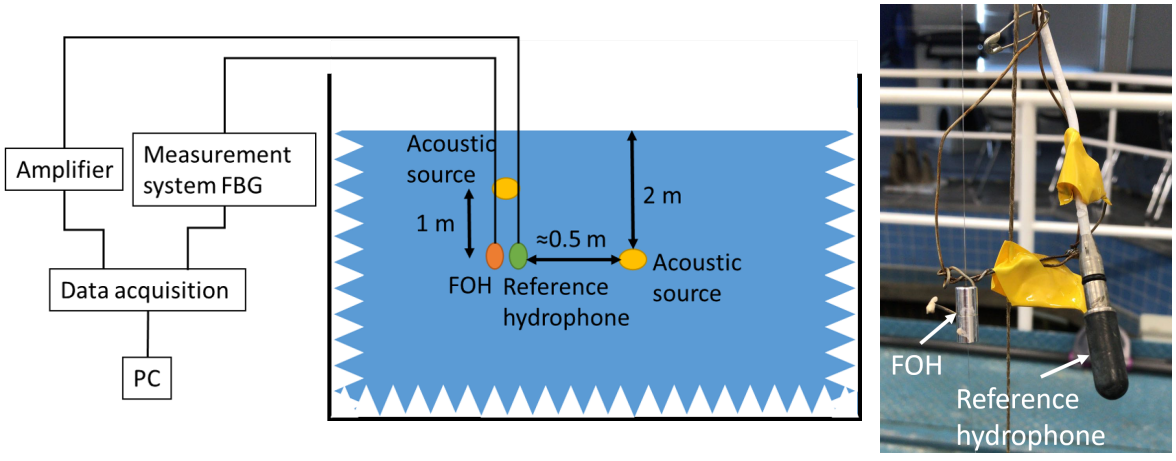

Figure 5-2: Left: the test set-up of the experiments. Right: the FOH an reference hydrophone are glued to a metal wire construction.

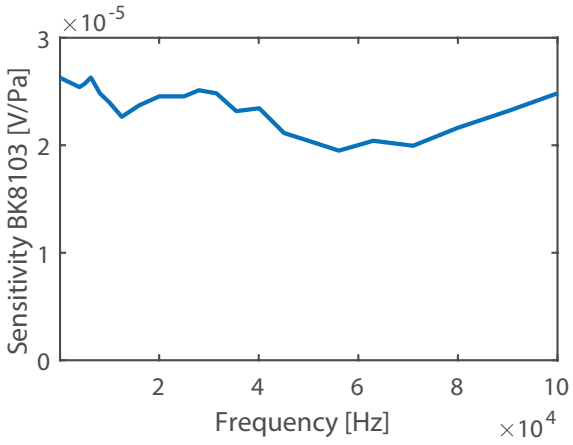

Figure 5-3: The sensitivity of the BK8103. The sensitivity is not completely flat, this is taken into account during calculations.

includes the amplifier and cables) is correctly calibrated and that losses are taken into account and compensated for. The sensitivity of the reference hydrophone is checked frequently and is described in it's specifications document. The pressure sensitivity of the reference hydrophone is depicted in Figure 5-3. The sensitivity is not completely flat, this is taken into account during calculations.

In addition, measurements were executed using a pistophone, the BK4223, to measure the signal loss caused by cables, connectors and amplifiers. The BK4223 is a device which produces a pressure wave at 250 Hz with a specific amplitude. The measurements with the pistophone indicated a signal loss of 8.6 dB. The derived signal loss was not taken into account during calculations in the following sections, due to the following reasons:

- 8.6 dB loss is a large loss for a system only including the reference hydrophone, an amplifier and 20 m of cable.
- Two different reference hydrophones and two different amplifiers were tested with longer and shorter cables, they showed the same losses. Hence, the loss is not caused by cable length, a flaw in the sensitivity specifications of the hydrophone or a flaw in the amplifier. The only device that was not interchanged and of which the behavior thus could not be verified, is the pistophone.
- The experimentally determined transfer functions correlate very well with the FRFs from the FEM models. Furthermore, additional measurements were done to determine the static sensitivity of the FOH. This static sensitivity is the same as the sensitivity of the dynamic measurements when interpolating the transfer function to "0 Hz".
  When compensating for the signal loss of 8.6 dB, the experimentally determined transfer functions as discussed in the next coming sections, lose a factor 2.7 in sensitivity. Hence in that case they would not correspond anymore with the FEM models and the static measurements.

The measuring uncertainty of the reference hydrophone between 4 kHz and 200 kHz is 1 dB. The specifications show that the change in sensitivity for temperature and static pressure difference (at 2 m depth) are negligible.

5-2 Results

Several different types of measurement were conducted:

- Static pressure measurements by lowering the hydrophone in the basin.
- Frequency sweeps from 1 to 80 kHz in one sweep and in smaller frequency ranges, with the source above or next to the FOH.
- Transient pulses at different frequencies.
- Tones at different frequencies and amplitudes.

The static measurements revealed the sensitivity for static pressure. Transfer functions of the hydrophones were determined from the sweep and pulse measurements. The pulse measurements were also used to study the behavior of the sensor in time. A pulse has approximately the same shape as the pulse caused by neutrino interactions. With the tone measurements the sensitivity at one frequency was determined accurately and also the linearity of the hydrophones for different amplitudes of the pressure waves was investigated.

To prevent aliasing, the sampling frequency must be a least twice the frequency of the highest frequency component present in the continuous time signal following the Nyquist criterion. The sampling frequency that was used is 400 kHz and the highest frequency used in the measurements was 80kHz.
A common way to convert time measurements to the frequency domain is by using the Fast Fourier Transform (FFT). This is a very efficient algorithm to describe discrete time measurements as a series of cosines. When the length of the measurement is not precisely an exact multiple of the period of the signal, or if the signal is not perfectly periodic, leakage errors occur. Sometimes leakage can even mask components of smaller signals.
The begin- and end-points are discontinuous, these discontinuities are shown in the FFT as (high) frequency components that are not present in the original signal [43]. To make sure that there are no discontinuities between the begin and the end point a window (filter) was applied to the data. A window makes sure that the begin and end point are zero. In this way the leakage does not affect the complete frequency bandwidth and is confined to a smaller frequency range. This allows to determine the true amplitude of individual peaks and in the case of two closely spaced tones it is possible to separate them [44].

Different windows are used for the different types of measurements. Amplitude accuracy is very important for the data analysis of the tone measurements, hence, a flattop window was used with 1 s length. To analyze the sweep measurements a rectangular filter with a length of one sweep was used. During the data analysis of the pulse measurements it is important to align the window with the pulse. A Hanning window was used with the middle of the window located at the start of the pulse. The length of the Hanning window should be long enough to include the dynamics of the hydrophone caused by the pulse, and should be short enough to exclude the dynamics caused by reflections of the acoustic waves. In the horizontal plane the space between the source and the hydrophones was approximately 0.5 m and the first object to cause reflection was the surface of the water which was located 2 m higher. The first reflection, reflected via the water surface, has a traveling distance of 2.0156 m from the source to the hydrophones. The time needed for this wave to reach the hydrophones is 1.3

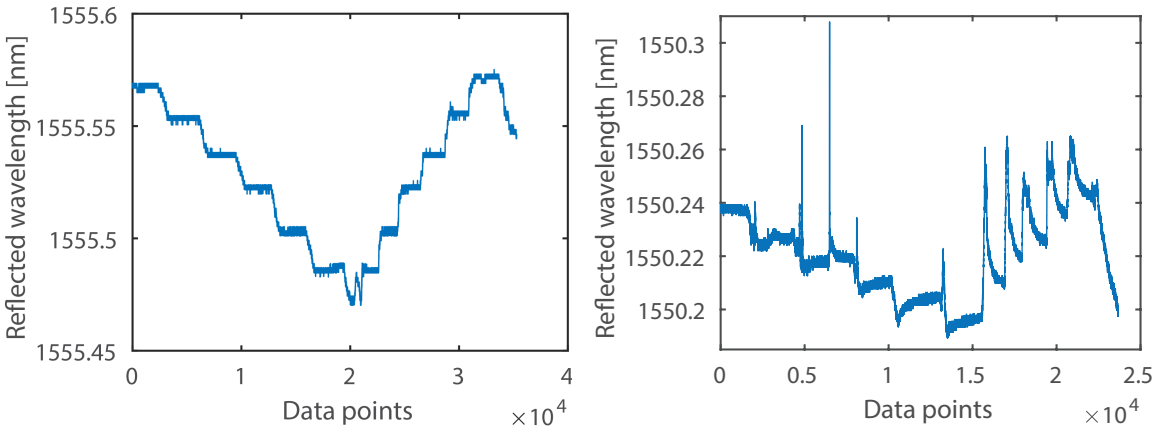

Figure 5-4: The reflected wavelength while lowering the FOHs to 5 m depth in steps of 1m. The steps of 1 m depth difference can clearly be seen. Left: L3. Right: L4.

ms, thus the length of half the window should be shorter than this. The length of the window is 2 ms.
There may be some error in the results if the reference sensor and the FOH were not placed at the same distance of the source. It is assumed that this difference was very small.

5-2-1 Static pressure measurements

The FOHs were lowered in the basin in steps of 1 m, the reflected optical wavelength was measured with a Micron optics device. This set-up does not require a reference hydrophone. Figure 5-4 shows the recorded data of hydrophone L3 and L4. The steps of 1 m depth difference are clearly visible. Results for S1 and S2 were found similar to that of L3. Only L4 shows odd behavior, with every step it takes some time to settle. It is not known what causes this behavior. Two possible causes may be that either the hydrophone has a small leakage or that the FBG is partially located outside the transducer. If the FBG is partially located outside the transducer when the transducer is moved, the fiber outside the transducer will bend and it will take some time for the fiber to move to its original position.

The optical wavelength shift between two successive depth levels was determined and converted into the strain in the fiber per Pascal pressure. The results are presented in Figure 5-5. The two thick black lines depict the static sensitivity as predicted using FEM. The static sensitivity is 3.95 $\frac{\mathrm{n}\epsilon}{\mathrm{Pa}}$ for the short hydrophones and 2.04 $\frac{\mathrm{n}\epsilon}{\mathrm{Pa}}$ for the long hydrophones. The sensors exhibits similar sensitivity on all depth levels when moving up and down between these levels. Some error can be explained by the way in which the test was conducted. The rope was held by hand and also manually lowered and an error of a few cm in depth could easily be made. An error in marking the distances on the rope can also easily be made. An error of 5 cm corresponds to an error of 5 %, which is 0.2 $\frac{\mathrm{n}\epsilon}{\mathrm{Pa}}$ using the predicted sensitivity. Also the lower sensitivity between 0 m and 1 m depth can be explained because that the sensor was at the surface of the water, and it was sometimes below and sometimes on the surface during measurements.
The average of the sensitivities is 3.82 $\frac{\mathrm{n}\epsilon}{\mathrm{Pa}}$ for S1, 2.82 $\frac{\mathrm{n}\epsilon}{\mathrm{Pa}}$ for S2, 1.35 $\frac{\mathrm{n}\epsilon}{\mathrm{Pa}}$ for L3 and 0.75 $\frac{\mathrm{n}\epsilon}{\mathrm{Pa}}$ for L4. It is concluded that S2, L3 and L4 are less sensitive than predicted. Reasons for this

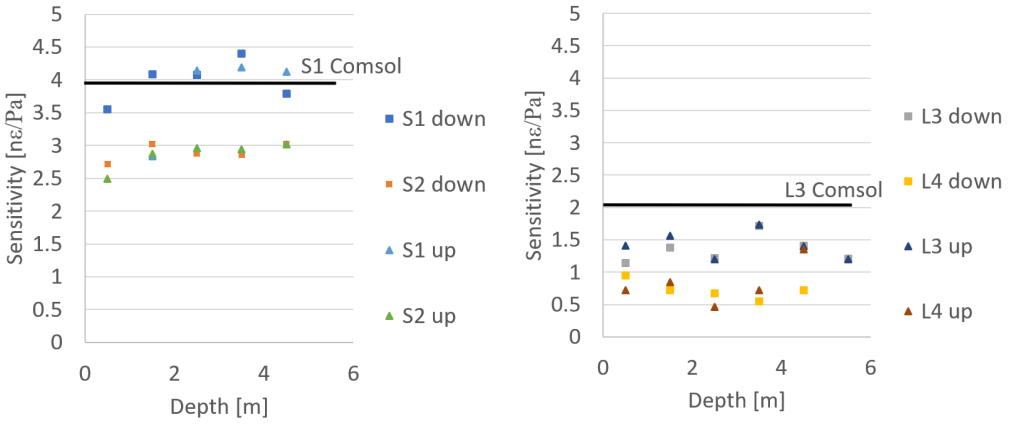

Figure 5-5: The static sensitivity of the FOHs while lowering them deeper in the water in steps of 1 m. The black line depicts the predicted sensitivity by the FEM models. Left: the normal hydrophones. Right: the longer hydrophones.

could be that the diaphragms are thicker or have a smaller radius or that the transducers are longer. Within the manufacturing tolerances the static sensitivity allowed is in the worst case 3.38 $\frac{\text{n}\epsilon}{\text{Pa}}$ for the short sensors and 1.73 $\frac{\text{n}\epsilon}{\text{Pa}}$ for the long sensors.
When the fiber is attached there will always be some glue on top of the diaphragm. In the FEM model a drop of glue of 1 mm was taken into account. The glue on the manufactured sensors can have a different Young's modulus than the glue in the model and the shape can be different anyway. Hence the differences between the experimental sensitivity and the calculated sensitivity may also have been caused by glue affecting the sensitivity or by a manufacturing error exceeding the manufacturing tolerances.

5-2-2 Transfer function

The transfer functions were determined using the measurements with the sweeps and the pulses. The sweeps were generated with a function generator and the frequency was increased at a fixed rate. Typically the sweeps spanned a frequency range of 10 kHz or more and the period was a few seconds.

The formulas to calculate the transfer function and the coherence function are:

$$\text{Transfer function} = \frac{P_{yx}}{P_{xx}}. \tag{5-1}$$

$$\text{Coherence function} = \frac{|P_{xy}|^2}{P_{xx}Pyy}. \tag{5-2}$$

In the equations, P_{xx} is the PSD of the input signal, which is the output of the reference hydrophone and P_{yy} is the PSD of the output signal, which is the output of the FOH. P_{xy} is the cross power spectral density of the two signals.
The coherence function is commonly used to examine the relation between the two signals and to estimate the causality between the two signals. When two signals are perfectly correlated the coherence is 1, when there is absolutely no correlation the coherence is 0. The coherence can thus be taken as an indicator of the quality of the transfer function. In the research

presented in this thesis the transfer functions of the sweeps are filtered with the values of the coherence function, in which a coherence higher than 0.7 is required.

In Figure 5-6 the transfer functions of the frequency sweep measurements are shown and compared with the FEM predicted FRFs. On the left side the measurements are shown when the source is above the hydrophones, on the right side the measurements when the source is located next to the hydrophones. The first row from above presents the transfer functions of the measurements with S1, the second those with S2, the third those with L3 and finally the bottom row represents the measurements done with L4. The various colors in this figure indicate the transfer functions of the separate measurements and the black line indicates the FRF from the FEM model.
In general the FEM predicted FRFs correlate very well with the experimentally determined transfer functions. When the measurements were conducted immediately after each other, without changing anything in the configuration, it is clearly seen that these measurements align very well together. But in a measurement that was done later, while in the meantime the sensor had been moved, a change in behavior is observed. This can clearly be seen in the top right figure, where there is a dip at the eigenfrequency. A clear explanation for this was not found, maybe a strange reflection (by the basin, watersurface or the hanging construction) precisely on only one of the reference hydrophone or FOH and not on the other could have caused this.

Pulse measurements at different frequencies (and different input voltage to the source) were also conducted. The input signal is an acoustic wave at a certain frequency, which stops after one wavelength. In Figure 5-7 the transfer functions of the pulse measurements are compared to those calculated from frequency sweeps for S1 and L3. The transfer functions of the pulse measurements verify those of the sweep measurements, they show the same behavior including the peaks and valleys.

The experimentally determined transfer functions of S1 and L4 correspond very well with the expected behavior as predicted in the FRF using FEM. The eigenfrequency is located at the expected frequency. The sensitivities are also the same, even at the resonance peak. The measurements and the FEM model of S1 have the same Q-factor, which is 0.13, hence the damping was included correctly in the models. One difference is that the transfer functions of S1 and L4 with the source horizontal to the hydrophones show unexpected behavior around 68 and 74 kHz. As the axi-symmetric FEM model can only include symmetric eigenmodes, this may indicate an asymmetric eigenmode.
For the other two sensors, S2 and L3, the shape of the experimentally determined transfer functions and the FRF by the FEM model have the same general shape. The location of the eigenfrequencies is though somewhat higher and also the sensitivity is lower. This suggests that the diaphragms were manufactured stiffer. The behavior of both S2 and L3 with the source horizontal to the hydrophones, show a dip (or multiple) at the eigenfrequency. This is seen in the measurements with the burst and the sweeps, thus it can not be caused by echos. A possible explanation could be that the diaphragms on the same hydrophone have a different stiffness, which causes dynamic behavior that was not taken into account.

At the end of Chapter 4 it was predicted that the longer sensors would behave differently for waves traveling horizontally or vertically in the direction of the sensors. The experimentally determined transfer functions confirm this behavior.
Furthermore, when estimating the static sensitivity by interpolating the transfer functions

towards 0 Hz, the results from the static measurements are confirmed. The transfer function and the static measurement results show the same static sensitivity for FOHs S1, S2 and L3. The static sensitivity for L4 is different and as the static measurement of L4 also showed some strange behavior, which is not well understood, it was concluded that the static measurements of L4 were probably executed wrongly.

The manufacturing tolerances can explain the differences between the measurements and the FEM model partially. A FRF with the largest changes in tolerance was calculated to see what the maximum change in behavior due to manufacturing tolerances could be. The diaphragm was made 0.01 mm thicker, the diameter 0.05 mm smaller and the length 0.64 mm longer. The FRFs of the FOHs with changed dimensions are plotted versus the transfer functions of the measurements, this is shown in Figure 5-8. The slightly higher eigenfrequency and lower sensitivity of the L4 hydrophone lies within the possible difference caused by mechanical tolerances. For S2 and L3 the tolerances can explain some of the difference, but not all. Similar to the static sensitivities, the glue on top of the diaphragm where the fiber is attached can have a different Young's modulus than the glue in the model and the shape can differ, causing a different behavior.

In Figure 5-9 the PSDs of sweep measurement with FOH S2 are shown. The left figure presents the PSD of the reference hydrophone and the figure on the right presents the PSD of S2. The amplitude of the pressure waves emitted by the source scales linearly with frequency, following the specifications of the source and verified by looking at the PSD of the reference hydrophone. At low frequencies the amplitude of the emitted pressure waves was so small that the measurements of the reference hydrophone, but also of the FOH show a large noise. This noise caused a coherence below 0.7 for frequencies below 10 kHz.

Echo

The transfer functions originating from the frequency sweeps show a substantial jitter. Looking in more detail at transfer functions of different measurements, which overlap in their frequency range, it is noticeable that this jitter does not behave randomly, but is rather constant. In Figure 5-10 transfer functions of different measurements of S2, conducted after each other without changing anything in the set-up, are depicted. The PSD of the FOH and the reference hydrophone are depicted in Figure 5-11. The jitter is present in both hydrophones, so it is not caused by the dynamics of the hydrophones.

A simulation was conducted of a frequency sweep with echos. An echo that is delayed by 1.3 ms, the minimum travel time for an echo reaching the hydrophones in this set-up, and that has 5% of the power of the original signal was added to the sweep. An extra echo that is delayed by 2 ms was added in a second simulation. The PSD of these signals without and with echos is shown in Figure 5-12. There is a jitter very similar to the jitter in the measurements. Hence, it is likely that the jitter in the measurements is caused by the echos in the basin. In further research it is recommended to experiment in a large lake or sea to avoid the echos that cause this large jitter in the transfer functions.

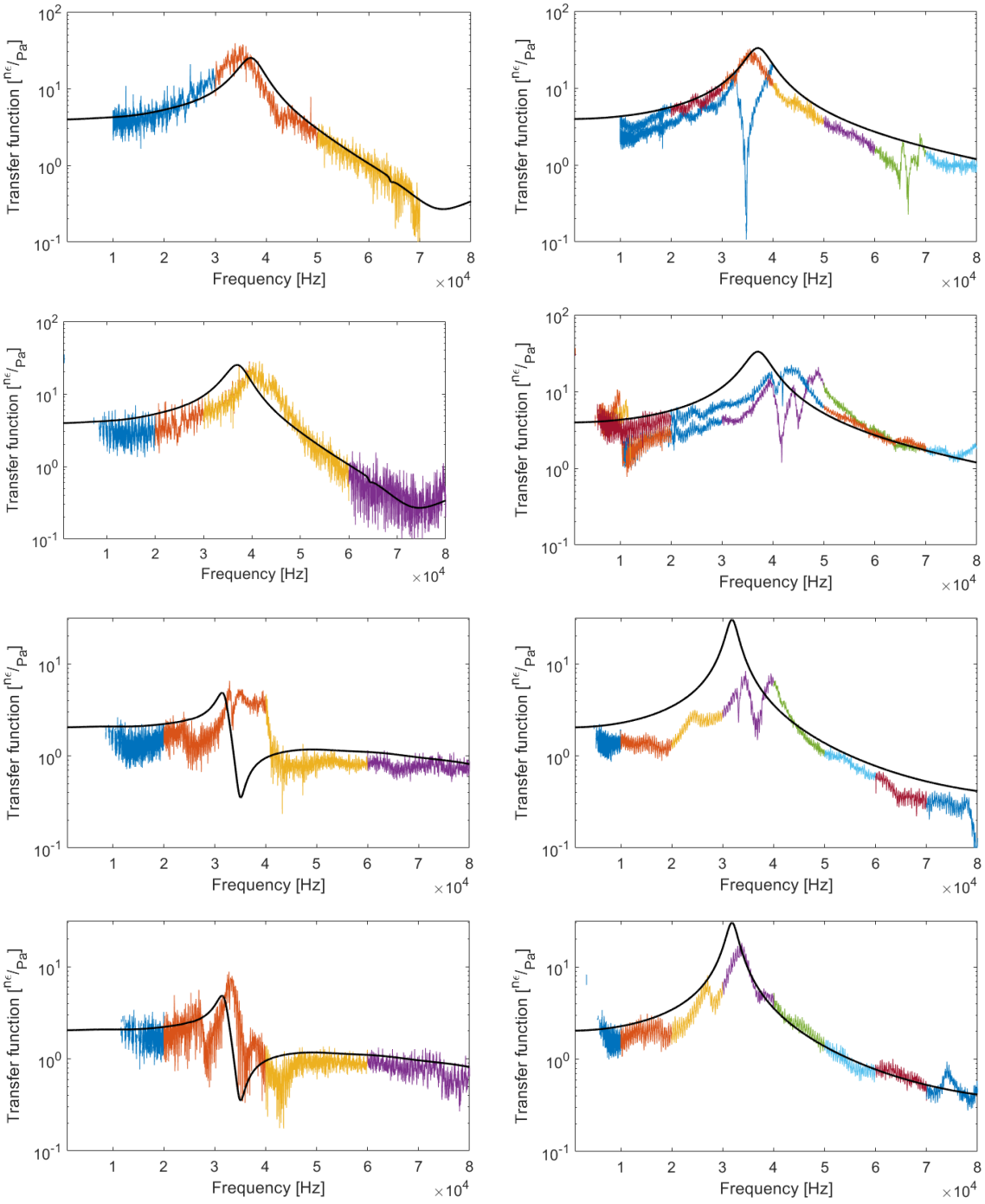

Figure 5-6: The transfer functions of the frequency sweep measurements. The colors indicate the transfer functions of the separate measurements and the black line depicts the FRF from the FEM results. The 1^{st} row shows the transfer functions of S1, the 2^{nd} row shows those of S2, the 3^{rd} row show those of L3 and the 4^{th} row shows those of L4. Left: the source is located above the hydrophones. Right: the source is located at the same height of, next to, the hydrophones.

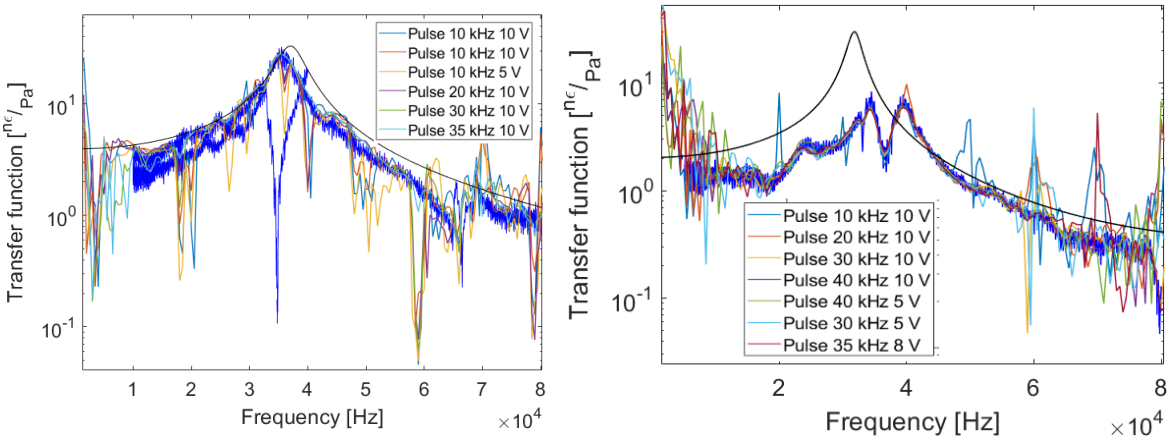

Figure 5-7: The colored lines that are included in the legenda depict the transfer functions of the pulse measurements, the blue lines depict the transfer functions of the frequency sweeps with the source horizontal to the hydrophones. The black line is the FRF from the FEM model. Left: S1. Right: L3.

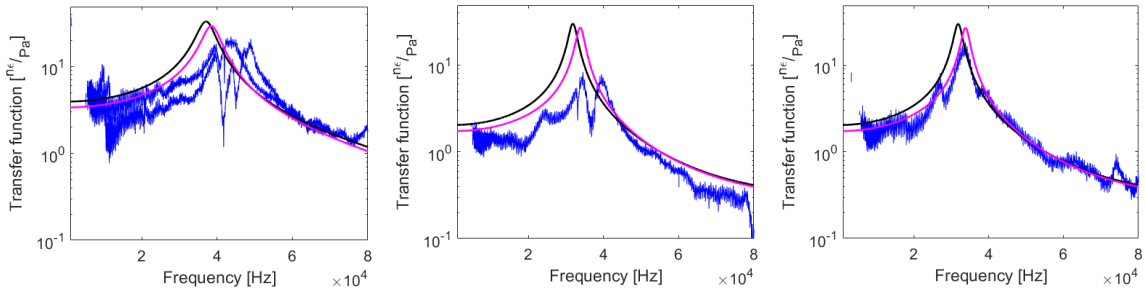

Figure 5-8: The magenta lines depict the FRFs of the FOHs with the maximum tolerance error, the black line depicts the normal FRF from the FEM results and the blue lines depict the transfer functions from the frequency sweeps. Left: S2. Middle: L3. Right: L4.

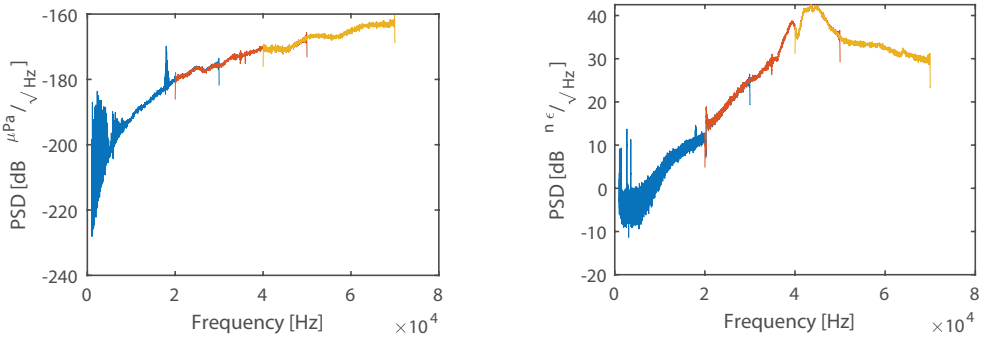

Figure 5-9: The PSD of sweep measurements done with FOH S2. The colors depict different meaurements. As seen the amplitude of the pressure waves is smaller at lower frequencies and the the signal to noise ratio is larger. Left: the PSD of the reference hydrophone. Right: the PSD of S2.

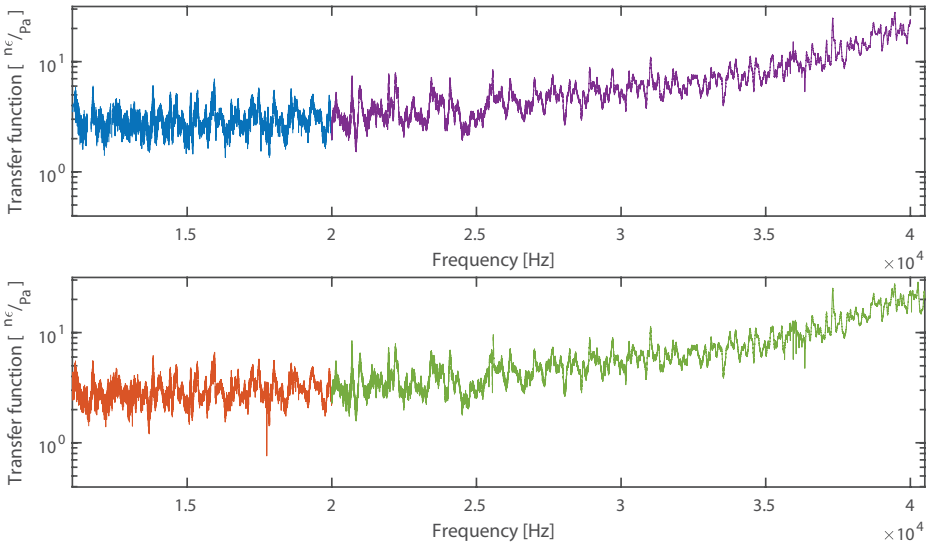

Figure 5-10: The jitter in the transfer functions of different measurements is almost identical for measurements with the same configuration. The colors indicate the transfer functions of different measurements with sensor S2.

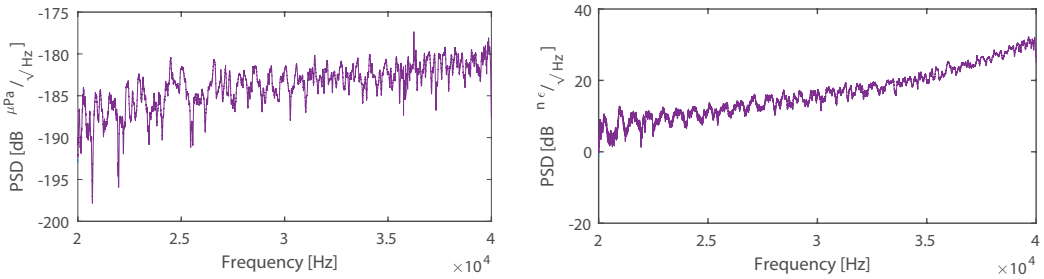

Figure 5-11: The PSD of the FOH and the reference hydrophone is depicted. The jitter exists in the PSD of the measurements of both the FOH and the reference hydrophone. Left: reference hydrophone. Right: the FOH.

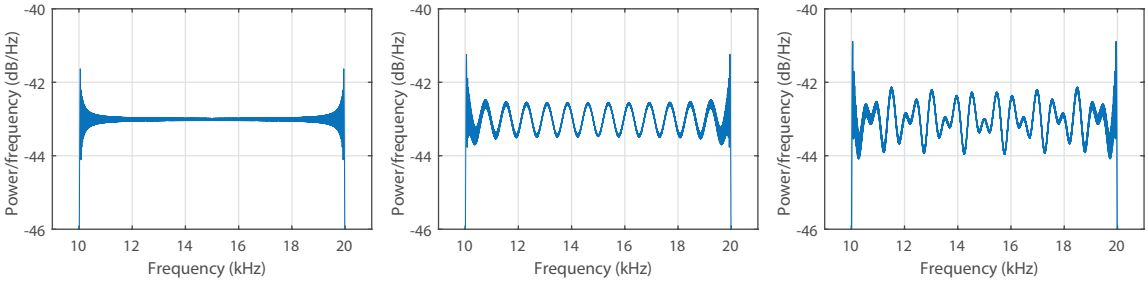

Figure 5-12: Left: PSD of a frequency sweep without echo. Middle: PSD of the same signal with an echo with 5% amplitude that is 1.3 ms delayed is added. Right: PSD same signal with another echo added with time delay of 2 ms.

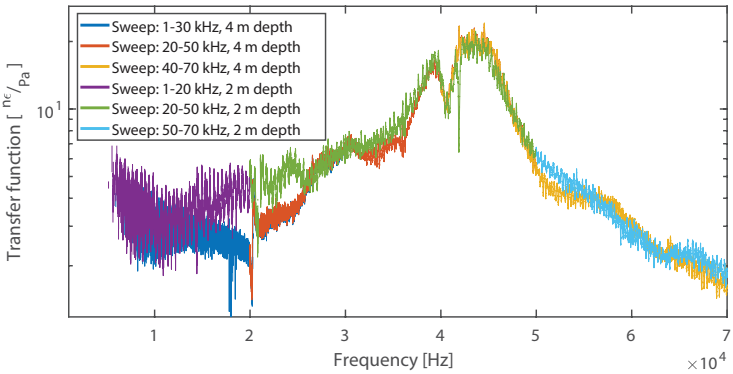

Figure 5-13: Transfer functions of the frequency sweeps of the FOH S2 conducted at 2 and 4 depth. There is no difference.

Depth dependency

To check if the dynamic behaviour of the hydrophones would change with a higher static pressure, the frequency sweep measurements with FOH S2 were conducted at 2 and 4 m depth. The transfer functions for these measurements are given in Figure 5-13. As seen there is no depth dependency. A FEM simulation including different static pressures, corresponding to 0, 2 and 4 m water depth, was conducted. This simulation also showed a negligible difference in behavior between static pressure differences in this range.

5-2-3 Tone measurements

To determine if the hydrophones behaves linearly, measurements were done with a constant tone at one frequency. The measurements were done with a varying input voltage of the acoustic source. The amplitude of the acoustic waves scales linearly with the input voltage. The PSD of the tone measurements at 30 kHz with different input voltages for the S1 is depicted on the left of Figure 5-14. The PSD amplitude scales linearly with the used input voltage. On the right of the figure the measured strains by the FOHs during the measurements, with tones at several frequencies, as a function of input voltage are shown. Note that the different slopes are due to the output of the source, which is not constant but increases with frequency (see Figure 5-9). At higher and lower frequencies all the four FOH's behave linearly. This means that the experimentally determined sensitivity is also valid for pressure waves with a low amplitude, such as the pressure wave from the neutrino interaction.

The transfer functions of the tone measurements complement the transfer functions derived from the sweeps and the pulse measurements. In Figure 5-15 and Table 5-1 the transfer functions of the sweep and pulse measurements are compared to the sensitivities from the tone measurements and the FRFs from the FEM mode. The jitter in the sweep measurements makes it difficult to find the exact sensitivity. Only the value of the pulse measurement that had the same frequency as the tone is listed in the table. Except for the 20 kHz tone measurements with the S1, the sensitivities from the tone measurements correspond very well with most sweep and pulse measurements. The amplitude of the transfer functions of the sweep and pulse measurements is thus quite trustworthy.

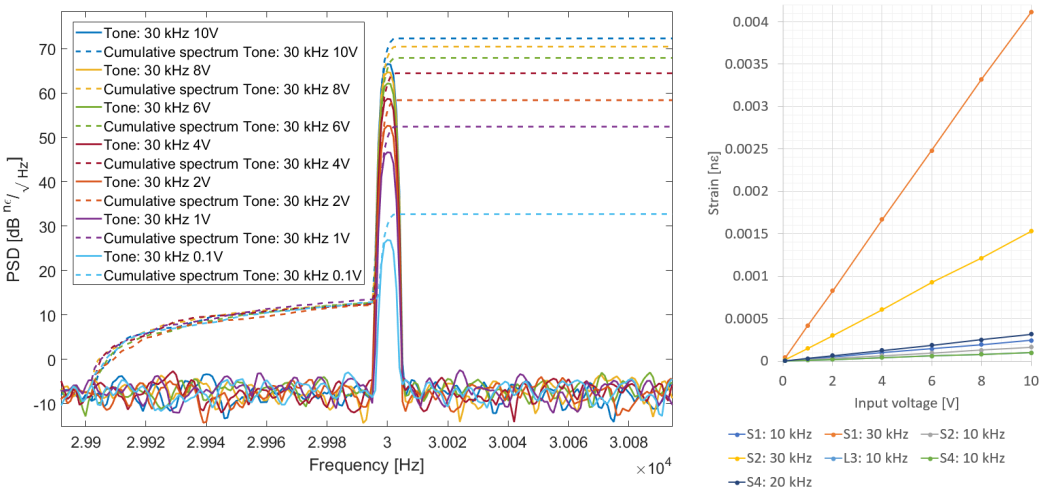

Figure 5-14: Left: the PSD of tone measurements at 10 kHz with several voltage as input. Right: the measured strain of the tone measurements, at several frequencies, as a function of input voltage for the four FOHs.

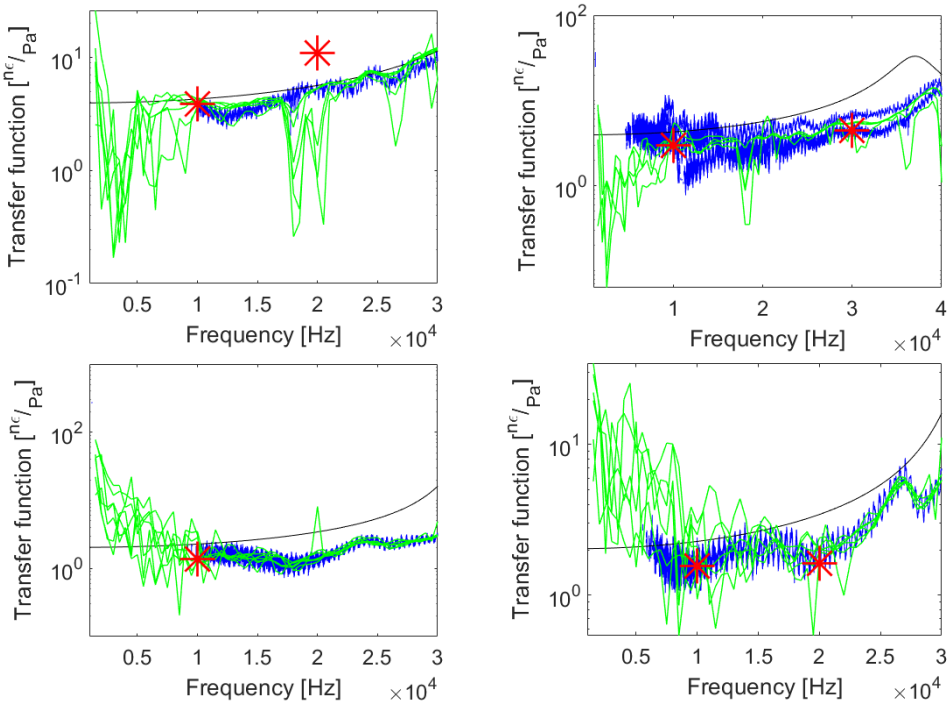

Figure 5-15: The sensitivities found with the tone measurements (red stars) are compared with the transfer functions from sweep (blue lines) and pulse measurements (green lines) and the FEM model (black line). Top; left: S1, right: S2. Bottom; left: L3, right: L4.

Table 5-1: Value of the dynamic sensitivity at certain frequencies, deduced from the transfer functions, which are derived from the various measurements.

Sensor	Freq. [kHz]	Tone	Sweep	Pulse	FEM model
S1	10	3.88	3.73/2.34	4.284	4.28
	20	11	5.51/3.51	5.28	5.66
S2	10	2.99	3.19/4.39/5.87	2.78	4.29
	30	4.46	7.24/4.53	5.52	11.36
L3	10	1.39	1.51	1.49	2.28
L4	10	1.56	1.61	1.82	2.28
	20	1.63	1.62	2.01	3.44

5-2-4 Pulse measurements

The pulses used during the pulse measurements had approximately the same shape as the pulses coming from neutrino interactions, which is a sine shaped pulse with a length of only one wavelength. Hence, it is very interesting to look at the behavior of the sensor for such signals. Although the used pressure amplitude during the measurements is higher than the amplitude from a real neutrino signal, the dynamic behavior is still realistic as the FOHs behave linearly.

The pulse measurements of the FOH S1 are shown for pulses at three different frequencies in Figure 5-16. The acoustic source sent out a higher amplitude at higher frequencies and the FOH has also a higher sensitivity at frequencies closer to the eigenfrequency. Hence, the response of the FOH at 30 kHz is much larger than at 10 kHz. At 10 kHz the amplitude was even so low that the response in the time domain is difficult to make clearly visible above the noise. The FOH has, in contrast to the reference hydrophone, a long reverberation after the pulse, especially for frequencies close to the eigenfrequency. By filtering the original signal can be retrieved.

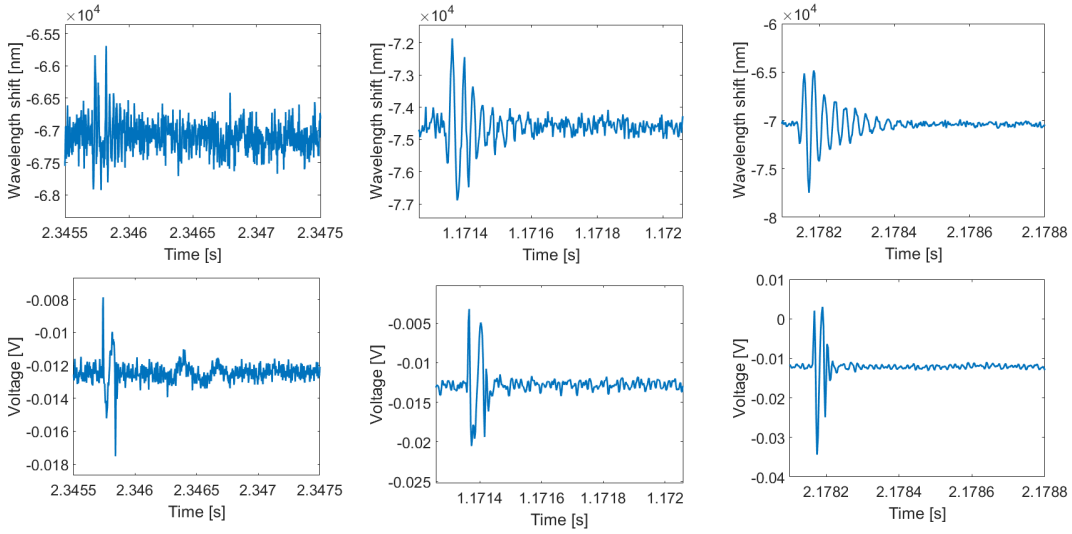

Figure 5-16: The pulse measurements at different frequencies. Top row: the response of the FOH S1. Bottom row: the response of the reference hydrophone.

Chapter 6

Conclusions and recommendations

As a result of the research as discussed in this thesis, conclusions and recommendations will be made in this chapter.

6-1 Goal and main conclusions

Goal

Before jumping into the conclusions, the goal of the research reported in this thesis is repeated:

The goal of the research reported in this thesis is to design, construct and test a hydrophone that can be used to detect ultra-high energy neutrinos, when implemented in a large-scale telescope.

To be implemented in a telescope for the detection of ultra-high energy neutrinos, the designed hydrophone has to meet requirements on sensitivity, dimensions, frequency range and pressure compensation. The emphasis during the design phase was to come up with different possibilities to design and optimize transducers that convert pressure into strain in a fiber. Topology and shape optimization techniques were implemented. In particular, emphasis was placed on both the manufacturing and testing of a hydrophone, such that the dynamic behavior predicted by finite element method models could be verified experimentally.

A systematic approach to design and optimize a transducer, that converts pressure to strain in a fiber, was used to design a fiber optic hydrophone. Four hydrophones were successfully constructed and tested. By experimentally investigating the dynamic behavior of the four constructed models, the predicted dynamic behavior by the FEM models was verified. Hence it was concluded that the modeling approach was sufficiently accurate. Detailed findings and recommendations on the different approaches used for the design, the manufacturing and the experiments are presented in Section 6-2.

Requirements

Sensitivity: The first requirement is that the hydrophone must be able to measure the ambient noise in the sea at Sea State 0 (SS0). The sea state is a variable that describes the state of the ocean, when there is more wind (a higher level of the sea state), the sea is noisier and the ambient noise is higher. SS0 is when the water surface is very calm and the water looks glassy. SS1 is when the water surface shows small ripples and SS4 is when the conditions are moderate. When the hydrophone can measure as low as the ambient noise in the sea, the noise in the sea is the limiting factor on the minimum amplitude of the signal caused by neutrino interaction that can be measured. Otherwise the sensitivity of the hydrophone is the limiting factor. The designed hydrophone can measure the ambient noise at SS1 in its complete frequency range, the ambient noise at SS0 can only be measured below 10 kHz and around the first eigenfrequency of the hydrophone. The conditions in the sea are mostly above SS0, hence most of the time the noise will be the limiting factor.
In the case of measuring at a location with an ambient noise lower than the hydrophone is able to measure, slightly more hydrophones are needed to cover the whole detection volume of the telescope. The fiber optic hydrophone has a sensitivity that is significantly higher than required to measure the acoustic signal coming from ultra-high energy neutrino interactions. Thus, although the required sensitivity to measure SSO is only partially met, the hydrophone can still be used for the detection of ultra-high energy neutrinos.

Frequency range and directionality: The hydrophone should have a frequency range of 1 - 50 kHz. There was a trade-off between sensitivity and frequency range, hence concessions had to be made. The frequency range of the hydrophone goes up to 40 kHz. The hydrophone was also constrained to certain wavelength related dimensions. These constraints were made to obtain a hydrophone that does not show direction-dependent dynamic behavior. The hydrophone meets this requirement and only shows a small change in dynamic behavior due to directionality in its frequency range.

Pressure compensation: The fiber optic hydrophone needs to operate in the deep-sea at 3 km depth. As this exceeded the limits of the project, a pressure compensation mechanism was not designed in this research. However, designing such a mechanism is necessary before the hydrophone can be implemented in the acoustic telescope for neutrino detection. The behavior of the hydrophone, in the case of being pressure-compensated, was predicted. At a hydrostatic pressure of 300 bar, the pressure at 3 km depth, the dynamic behavior of the transducer will only slightly change.

Conclusions

The manufactured hydrophone and it's specifications are presented in Figure 6-1.

To conclude: the designed hydrophone is suitable for ultra-high energy neutrino detection. However, extra engineering is needed to design a pressure compensation mechanism and to implement it in arrays to be used in the neutrino detection telescope. The dynamic behavior was characterized using FEM models and was experimentally verified.

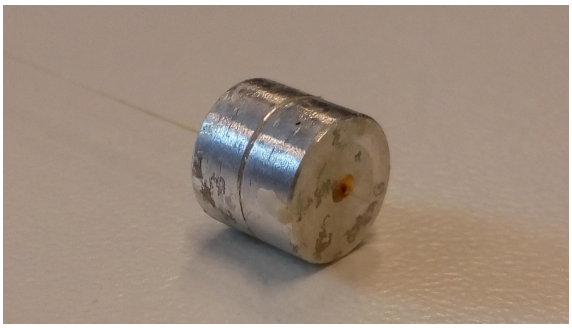

First eigenfrequency	37 kHz
Static sensitivity	3.95 $\frac{\text{n}\epsilon}{\text{Pa}}$
Height	5.65 mm
Diameter	6.46 mm
Thickness diaphragm	0.19 mm
Material	Aluminum
Fiber	125 μm diameter
FBG length	5 mm

Figure 6-1: Left: the manufactured hydrophone. Right: the specifications of the hydrophone.

6-2 Detailed findings and recommendations

6-2-1 Design and optimization

A systematic approach to design and optimize a transducer, that converts pressure to strain in a fiber, was used to design a fiber optic hydrophone. Extensive literature research was done on fiber optic based hydrophones. Surprisingly, only a small amount of mechanisms was found. Limited research on other types of hydrophones and transducers was done. It is recommended that when further research is continued in this area, the literature on other types of hydrophones should also be explored, as they are more developed than the fiber optic based hydrophones.

Topology optimization was used to find inspiration for new transducer concepts. Many different topology optimization simulations with hydrostatic pressure as load and various settings were performed in a 2D and 2D axi-symmetric environment. A large amount of possible designs was conceived. However, the conversion of the topology optimized designs to real concepts was too extensive and time-consuming in the context of this project and therefore it was decided to optimize an already existing concept.

Although many potential designs were found, there are some flaws in the optimization that are recommended to be improved in the future. Most optimization issues originate from the pressure load that is applied in the optimization. The complexity of topology optimization with pressure load problems lies in the fact that at each iteration step the pressure load changes in location, direction and magnitude. One of those issues is that it is difficult to get a stable optimization, another is that no procedure was found to force the boundaries of the transducer to form a closed cavity. Hence, not all the resulting designs of the optimization have closed boundaries. When a boundary is not closed, the design does not function under a real hydrostatic loads. For further research other methods to work with hydrostatic pressures loads can be tried, such as methods with boundary identification or with a filter on densities to determine where pressure should be applied.

Topology optimization can also be implemented inside an already existing transducer to enhance the performance. In this way no hydrostatic pressure directly interacts with the finite elements in the design domain of the optimization. Finally, when the encountered problems are solved, the optimization should be applied in 3D, which will cost much more computational time. 3D has total design freedom and no limitations, such as the design must be symmetrical, and therefore very different and potentially superior designs can be formed.

This research done within the framework of this project can be seen as a good starting point for future research on the use of topology optimization in combination with pressure loads.

The dimensions of two concepts, the diaphragm and the reversed diaphragm were parametrically optimized. Two algorithms were used to obtain the highest sensitivity, while constraining the eigenfrequency. Different eigenfrequencies values were used as constraints to create sufficient variation in frequency range and sensitivity to select an optimal design for the detection of neutrinos. One phenomenon that had to be taken into account during optimization is the effect of added mass. When a structure accelerates in a fluid, the fluid applies an extra inertial force on the structure. This causes a large decrease of the eigenfrequency of a diaphragm that is moving in water. The added mass effect is a complex phenomenon and not much literature was found on estimating the effect of added mass with FEM software. With the method that was employed in this thesis the added mass could be estimated and used for optimization. This method includes the estimation of the added mass applied on the diaphragm in function of the diameter of the diaphragm. This estimation was based on a curve fit of the calculated added mass for several different radii of the diaphragm.

There are some recommendations for the parametric optimization: the first is on the estimation of the added mass effect. When calculating the frequency response of the optimized design using FEM models, which included the acoustic physics, it was observed that the estimate of the added mass was not perfect. To illustrate: the optimized design, which was used as the basis of the final design, has an eigenfrequency at 36.7 kHz, while the optimization was constrained to a minimum eigenfrequency of 40 kHz. So, the estimation of the added mass was not precise for very small diameters of the diaphragm. It is recommended to find a better fit for the estimation of the added mass when doing further research on hydrophones, because its effect on the eigenfrequency can be considerable. Alternatively, a coupled acoustic-structural simulation approach can be used, however this gave challenges in identifying the structural vibration modes out of the many structural and acoustic modes the simulation produces. This is an interesting entry for further research. In future research shape optimization on the shape of the diaphragm can be of added value. For example, one could think of a corrugated diaphragm.

6-2-2 Manufacturing

The parametrically optimized design was first simplified to make manufacturing simpler. Two hydrophones with the optimized dimensions and two hydrophones of three times longer length were manufactured. The longer hydrophones were manufactured to study the effect on the dynamical behavior caused by a different ratio of transducer length to the wavelength of the acoustic waves. Machining the components was easy, however the assembly showed some difficulties. It proved difficult to attach the thin optical fiber to the transducer, without the risk of breaking the fiber. Further engineering is needed to make the assembly more suitable for mass manufacturing. Another recommendation is to make a design with more margin between the length of the FBG and the transducer in which the FBG must fit. A last recommendation is to design a hydrophone in which the fiber laser can be engraved in the fiber while it is already fixed to the transducer. In this way the fiber laser is automatically aligned with the transducer and the fiber laser, which is invisible, does not have to be located before assembly.

6-2-3 Experiments

The goal of the experiments was to verify the frequency response functions of the transducer as predicted with FEM. Four types of measurements (static, frequency sweeps, pulses and tones) were executed to have a complete set of data, such that they could complement and corroborate each others results. The experimentally determined behavior of two of the manufactured hydrophones corresponds very well with the predicted frequency response functions. The sensitivities and the location of the eigenfrequencies match. The other two hydrophones showed similar behavior as well, when taking into account the possibility that the diaphragms were manufactured stiffer than expected.

By doing measurements with the source located at different orientations to the hydrophones, it was possible to verify the directionality of the hydrophones. Also with measurements at different depths, the depth dependency could be confirmed. The hydrophones behave linearly at low and high frequencies and thus the determined behavior of the hydrophones is also valid at low pressure amplitudes, like in the cases when the signal comes from neutrino interactions. Furthermore, pulse measurements were conducted with pulses, which have approximately the same shape as the signal coming from a neutrino interaction.

There are, however, a few (unexplained) artifacts observed in the measurements that raise questions. One can occasionally see a dip in the sensitivity at the eigenfrequency and also the data are very noisy under 10 kHz, resulting in the situation that no conclusions can be drawn about the behavior of the sensors below this frequency. It is recommended to examine these artifacts. In the transfer functions of the sweep measurements a large constant jitter was present. It is likely that this jitter is caused by echos in the basin, in which the tests were conducted. To avoid these echos, the measurements should be done in a large volume lake or sea.

Finally, additional measurement were conducted with a pistophone. They were done to compensate for signal losses in the reference hydrophone system. For several reasons it was assumed that the results of those measurements were invalid. An accurate calibration of the complete measurement system is necessary for good results and thus the problem with the signal loss measurement should be resolved before doing further testing. A first experiment to do this is by using an acoustic source of which the behavior is well known.

Appendix A

Acoustic waves and units

A-1 Acoustic waves

An acoustic wave is the propagation of a mechanical perturbation in a medium, in this case water. Because the medium has elastic properties, the local compressions and decompressions propagate from one point to its surrounding points, away from their source. The rate of propagation is called the velocity of the acoustic wave. The acoustic waves in water are longitudinal waves. The acoustic pressure is the variation of pressure around the average hydrostatic pressure.

The propagation velocity c of the acoustic wave depends on the density ρ and the elasticity modulus E of the medium, which are also dependent on the pressure, salinity and temperature. The wavelength at a certain frequency is thus also dependent of those variables. In sea water the velocity is close to 1500 m/s, in air this is approximately 340 m/s [45].

$$c = \sqrt{\frac{E}{\rho}} \tag{A-1}$$

$$\lambda = cT = c/f. \tag{A-2}$$

In acoustics it is common to work with logarithmic scales, intensity and power. The absolute acoustic pressure is expressed in dB re 1 μPa.

A-1-1 Propagation losses

There are two main processes in which the acoustic wave loses intensity, the geometrical spreading loss and the attenuation loss. These losses determine the range of the acoustic wave. The hydrophone's performance depends directly on signal to noise ratio and thus on the amplitude of the acoustic wave at that point.

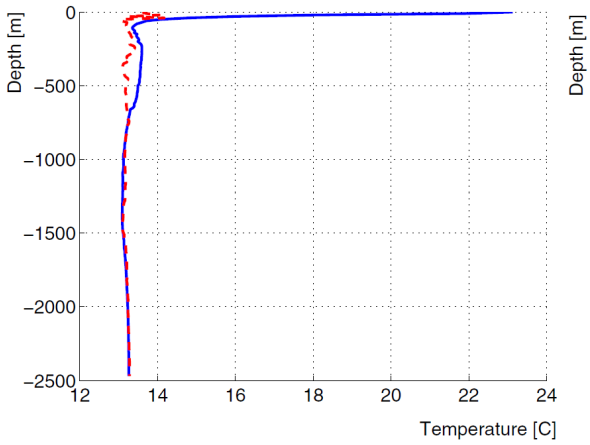

Figure A-1: The temperature distribution in the Mediterranean sea.

First a small explanation about the geometrical spreading loss. When the acoustic wave spreads from its source and the energy of the acoustic source is conserved, the energy will spread over spheres with larger and larger radii, R_i. The intensity will decrease each time it is further from the source. The intensity, seen in equation Eq. (A-1-1), will decrease proportionally to the surfaces (S_i) of the spheres.

$$\frac{I_1}{I_2} = \frac{S_2}{S_1} = \left(\frac{R_1}{R_2}\right)^2. \tag{A-3}$$

Second there is the attenuation loss. When the acoustic wave is traveling through the water, part of the energy is absorbed by the sea water, this is called attenuation loss. In distilled water the attenuation loss is proportional to the square of the frequency of the wave. Because of this waves with a higher frequencies have a higher attenuation loss and will propagate less than the waves at lower frequencies. In sea water there is also some extra attenuation due to the ionic relaxation of chemical compounds [6], this is dependent on pressure and temperature of the water. The Mediterranean sea where the telescope will be located shows some favorable characteristics for neutrino detection. At great depths the sea still has a temperature of about 13 degrees Celsius and the change in temperature is negligible, this is favorable for the ionic relaxation and causes a longer attenuation length. The temperature distribution in the Mediterranean sea is shown in Figure A-1. In Figure A-2 the absorption and attenuation length in the sea and in pure water are depicted, as seen, the absorption is very dependent on frequency.

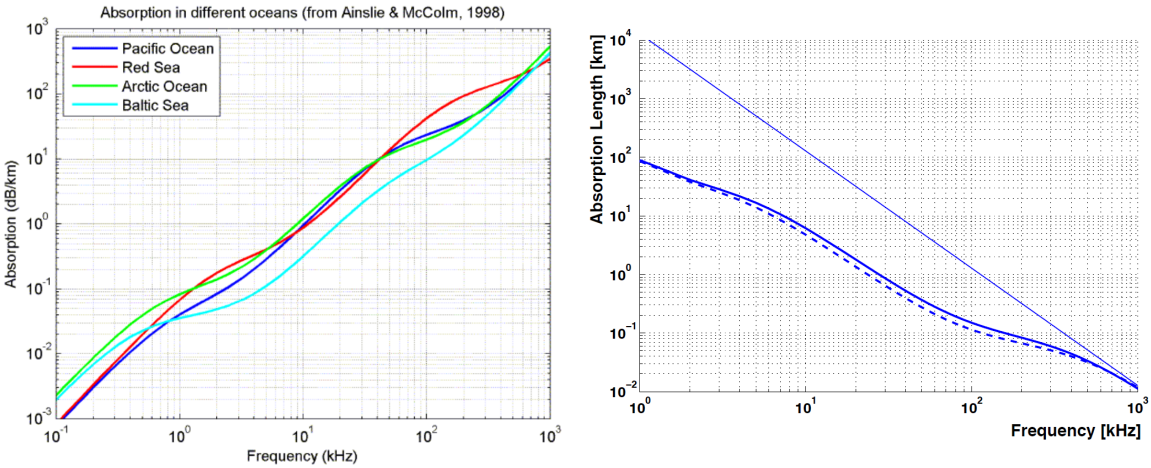

Figure A-2: Left: the absorption of acoustic waves in function of the frequency of the wave [46]. Right: the attenuation length of acoustic waves in functions of the frequency of the wave [6]. The straight line is in pure water, the solid thick line is in seawater at 2000 m depth and the dashed line is in seawater at 100 m depth.

A-2 Logarithmic scale and power spectral density

Because the large range in acoustic pressure and power it has become common to use a logarithmic scale, this scale is noted in decibels (dB). A dB quantifies the difference between two values. A decibel is equal to $10 \log_{10} \frac{P_1}{P_2}$. A 10 dB difference between P_1 and P_2 means that P_1 is ten times higher than P_2.

When working with acoustic pressure, the sound pressure level (SPL), the ratio of intensities, is expressed as in equation Eq. (A-4).

$$\text{SPL} = 10 \log \left(\frac{P_1}{P_2} \right) = 10 \log \left(\frac{p_1^2}{p_2^2} \right) = 20 \log \left(\frac{p_1}{p_2} \right). \tag{A-4}$$

A reference level, p_{ref} is used to be able to compare the absolute pressure in dB.

$$p_{dB} = 20 \log \left(\frac{p}{p_{ref}} \right). \tag{A-5}$$

In underwater acoustics 1 μPa is usually used as the pressure reference. When working with air the reference pressure is usually 20 μPa. In water this is thus expressed as dB re 1 μPa.

The power spectral density (PSD) is the mean-squared pressure of the noise measured in a given frequency bandwidth divided by the measurement bandwidth, it is also called the spectral level (SPL). Its decibel unit in underwater acoustics is dB re 1 $\frac{\mu \text{Pa}^2}{\text{Hz}}$. The total power content of the PSD is the same as that of the time signal the PSD is calculated from.

Appendix B

Added mass effect

FEM models were made of two beams of which the eigenfrequencies in water are already known in literature. The eigenfrequencies, experimentally determined in literature [47][48], and found by simulations are listed in Table B-1 and Table B-2. Figure B-1 shows one of the models of the simulations. The boundary condition at the outer side of the acoustical domain is the spherical wave radiation boundary condition.

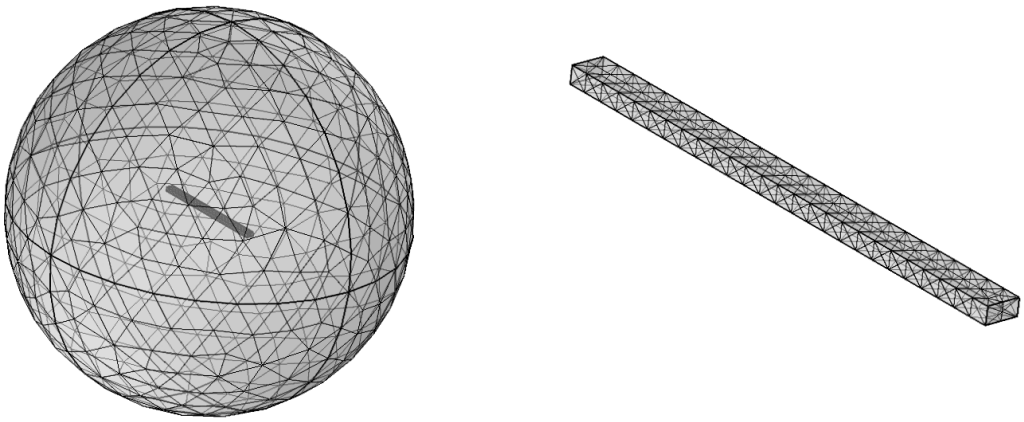

Figure B-1: Model for the simulation of a beam in water.

Table B-1: The eigenfrequencies of a one side clamped beam found with simulations and according to [47].

Mode	In air from source	In air simulation	In water from source	In water from simulation
1	15.1	15.16	4.2	5.51
2	94.9	94.98	30	34.86
3	266.2	266.14	95	99.52
4	522	522.15	198	200.12

Table B-2: The eigenfrequencies of a one side clamped beam found with simulations and according to [48], only the bending modes of the beam are in the table.

Mode	In air from source	In air simulation	In water from source	In water from simulation
1	169.12	177.92	128.46	137.5
2	1060.1	1109.6	809.3	862.1
3	2947.5		2201.4	2421.5

Appendix C

Topology optimization

C-1 Overview

There is a vast choice in how to set up the TO simulations. Here the variations on objective, constraints, boundary conditions and more that were studied are laid out.

- Material properties
  - Young's modulus and Poisson ratio
    - Different ranges in which the Young's modulus can vary:
    - 1e-6 to 1e3 Pa
    - 1e-6 to 1 Pa
    - 1e-3 to 1e3 Pa
    - 1e-3 Pa to 200 GPa
    - 1 Pa to 200 GPa
  - Bulk modulus and shear modulus
- Interpolation methods
  - SIMP: with varying heights of penalization
  - RAMP
  - SIMPRAMP [49]
- Interpolation between different material phases
  - Solid - void
  - Solid - void - Soft material
  - Solid - Soft material
  - Solid - water

  - Solid - void - water [50]

- Shape design domain
  - Quarter circle
  - Half circle
  - Circle
  - Rectangular
  - Hole, in the middle of the design domain, that is not part of the design domain. No design can be formed here.
  - Small gap around fiber which is not part of the design domain.

- Initial design field
  - Uniform value for the density of all elements
  - Gradient in the begin densities from the elements
  - Starting design

- Model of fiber (solid, spring, thin elastic layer, long, short, ...)

- Filter
  - None
  - Helmholtz filter

- Boundary conditions
  - Symmetric
  - Soft boundary
  - Roller
  - Elastic with springs
  - Hard boundary
  - Hard+soft boundary

- Load cases of varying sizes (from 1e-6 Pa to 1 Pa)
  - Point/boundary load
  - Pressure loads
  - Prescribed displacement
  - Load with direction pointed to the middle
  - Load on point/boundary of solid structure
  - Prescribed displacement solid structure
  - Loads with springs
  - Expansion solid material

- Discretization of elements
  - Linear
  - Quadratic
  - Higher order elements
  - Lagrange/serendipity
  - Real/complex
- Objective function (maximizing or minimizing)
  - Displacement of (the end) point on fiber
  - Maximizing elastic energy in fiber
  - Maximizing the strain in the fiber
  - 1/(one of the above objective functions)
  - The quadratic of one of the above objective functions, with this approach the optimization algorithm can choose to for example to extend or shorten the fiber
- Constraints
  - Maximum amount of material
  - Maximum ratio between different material phases
  - Elastic energy in the design domain
  - Maximum displacements of elements
  - Elastic energy with a pseudo-gravity load case
- Mesh
  - Element size
  - Element shape
  - All uniform elements
- Termination criteria
  - Maximum number of iterations
  - Convergence of the objective function

C-2 Discretization

The typical force inverter problem is used for a small discretization study. 100 iterations were done for each optimization with different settings, the results and settings are shown in Figure C-1. The first column are the components in the simulations that are discretized and the second column lists the various possible settings. The "x" in the other columns depict which setting were used and at the bottom of the columns the resulting design after 100 iterations is depicted.

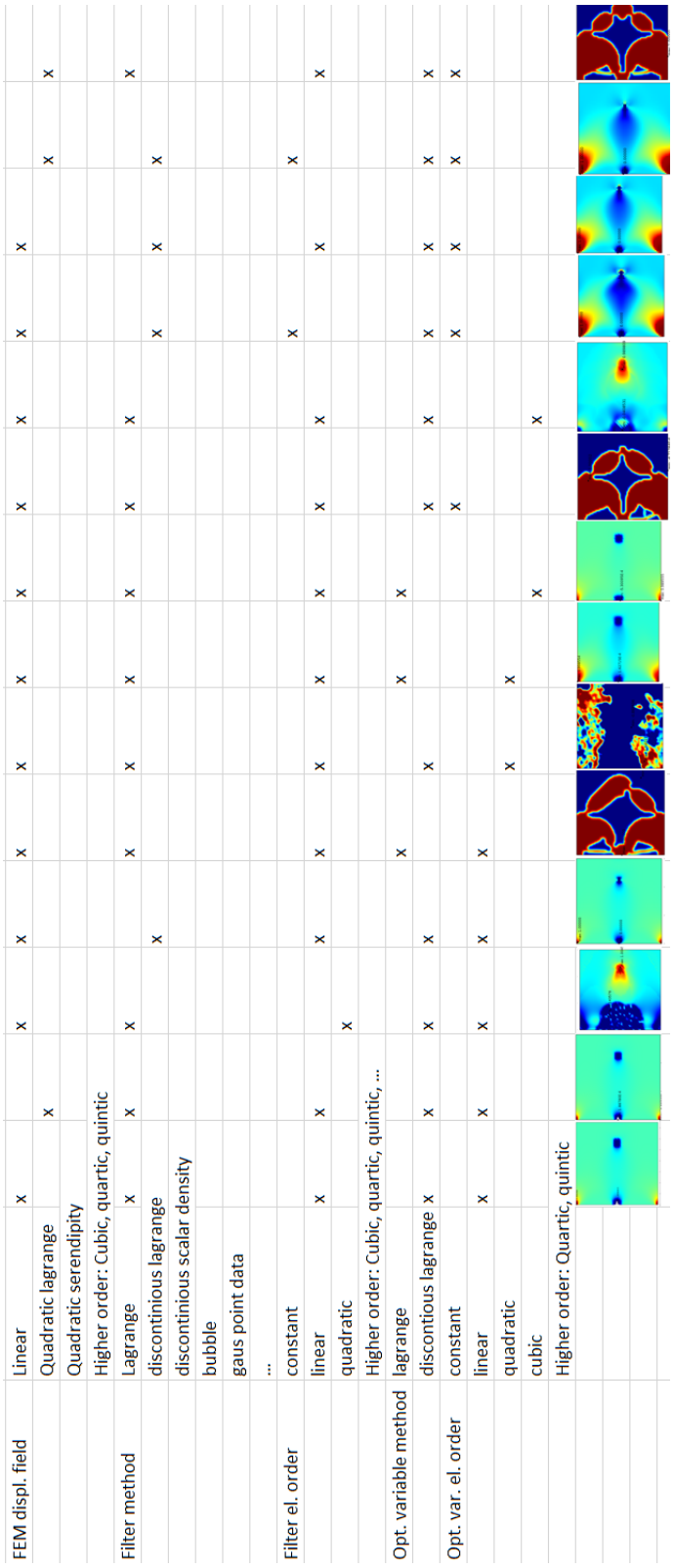

Figure C-1: A small discretization study for the TO. The "x" marks which discretization settings are used in the optimization. The results of the optimization after 100 iteration are seen in the pictures.

Appendix D

Finite element model

For this research Comsol, a finite element method (FEM) package, is used. Several simulation models are used for different purposes. First a brief explanation on the used physics is given and then the models that were used for the different purposes are explained and checked.

D-1 Physics and boundary conditions

Three different physics or modules are used. First of all the structural and acoustics physics are used to solve the equations of motion. The fluid-structure interaction interface is added to combine the structural and acoustic physics on their shared boundaries. Second the optimization module is used to set-up the optimization algorithms with its objective, constraints and other settings.

The structural module solves the mechanical equations for the elastic deformations of the transducer, while the acoustic toolbox solves the Navier-Stokes equations to find the velocity and pressure fields of the fluid. The multiphysics coupling is on the acoustic-structure boundary interface. It couples a pressure acoustics model to structural components, including the fluid load on the structure and the structural acceleration as experienced by the fluid. For example: the velocity of the structure is coupled to the velocity of the fluid and on that boundary they must be the same. The equations that are used on exterior boundaries read as follows, where n is the surface normal, u_{tt} is the structural acceleration, p_t is the total acoustic pressure and F_A is the load experienced by the structure:

$$-n(-\frac{1}{\rho_c}(\delta p_t - q_d)) = -nu_{tt}.F_A = p_t * n \tag{D-1}$$

The solvers should behave correctly when coupling the physics. The model should be fully coupled or solved in a segregated way, for large models an iterative solver could be more efficient or robust.

The name of the finite element method already tells that the size of the model and the amount of elements is finite. It is not possible to recreate an infinite domain for outgoing acoustic waves, such as there is in real life situations. In Comsol two options to truncate the acoustic domain are given, such that reflection of the waves at the outer boundaries of the model is minimized: the perfectly matched layer (PML) and the spherical boundary condition. When the spherical boundary condition is applied on a boundary, it is completely transparent for waves traveling perpendicular on the boundary. Waves at other angles are also passed, but when the angle becomes too sharp to the boundary they tend to get reflected. The PML is not a boundary condition but rather a domain, a layer, that is added around the model and that artificially absorbs the wave equations. When perfectly modeled the PML absorbs waves of all frequencies and with every angle of incidence.

D-2 Models

D-2-1 Added mass estimation

The function, which was used to estimate the added mass during the parametric optimizations, was derived using two separate models. To calculate the eigenfrequencies of the concept in water a model with the structural and acoustic physics was used. To estimate the added mass, which has to be applied on the diaphragm, a model which only includes the structural physics was used.

The structural-acoustic model is shown in Figure D-1. The green depicts the acoustic domain, with water as material. The red depicts the transducer, made of steel, and the blue depicts the fiber, made of silica glass. A spherical wave radiation boundary condition is applied on the outer edge of the circle. The structural model is identical to the structural-acoustic model, but without the acoustic domain. In both models a prestress (initial stress and strain) was applied on the fiber in the z-direction, as shown on the right in Figure D-2. In the structural model an added mass was applied on the diaphragms, as presented on the left in Figure D-2.

The spherical wave radiation boundary condition was used to truncate the acoustic domain. With this method there is no need to add extra elements to the model. Later it turned out that this was not the right choice as the PML gives more accurate results. This may be the reason why there was a the discrepancy between the estimated eigenfrequencies during the optimization and the eigenfrequencies seen in the frequency response fuctions that were calculated later on.

D-2-2 Optimization

The models used during the parametric optimizations resemble the models used for the added mass estimation. The only difference was that they include an extra line of symmetry to reduce computational time, only the half of the transducer was simulated in the model. This model also had a prestress in the fiber. The objectives and constraints in the optimization were calculated as follows:

- The eigenfrequency constraint was checked by doing an eigenfrequency study of the transducer while the diaphragms are loaded with the added mass.

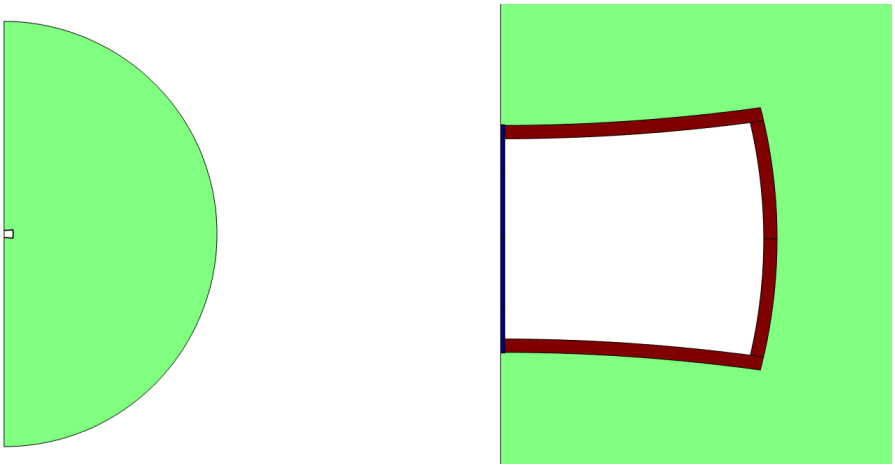

Figure D-1: Model with the acoustic and structural physics used for added mass estimation. The green color indicates the acoustic domain, which has water as a material. The red color indicated the transducer and the blue color indicates the fiber, which is made of silica glass.

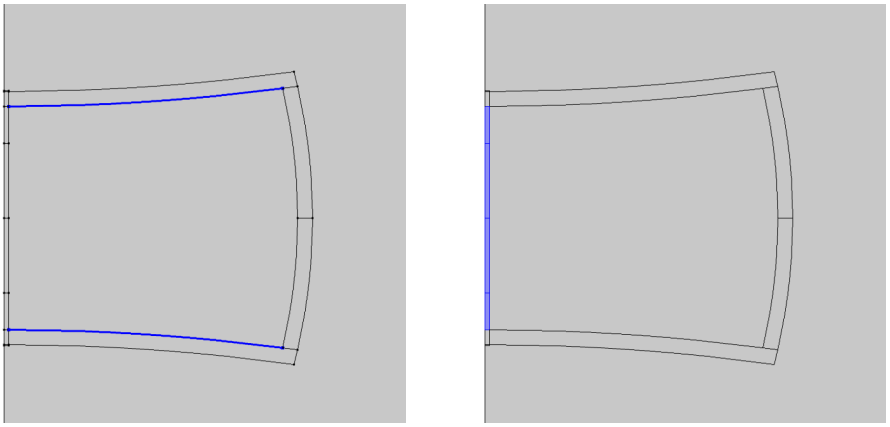

Figure D-2: Left: the boundaries on which the added mass is applied. Right: the areas in which the prestress in the fiber is applied.

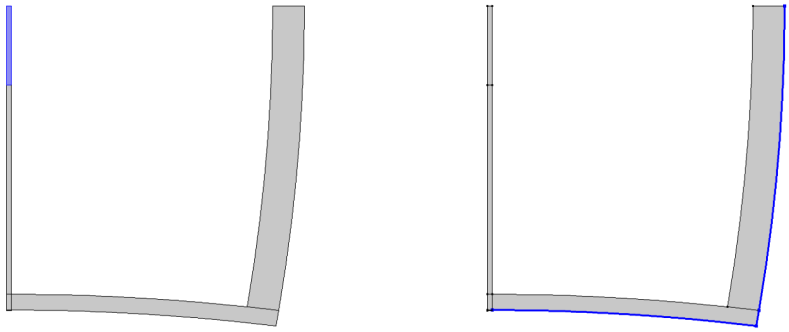

Figure D-3: The FEM model that was used for the parametric optimizations of the diaphragm concept. Left: the blue indicate the area in which the strain was measured. Right: the boundaries on which the pressure load was applied during the parametric optimizations are blue.

- The other constraints only includes geometrical measurement, they do not need a study to be checked.
- The objective was calculated by doing two static studies. One with a boundary load and one without, the boundaries which were loaded are depicted in Figure D-3. For both studies the strain in the blue part of the fiber as shown in Figure D-3 was calculated. The objective was found by subtracting the strains with- and without the boundary load.

D-2-3 Frequency response function

The frequency response function was calculated using the model seen in Figure D-4. Dark blue depicts the PML, light blue depicts the acoustic domain, red the fiber, orange the glue and green the aluminum transducer. The structure was fixed in the point as indicated on the left in Figure D-5. The strain was measured in the blue section in the middle figure. The boundary load to simulate waves coming from the right side, thus traveling in the horizontal direction, was applied on the blue boundaries in the right of the figure. The formula used for the boundary load was $\cos(\frac{2\pi}{c/freq}R)$, with R being the distance from the axi-symmetric axis and $freq$ the frequency of the incoming wave. The loadcase in the situation that the wave was coming from below was applied using a background pressure field in the acoustic domain. The most outer boundary of the PML had a spherical wave radiation boundary condition.

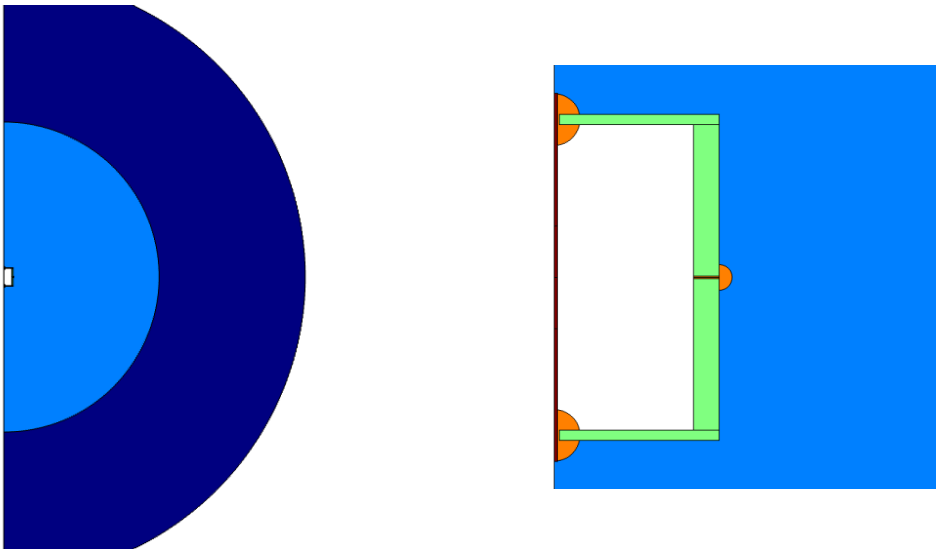

Figure D-4: The FEM model that is used to calculate the frequency response functions. Dark blue indicates the PML, light blue indicates the acoustic domain, green the transducer, orange the glue and red indicate the fiber.

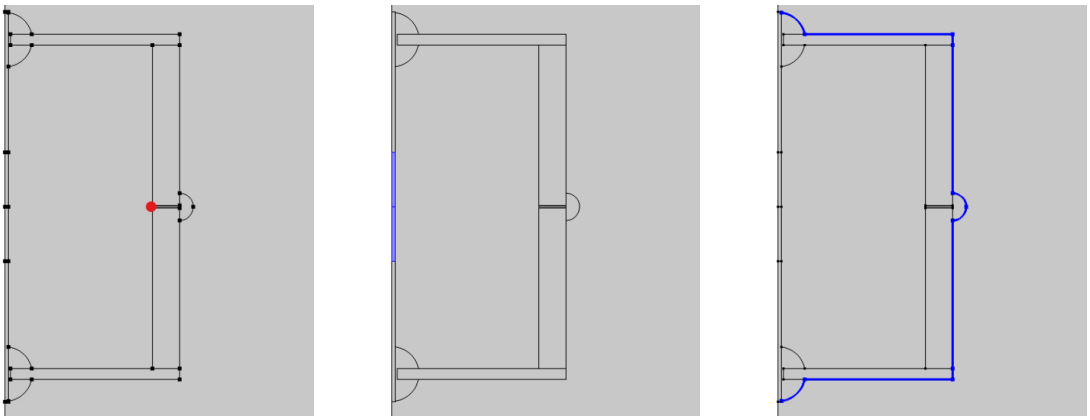

Figure D-5: Boundary conditions of the FEM model used for the calculation of the FRFs. Left: the point that was fixed in the model. Middle: blue indicated the area where the strain in the fiber was measured. Right: the blue boundaries were loaded by the pressure load, when waves were simulated to travel in the horizontal direction.

D-3 Error checking

There are methods to check whether a model is already sufficiently accurate. The models in this thesis were checked using a mesh refinement convergence study, an element order convergence study and by comparing them to experimental data.

D-3-1 Mesh refinement convergence study

The mesh and the accuracy that can be obtained are directly related to each other. For each element in the mesh the governing equations are solved. When the mesh is too coarse, not enough accuracy is obtained. When the mesh is very fine a good approximation of the true value is found, however the computational time will be much larger. With the mesh refinement study the model was solved multiple times, but each time a finer mesh was implemented. The results of these different simulations were compared by analyzing the strain in the fiber at multiple frequencies. The model was meshed as in Figure D-6.

First a mesh-convergence check was done for the mesh of the diaphragm. A fixed number of elements was imposed on the blue borders as is illustrated on the left side of Figure D-7. The boundaries on the right side had the same number of elements divided by 5. The mesh used for the calculations is shown on the left.

In Figure D-8 the mesh convergence checks are shown for the mesh of the diaphragm. With 35 elements, the amount that was used in the calculations, the sensitivity is already very accurate.

Next a mesh convergence check was done on the other structural elements. A mesh was assigned by using the automatic size function in Comsol. Using this function the mesh can change ranging from a course mesh tot a very fine mesh. The mesh that was used for the FRFs was made with the 'normal' mesh size settings. The results of the check are shown in Table D-1. From this it is deduced that the mesh size settings of these components do not have a large effect on the sensitivity.

Table D-1: Mesh convergence study of the other structural elements.

Mesh size settings	Sensitivity 1 kHz
normal	3.9600
fine	3.9600
finer	3.9602
Extra fine	3.9604
Extremely fine	3.9604

Next the mesh of the acoustic domain was checked. The maximum element size of the acoustic domain is obtained by dividing the shortest wavelength by 8. In Figure D-9, the mesh convergence checks for different mesh sizes are shown. The mesh convergence study was done for waves with a frequency of 1 Hz, 20 kHz and 80 kHz. Only at the high frequencies, the settings matter because than the element size is of the same order of magnitude as the wavelength. At lower frequencies the element size is already a lot smaller than the wavelength and

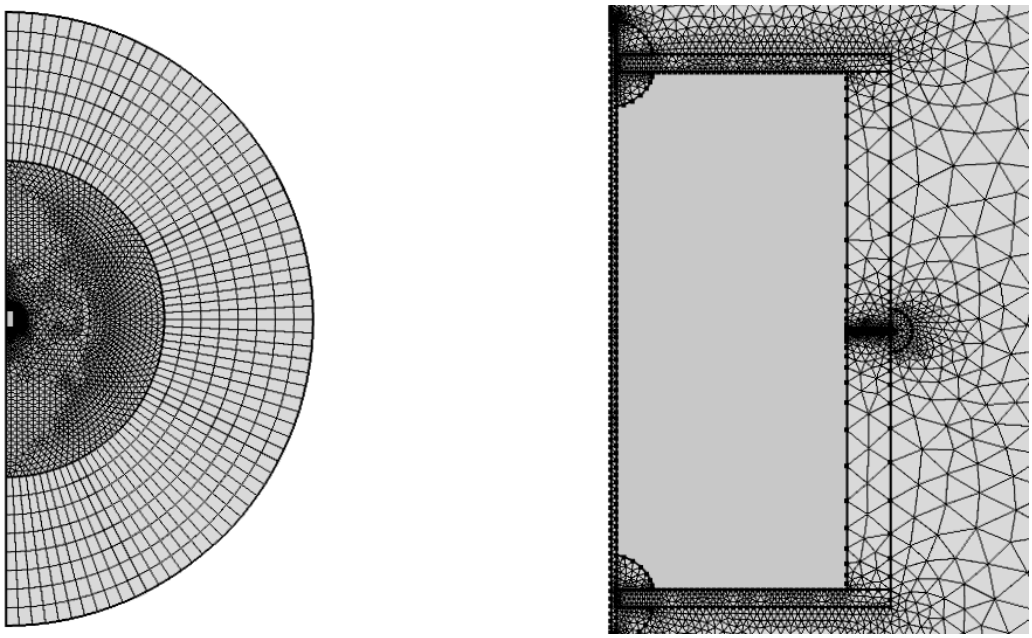

Figure D-6: The mesh used in the FEM models. The PML has a structured mesh, while the other parts use an unstructured triangular mesh.

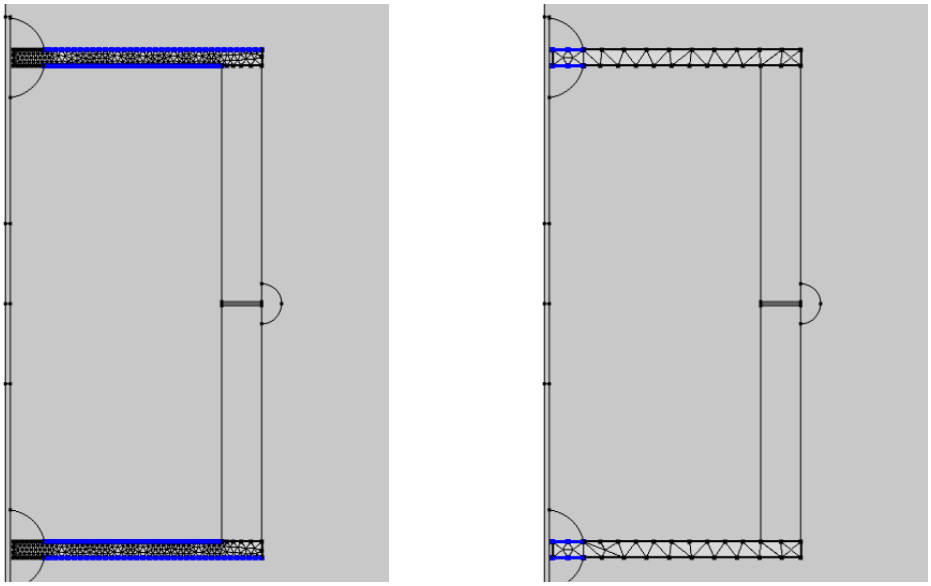

Figure D-7: The mesh of the diaphragm in the FEM model. Left: a fixed number of elements was imposed on the blue borders. Right: the same number of elements divided by 5 is imposed on the blue borders.

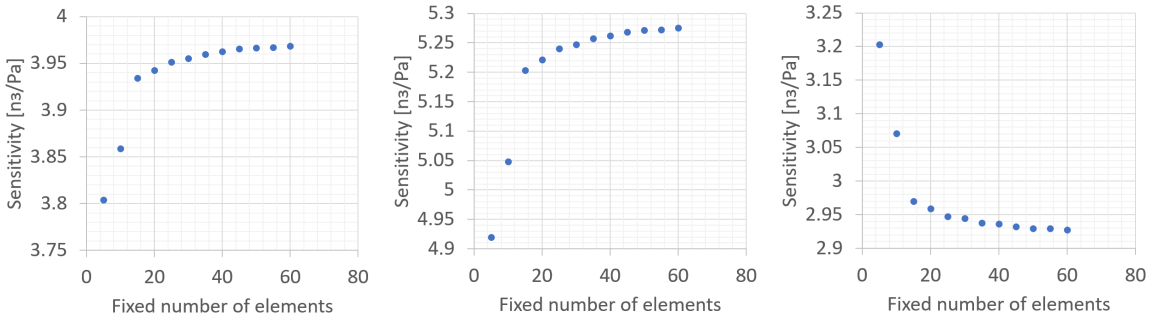

Figure D-8: The convergence check for the mesh of the diaphragm was done by changing the amount of elements. Left: acoustic wave at 1 Hz. Middle: acoustic wave at 20 kHz. Right: acoustic wave at 50 kHz

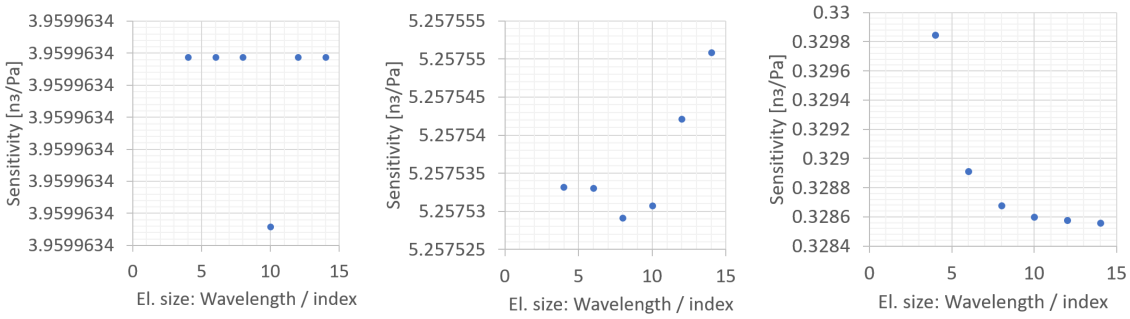

Figure D-9: The mesh convergence check for the acoustic domain. The used maximum element size was the wavelength divided by the index of the x-axis in the figure. As seen the difference in sensitivity between the used element sizes is negligible at lower frequencies. At a higher frequency, 80 kHz, convergence is clearly seen. Left: acoustic wave at 1 Hz. Middle: acoustic wave at 20 kHz. Right: acoustic wave at 80 kHz.

thus the changes in element size had negligible effect.

The influence by the size of the acoustic domain on the sensitivity was also checked. The radius of the acoustic domain was calculated as is the equation below:

$$Radius = r_{cyl} + D + \frac{\lambda_{low}}{AA} \tag{D-2}$$

r_{cyl} is the radius of the diaphragm, D is the thickness of the outer walls of the hydrophone, λ_{low} is the wavelength of an acoustic wave in water at 3 kHz, AA was varied between a value of 2 and 12 to change the radius of the acoustic domain. The change in sensitivity, for pressure waves at 1 Hz and 20 kHz, was negligible in this radius.

The PML had a structured mesh, that consisted of 8 layers. The PML has different stretching options and in this case the rational stretching option was used as this is commonly used for open radiation problems and it is efficient for many angles of incidence. The thickness of the PML layer was checked for convergence. The PML thickness was: λ_{low}/DD, where DD was varied between 2 and 12. The change in sensitivity, for pressure waves at 1 Hz and 20 kHz, was negligible in this range of thickness.

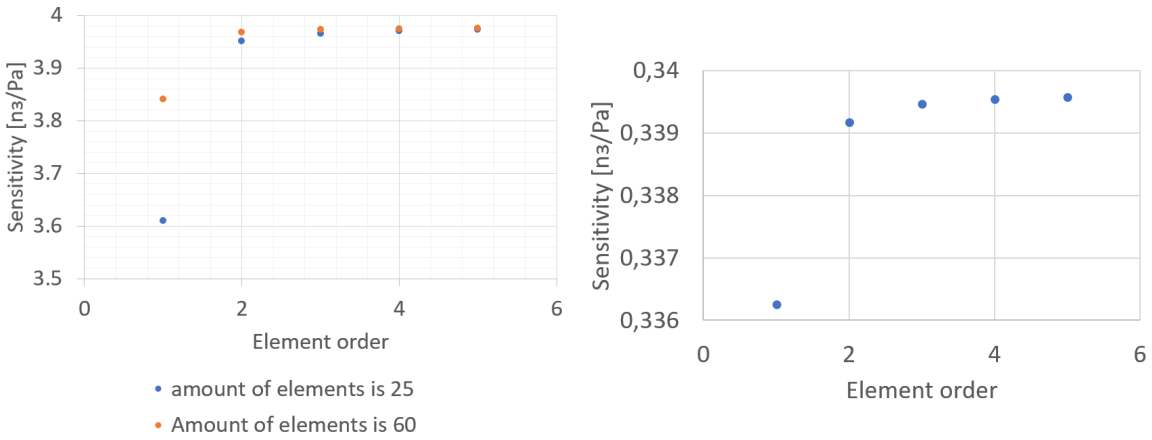

Figure D-10: The element order convergence check. Left: the element order for the structural physics is varied. Right: the element order for the acoustic physics is varied.

D-3-2 Element order convergence study

The element order convergence study works basically the same as the mesh refinement study. The only difference is that now size of the elements does not change, but that the elements order changes. In the left side of Figure D-10 the element order convergence study for the structural module is shown. The fixed amount of elements of the diaphragm was 25 or 60 and the element size for the other structural elements was set to "coarse". On the right side of the figure the element order convergence study for the acoustic elements is shown. Only when the elements are linear the difference in sensitivity is large. In the models a quadratic element order was used.

Bibliography

[1] R. Lahmann, *Ultra-High-Energy Neutrinos and Their Acoustic Detection in the Sea*. PhD thesis, Friedrich-Alexander Universität Erlangen-Nürnberg, 2011.

[2] S. Aiello, M. Ageron, J. A. Aguilar, Amore I, and M. Anghinolfi, "KM3NeT Technical Design Report for a Deep-Sea Research Infrastructure in the Mediterranean Sea Incorporating a Very Large Volume Neutrino Telescope," tech. rep., KM3NeT, 2011.

[3] J. D. Perkin, *The Acoustic Detection of Ultra High Energy Neutrinos*. PhD thesis, The University of Sheffiel, 2007.

[4] U. F. Katz and C. Spiering, "High-energy neutrino astrophysics: Status and perspectives," *Progress in Particle and Nuclear Physics*, vol. 67, no. 3, pp. 651–704, 2012.

[5] R. Engel, D. Seckel, and T. Stanev, "Neutrinos from propagation of ultrahigh energy protons," *Physical Review D - Particles, Fields, Gravitation and Cosmology*, vol. 64, no. 9, p. 10, 2001.

[6] R. Lahmann, "Acoustic detection of high energy neutrinos in sea water: status and prospects," *EPJ Web Conf.*, vol. 135, no. 06001, 2017.

[7] R. Lahmann, "Acoustic Detection of Neutrinos: Review and Future Potential," *Nuclear and Particle Physics Proceedings*, vol. 273-275, pp. 406–413, 2016.

[8] S. Bevan, A. Brown, S. Danaher, J. Perkin, C. Rhodes, T. Sloan, L. Thompson, O. Veledar, and D. Waters, "Study of the acoustic signature of UHE neutrino interactions in water and ice," Tech. Rep. February 2013, The ACORNE collaboration, 2009.

[9] E. J. Buis, E. J. J. Doppenberg, R. A. Nieuwland, and P. M. Toet, "Fibre laser hydrophones for cosmic ray particle detection," in *13th Topical Seminar on Innovative Particle and Radiation Detectors (IPRD13)*, vol. 9, 2013.

[10] N. Kurahashi and G. Gratta, "Oceanic ambient noise as a background to acoustic neutrino detection," *Physical Review D - Particles, Fields, Gravitation and Cosmology*, vol. 78, no. 9, pp. 1–5, 2008.

[11] K. Graf, "Acoustic neutrino detection in sea water: Technical aspects," in *AIP Conference Proceedings 1535*, pp. 169–175, University of Erlangen, 2013.

[12] P. Antunes, F. Domingues, M. Granada, and P. Andr, "Mechanical Properties of Optical Fibers," in *Selected Topics on Optical Fiber Technology* (InTech, ed.), 2012.

[13] G. Scott Glaesemann, "Optical Fiber Mechanical Reliability Review of Research at Corning ' s Optical Fiber Strength Laboratory," Tech. Rep. July, Corning, 2017.

[14] FBGS Technologies GmbH, "https://www.fbgs.com/technology/fbg-principle/," 2018.

[15] V. M. Baas, P. Toet, and E. J. Buis, "Fiber laser design and measurements for fiber optic hydrophones in their application for ultra-high energy neutrino detection," in *Proceedings of Science, The 34th International Cosmic Ray Conference*, vol. 30-July-20, (The Hague), 2015.

[16] H. W. Iversen and R. Balent, "A correlating modulus for fluid resistance in accelerated motion," *Journal of Applied Physics*, vol. 22, no. 3, pp. 324–328, 1951.

[17] L. Peeperkorn, "A fiber laser pressure sensor: for the detection of ultra-high energy neutrinos," 2018.

[18] S. Huang, X. Jin, J. Zhang, Y. Chen, Y. Wang, Z. Zhou, and J. Ni, "An optical fiber hydrophone using equivalent phase shift fiber bragg grating for underwater acoustic measurement," *Photonic Sensors*, vol. 1, no. 3, pp. 289–294, 2011.

[19] Y. Liu, W. Zhang, T. Xu, J. He, F. Zhang, and F. Li, "Fiber laser sensing system and its applications," *Photonic Sensors*, vol. 1, no. 1, pp. 43–53, 2011.

[20] G. H. Ames and J. M. Maguire, "Miniaturized mandrel-based fiber optic hydrophone.," *The Journal of the Acoustical Society of America*, vol. 121, no. 3, pp. 1392–5, 2007.

[21] S. Foster, A. Tikhomirov, M. Milnes, J. van Velzen, and G. Hardy, "A fiber laser hydrophone," in *Proc. of SPIE*, vol. 5855, p. 627, Defence Science and Technology Organisation,Thales Underwater Systems Pty Ltd, 2005.

[22] N. Beverini, R. Falciai, E. Maccioni, M. Morganti, F. Sorrentino, and C. Trono, "Developing fiber lasers with Bragg reflectors as deep sea hydrophones," *Annals of Geophysics*, vol. 49, no. 6, pp. 1157–1165, 2006.

[23] P. E. Bagnoli, N. Beverini, B. Bouhadef, E. Castorina, E. Falchini, R. Falciai, V. Flaminio, E. Maccioni, M. Morganti, F. Sorrentino, F. Stefani, and C. Trono, "Erbium-doped fiber lasers as deep-sea hydrophones," *Nuclear Instruments and Methods in Physics Research, Section A: Accelerators, Spectrometers, Detectors and Associated Equipment*, vol. 567, pp. 515–517, 2006.

[24] A. I. Azmi, I. Leung, X. Chen, S. Zhou, Q. Zhu, K. Gao, P. Childs, and G. Peng, "Fiber laser based hydrophone systems," *Photonic Sensors*, vol. 1, no. 3, pp. 210–221, 2011.

[25] P. E. Bagnoli, N. Beverini, R. Falciai, E. MacCioni, M. Morganti, F. Sorrentino, F. Stefani, and C. Trono, "Development of an erbium-doped fibre laser as a deep-sea hydrophone," *Journal of Optics A: Pure and Applied Optics*, vol. 8, no. 7, 2006.

[26] U. K. Chandrika, V. Pallayil, C. Zhihao, and N. J. Hong, "Development of a high sensitivity DFB fibre laser hydrophone," in *Proceedings of the 2011 International Symposium on Ocean Electronics, SYMPOL-2011*, pp. 103–108, Acoustic Research Laboratory, National University of Singapore,A*STAR Institute of InfoComm Research, 2011.

[27] F. Zhang, X. Zhang, L. Wang, and C. Wang, "Study on the frequency response of static pressure compensated fiber laser hydrophone-theory and finite element simulation," in *Proceedings of Spie*, no. June 2014, p. 91571I, Shandong Academy of Science, 2014.

[28] L. Hansen and F. Kullander, "Modelling of hydrophone based on a DFB fiber laser," in *Mechanics of 21st Century - ICTAM04 Proceedings*, pp. 15–21, Technical University of Denmark, FOI, Swedish Defence Research Agency, 2004.

[29] G. Grosso and F. Mosca, "Fiber bragg grating hydrophone compromising a diaphragm amplifier, US 8,687,927 B2," 2014.

[30] U. Kuttan Chandrika, V. Pallayil, K. M. Lim, and C. Heng, "Design Considerations for a Dfb Fibre Laser Based High Sensitivity Broadband Hydrophone," in *Proceedings of the 11th European Conference on Underwater Acoustics DESIGN*, National University of Singapore, 2012.

[31] W. Zhang, L. Liu, F. Li, and Y. Liu, "Fiber Bragg grating pressure sensor with enhanced sensitivity," *Chinese optics letters*, vol. 5, no. 9, p. 507, 2007.

[32] D. M. K. Woo, "Pressure compensatde hydrophone, US 6,882,595 B2," 2005.

[33] X. Ni, Y. Zhao, and J. Yang, "Research of a novel fiber Bragg grating underwater acoustic sensor," *Sensors and Actuators, A: Physical*, vol. 138, no. 1, pp. 76–80, 2007.

[34] U. Kuttan Chandrika, V. Pallayil, K. M. Lim, and C. H. Chew, "Pressure compensated fiber laser hydrophone: Modeling and experimentation," *The Journal of the Acoustical Society of America*, vol. 134, no. 4, pp. 2710–2718, 2013.

[35] S. Foster, A. Tikhomirov, and J. V. Velzen, "Towards a High Performance Fiber Laser Hydrophone," *Journal of lightwave technology*, vol. 29, no. 9, pp. 1335–1342, 2011.

[36] E. J. Buis, E. J. J. Doppenberg, R. Lahmann, P. M. Toet, and J. D. Vreugd, "Fiber optic hydrophones for acoustic neutrino detection," in *EPJ Web of Conferences 116,*, vol. 03002, pp. 2–5, TNO Technical Sciences, University of Erlangen, 2016.

[37] M. P. Bendsøe and O. Sigmund, *Topology optimization: theory, methods, and applications*, vol. 2nd Editio. Springer-Verlag Berlin Heidelberg, 2 ed., 2003.

[38] E. Lee and J. R. R. A. Martins, "Structural topology optimization with design-dependent pressure loads," *Computer Methods in Applied Mechanics and Engineering*, vol. 233-236, pp. 40–48, 2012.

[39] B. S. Lazarov and O. Sigmund, "Filters in topology optimization based on Helmholtz-type differential equations," *International Journal for numerical methods in engineering*, vol. 86, pp. 765–781, 2011.

[40] COMSOL, *Optimization Module: User's Guide*. version: c ed., 2018.

[41] R. Dong, *Effective mass and damping of submerged structures.* PhD thesis, Lawrence Livermore laboratory University of California, Washington, 1978.

[42] M. K. Kwak and S.-B. Han, "Effect of fluid depth on the hydroelastic vibration of free-edge circular plate," *Journal of Sound and Vibration*, vol. 230, no. 1, pp. 171–185, 2000.

[43] National Instruments, "Understanding FFTs and Windowing," 2015.

[44] Siemens, "https://community.plm.automation.siemens.com/t5/Testing-Knowledge-Base/Windows-and-Spectral-Leakage/ta-p/432760," 2018.

[45] X. Lurton, *An introduction to underwater acoustics : principles and applications.* London: Springer, 2002.

[46] M. A. Ainslie and J. G. McColm, "A simplified formula for viscous and chemical absorption in sea water," *The Journal of the Acoustical Society of America*, vol. 103, no. 3, pp. 1671–1672, 1998.

[47] F. J. Elmer and M. Dreier, "Eigenfrequencies of a rectangular atomic force microscope cantilever in a medium," *Journal of Applied Physics*, vol. 81, no. 12, pp. 7709–7714, 1997.

[48] J. A. N. Hengstler and J. Dual, "Influence of the Fluid-structure Interaction on the Vibrations of Structures," 2013.

[49] M. Bruggi and C. Cinquini, "An alternative truly-mixed formulation to solve pressure load problems in topology optimization," *Computer Methods in Applied Mechanics and Engineering*, vol. 198, no. 17-20, pp. 1500–1512, 2009.

[50] C. Peter Michael and S. Ole, "Topology optimization using a mixed formulation : An alternative way to solve pressure load problems," *Computer Methods in Applied Mechanics and Engineering*, vol. 196, no. 13-16, pp. 1874–1889, 2007.